

Subcarrier Multiplexing for Next-Generation Optical Access Networks

Jonathan M. Buset



Department of Electrical & Computer Engineering
McGill University
Montréal, Québec, Canada
July 2014

A thesis submitted to McGill University
in partial fulfilment of the requirements of the degree of
Doctor of Philosophy

© Jonathan M. Buset, 2014

To JB.

Abstract

The advent of the Internet in the 1970s has led to an unprecedented level of global connectivity enabling communication across continents and oceans. Over the last ten years, its continuous commercialization and adoption by mainstream consumers has led to tremendous growth in global traffic which is stressing the capacity of all current network layers. This trend is expected to continue as the technology permeates deeper into our lives through affordable mobile devices and high bandwidth services such as on-demand streaming audio and video services, high-definition television and remote cloud storage. To meet these projected traffic demands, experts anticipate that fiber-to-the-home access networks based on single mode optical fibers will provide a future-proof upgrade pathway to replace the existing copper-based infrastructure.

By employing mature technologies from transport networks, wavelength-division multiplexed passive optical networks (WDM PONs) are a leading candidate technology to achieve the projected 10 Gbit/s service rates of next-generation access networks. However, their commercial viability hinges on the availability of low cost and wavelength-independent client side transceivers to meet the economic constraints set by the service providers. Bidirectional single feeder WDM PONs with reflective semiconductor optical amplifier (RSOA)-based uplink transmitters are a well researched solution, but in general their performance has been limited by two key factors: 1) bidirectional impairments due to scattering, reflections and inter-channel crosstalk; and 2) the RSOA's limited modulation bandwidth.

This thesis proposes using a combination of radio frequency subcarrier multiplexing (SCM) and digital signal processing (DSP) to address these challenges. We develop three generations of SCM WDM PON architecture to increase the bandwidth efficiency and the symmetric transmission bit rates as compared to previous SCM solutions. We also implement DSP-based techniques to compensate for the bandwidth-limited RSOA-based transmitter. In each case we experimentally realize the system's operation and verify its bit error rate performance over a 20 km single feeder WDM PON with bidirectional transmission and wavelength reuse. To demonstrate the architecture's economic viability, we intentionally limit the electronic and optoelectronic hardware to 10 GHz of electrical

bandwidth. The evolution of the three architectures leads to 2.5 Gbit/s, 5 Gbit/s and 10 Gbit/s symmetric line rates. We successfully demonstrate the operation of a 10 Gbit/s SCM WDM PON using pulse shaped higher-order quadrature amplitude modulation (QAM) channels with cost effective intensity modulation and direct detection optoelectronic transceivers. We further optimize the system parameters and characterize its symmetric operation for different QAM orders and channel spectral efficiencies. Ultimately, we successfully demonstrate that SCM WDM PONs are a viable and flexible solution for next-generation optical access networks operating at 10 Gbit/s data rates.

Résumé

L'avènement d'Internet dans les années 1970 a mené la connectivité à un niveau sans précédent, permettant des communications au-delà des continents et des océans. Lors des dix dernières années, sa commercialisation continue et son adoption par des consommateurs grand public a mené à une immense croissance du trafic global ce qui pousse les capacités de chaque niveaux du réseau d'aujourd'hui vers leurs limites. Cette tendance doit persister alors que la technologie s'encre plus profondément dans nos vies grâce aux appareils mobiles abordables et les services à larges bandes passantes tels que les services audio et vidéo sur demande en continu, la télévision haute définition and le stockage en nuage à distance. Pour répondre à ces futures demandes de trafic, les experts s'attendent à ce que les réseaux d'accès à fibre optique jusqu'à domicile s'appuyant sur des fibres optique monomode puissent fournir des options de mise à jour à l'épreuve du temps pour remplacer les infrastructures existantes reposant sur le cuivre.

En utilisant les technologies éprouvées du transport de réseaux, les réseaux optiques passifs à multiplexage en longueur d'onde (WDM PONs) sont une technologie de pointe potentielle pour l'accomplissement d'un débit de 10 Gbit/s prévu pour la prochaine génération de réseaux d'accès. Cependant, leur viabilité commerciale dépend de la disponibilité d'émetteurs à faible coût et indépendant de la longueur d'onde du côté du client pour répondre aux contraintes économiques mises en place par les fournisseurs de services. Des WDM PONs à transmission simple et bidirectionnelle avec des émetteurs montant s'appuyant sur des amplificateurs optiques semi-conducteurs réfléchissant (RSOA) sont une excellente solution, mais souvent leur performance est limitée par deux facteurs principaux: 1) la dégradation bidirectionnelle due à la diffusion, les réflexions et la diaphonie entre canaux; et 2) la limite de la bande passante de modulation des RSOA.

Cette thèse propose de surmonter ces défis en utilisation une combinaison de multiplexage de sous-porteuses (SCM) à fréquences radio et le traitement de données numériques (DSP). Nous avons développer trois générations d'architecture de SCM WDM PON pour augmenter l'efficacité de la bande passante et le débit de la transmission symétrique par rapport aux solutions SCM précédentes. Nous avons aussi implémenter des techniques de traitement de données numériques

pour compenser les limites sur la bande passante des émetteurs RSOA. Dans chaque cas nous avons réalisé expérimentalement les opérations du système et vérifié la performance du taux d'erreur binaire d'un WDM PON à transmission simple et bidirectionnelle permettant la réutilisation des longueurs d'onde sur une distance de 20 km. Pour démontrer la viabilité économique de l'architecture, nous avons intentionnellement limité la bande passante électrique du matériel électronique et optoélectronique à 10 GHz . L'évolution des trois architectures ont mené à des débits de transmission symétrique de 2.5 Gbit/s, 5 Gbit/s et 10 Gbit/s. Nous avons démontré avec succès le fonctionnement d'un SCM WDM PON à 10 Gbit/s utilisant des canaux à modulation d'amplitude en quadrature (QAM) d'ordre élevé en forme d'impulsion ayant une intensité de modulation rentable et des émetteurs optoélectroniques à détection directe. Nous avons optimisé davantage les paramètres du système et caractérisé la fonction symétrique pour des QAM d'ordres différents et des canaux de différentes efficacités spectrales. Ultiment, nous avons démontré avec succès que les SCM WDM PONs sont une solution viable et flexible pour la prochaine génération de réseaux d'accès optiques fonctionnant à des débits de 10 Gbit/s.

Acknowledgements

First, and foremost, I would like to thank my advisor Prof. David V. Plant for his encouragement, guidance and support over the course of my Ph.D. research. You provided me with the tools, expertise and freedom to explore new ideas while having the foresight to rein me in if I strayed too far from the objectives. The world-class lab facilities and talent that you have assembled are amazing and I feel privileged to have spent time as a part of it. Thank you.

The research group that I work in is full of fun and friendly peers, all of whom I now consider to be my friends. My heartfelt thanks go out to all of the past and present members of the Plant Group and the broader Photonic Systems Group. You have made my Ph.D. studies at McGill both interesting and enjoyable. Immeasurable thanks go to my friend and colleague Ziad El-Sahn, whose guidance, encouragement and support throughout our many days together in the lab have made this work possible. It was a pleasure working with you. Thank you also to Mathieu Chagnon for your amazing lab skills and boundless enthusiasm; to Mohamed Osman for many interesting conversions and knowledge of all things signal processing; to Mohammad Pasandi for helping me get a start in the lab and encouraging me to try new ideas; to Zhaobing Tian for his friendship and unparalleled lab expertise; to Bhavin Shastri for our collaborations; to Sandrine Filion Côté for great conversations and graciously agreeing to translate my abstract; and to the rest of the Plant Group for the many wonderful days and nights we worked together.

Many people around the McConnell building have directly contributed to my research and I would like to acknowledge their contributions here. I would like to thank my Ph.D. supervisory committee including Prof. Andrew G. Kirk and Prof. Zetian Mi for their input and support throughout the stages of my doctoral studies. Thanks also go out to Chris Rolston for technical support and for steering the administrative ship; to Philip Roche for many enlightening conversations and for keeping the labs running safely and smoothly; to Prof. Tho Le-Ngoc and Robert Morawski for sharing their equipment and providing me with training; to Maru Basanez, Carrie Serban and Kay Johnson in the SYTACom office; to Brent Snow for his technical support; and to Don Pavlasek for his wizardry in the machine shop.

I also wish to thank all of my friends at McGill and in the broader Montréal area for making these past years fun and enjoyable: Daniel McGuire, Dylan McGuire, Jody Swift, Philip Egberts, Adam Schneider, Jeff Bates, Jessica Topple, Gil Holder, Jonathan Guillemette, Dave Plant, Aleks Labuda, Kevin MacDermid, Sarah Dyck, James Kennedy, Sébastien Guillot, Alex Creamer and Paul Wiseman. I would also like to thank the members of the Icy Photons and Cold Fusion intramural hockey teams. It was a pleasure being your teammate and coach. My sincerest apologies to anyone that I may have overlooked.

Throughout the many long days and late nights spent completing this work, I have been supported by my wonderful fiancée Jessica. Her patience and kindness during this process has been above and beyond the call of duty. I cannot express how much I look forward to our next adventures together.

Finally, I wish to thank my family. Immeasurable thanks go to my parents Richard and Liz; to my grandparents; to my sister Kathleen and brother-in-law Jesse; and to all of my extended family. This whole process would not have been possible without your love and unwavering support.

A handwritten signature in black ink, appearing to be 'R. B.', with a long horizontal flourish extending to the right.

Statement of Originality

The work described in this thesis represents original scholarship by the author, and has not been submitted for a degree or diploma at any other institution. This thesis contains no material previously written or published by any other persons excepted where references are made. As evidence of my original scholarship and contribution to the existing body of knowledge, this work has currently resulted in ten peer-reviewed publications, comprising four journal articles [1–4] and six refereed conference proceedings [5–10]. We note that one of these conference proceedings is an invited contribution [6]. Portions of Chapters 4 and 6 were published as original work with the author of this thesis appearing as the first author in each publication. A summary of our contributions is as follows:

- We propose the concept of overlapped-subcarrier multiplexing (O-SCM) to relax the channel separation requirements in bidirectional wavelength-division multiplexed passive optical network (WDM PON) systems [5]. We experimentally demonstrate 1.5 Gbit/s full-duplex transmission with bit error rates (BERs) below 10^{-10} without the aid of electronic equalization or forward-error correction (FEC) coding. At the time of publication this was the highest reported symmetric bit rate for a bidirectional WDM PON with subcarrier multiplexing (SCM), downstream remodulation and a reflective semiconductor optical amplifier (RSOA)-based uplink transmitter.
- We further refine the O-SCM WDM PON's design and replace the proof-of-concept system's external modulator with an integrated commercial transmitter. We analytically derive and optimize the system's optical power budget, and experimentally demonstrate full-duplex transmission at 2.5 Gbit/s with BERs below 10^{-10} [1]. Additionally, we demonstrate operation with a stand-alone burst-mode (BM) receiver to perform clock and data recovery, instantaneous phase acquisition and radio frequency (RF) down-conversion of the 2.5 Gbit/s uplink channel [8].
- The second generation O-SCM architecture minimizes the impact of the RSOA modulation bandwidth by modifying the RF channel allocation. Furthermore, we design and implement

an offline analysis and digital signal processing (DSP) framework to electronically equalize the uplink signal and increase the symmetric bit rates [7]. We experimentally demonstrate full-duplex 5 Gbit/s operation and achieve BERs below the desired FEC coding thresholds [2]. At the time of publication we reported the lowest minimum launch power for a bidirectional SCM WDM PON operating at 5 Gbit/s.

- The third generation SCM WDM PON architecture implements higher-order quadrature amplitude modulation (QAM) signals and DSP to achieve symmetric 10 Gbit/s transmission over a 20 km single feeder bidirectional PON [3, 4, 9, 10]. We propose using DSP spectral pre-compensation to linearize the modulation response of the intensity modulation (IM) and direct detection (DD) optoelectronic transceivers, as well as using square-root raised cosine (SRRC) pulse shaping to increase the spectral efficiency of the QAM data channels. Combined, these improvements facilitate greater than 10 Gbit/s full-duplex transmission in only 10 GHz of electrical bandwidth. We develop the offline analysis framework and build the optical test beds to experimentally verify the system's BER performance. We demonstrate a resilience to upstream impairments and characterize the impact of system parameters such as pulse shaping roll-off factor, subcarrier frequency and QAM order. We report: 1) the first demonstration of a single carrier 10 Gbit/s SCM WDM PON with wavelength reuse, a commercial RSOA and 10 GHz IM/DD transceivers [3]; 2) the highest symmetric bit rate for a WDM PON with wavelength reuse and IM/DD quadrature phase-shift keying (QPSK) transmission for both the uplink and downlink channels [9]; 3) the first demonstration of a single carrier 10 Gbit/s 16-QAM SCM WDM PON using a commercial RSOA with wavelength reuse and IM/DD [10]; and 4) the highest net spectral efficiency for a 10 Gbit/s SCM WDM PON [4].

Contribution of Co-authors

Like many ambitious undertakings, academic research is rarely the work of a single individual. This thesis is no exception. Portions of the research presented were completed in collaboration with other authors and the contribution of each party is as follows:

- Chapter 2 presents a collaborative project between the Photonics Systems Group at McGill University and the Access and Broadband Networks group at Bell Canada. The author of this thesis, J. M. Buset, led the research and implementation of the Gaussian capacity model which forms the basis of the Internet bandwidth provisioning software. Z. A. El-Sahn led the development of capacity models to estimate the impact of additional customer services. The overall work was carried out under the supervision of the thesis advisor, Prof. D. V. Plant.
- In Chapter 3, the original concept of O-SCM WDM PONs was proposed by Z. A. El-Sahn. The author of this thesis, J. M. Buset, and Z. A. El-Sahn jointly performed and analyzed the transmission experiments at 1.5 Gbit/s and 2.5 Gbit/s. Z. A. El-Sahn was the lead author of the associated publications [1, 8] with content contributions and editing by the co-authors. The author of this thesis, J. M. Buset, and Z. A. El-Sahn cooperatively built and characterized the optical test bed for the BM receiver experiments at 2.5 Gbit/s. The BM clock and data recovery circuit was designed and implemented by B. J. Shastri who performed the experiments and analysis with Z. A. El-Sahn who was the lead author of the associated publication [8]. The overall work was carried out under the supervision of the thesis advisor, Prof. D. V. Plant.
- In Chapter 4 the author of this thesis, J. M. Buset, proposed an O-SCM architecture with an improved RF channel allocation scheme, designed and implemented the data acquisition and offline analysis framework, developed the measurement methodology, built the 5 Gbit/s O-SCM WDM PON experimental test bed and was the lead driver of the transmission experiments. Z. A. El-Sahn participated in some of the experiments and system characterizations. The author of this thesis, J. M. Buset, analyzed the data and was the primary author of the

associated publications [2, 7] with editing by the co-authors. The overall work was carried out under the supervision of the thesis advisor, Prof. D. V. Plant.

- In Chapters 5 and 6 the author of this thesis proposed using SRRC pulse shaped QAM channels as a means of reducing the inter-channel crosstalk in single feeder WDM PONs, and implemented DSP spectral pre-compensation to transmit higher-order modulation formats at 10 Gbit/s using inexpensive IM/DD optoelectronic devices. Z. A. El-Sahn wrote the first version of the DSP analysis framework code which the author of this thesis heavily modified and optimized for WDM PON applications. The first series of experiments presented in Sections 6.1 and 6.2 were cooperatively performed by the author of this thesis and Z. A. El-Sahn. The author of this thesis, J. M. Buset, analyzed the data and was the primary author of the associated publications [3, 9] with editing assistance by the co-authors. The transmission experiments in Sections 6.3 and 6.4 were performed solely by the author of this thesis, who analyzed the data and was the primary author of the associated publications [4, 10]. The co-authors assisted in editing the manuscripts. The overall work was carried out under the supervision of the thesis advisor, Prof. D. V. Plant.

Table of Contents

	<u>page</u>
Abstract	iii
Résumé	v
Acknowledgements	vii
Statement of Originality	ix
Contribution of Co-authors	xi
List of Tables	xvi
List of Figures	xvii
List of Abbreviations	xxi
1 Introduction	1
1.1 Motivation	1
1.1.1 Growth of Global Internet Traffic	1
1.1.2 Passive Optical Networks for Access	2
1.2 Review of the State of the Art	4
1.2.1 Current PON Technologies	4
1.2.2 Wavelength-Division Multiplexed PONs	7
1.2.3 Challenges for High-Speed WDM PONs	10
1.3 Problem Statement and Research Objectives	16
1.4 Thesis Overview	17
2 Bandwidth Capacity Estimation for a Deployed Gigabit-Capable PON	19
2.1 Introduction	19
2.2 Modelling GPON Bandwidth Capacity	20
2.2.1 Extreme Capacity Estimates	20
2.2.2 Gaussian Bandwidth Capacity Model	21
2.3 Usage Example	22
2.4 Summary	24
3 Overlapped-Subcarrier Multiplexing for WDM PONs	25
3.1 Overlapped-Subcarrier Multiplexing	25
3.2 Initial Demonstration at 1.5 Gbit/s	27
3.2.1 Physical PON Architecture	27
3.2.2 Optical Back-to-Back Performance	28
3.2.3 Full-Duplex Operation Over a 20 km WDM PON	29
3.2.4 Optical Power Budget	30
3.2.5 Operating Constraints for O-SCM	31

3.3	Optimized O-SCM WDM PON Operating at 2.5 Gbit/s	32
3.3.1	Changes to the Physical PON Architecture	33
3.3.2	BER Performance for 2.5 Gbit/s Symmetric Operation	34
3.3.3	Optimizing the ONU Coupler	35
3.4	A 2.5 Gbit/s O-SCM WDM PON With a Burst-Mode OLT Receiver	37
3.4.1	Physical PON Architecture	37
3.4.2	Burst-Mode Receiver Design for SCM Applications	38
3.4.3	Experimental Results	40
3.5	Summary	40
4	Electronically Equalized 5 Gbit/s Overlapped-SCM WDM PON	42
4.1	Offline Analysis and DSP Equalization Framework	42
4.1.1	Data Frame and Structure	43
4.1.2	Network-Based Data Acquisition	44
4.1.3	Data Frame Alignment and BER Calculation	45
4.1.4	Electronic Equalization	46
4.2	Physical PON Architecture	47
4.3	Experimental Results at 5 Gbit/s	49
4.3.1	Optical Back-to-Back Performance	50
4.3.2	Full-Duplex Operation Over a 20 km WDM PON	51
4.4	Summary	54
5	10 Gbit/s SCM WDM PONs with Higher-Order Modulation Formats	55
5.1	Spectrally Efficient M-QAM SCM WDM PONs	56
5.1.1	Generating M-QAM Signals with IM/DD Optoelectronics	56
5.1.2	Square-Root Raised Cosine Pulse Shaping	59
5.1.3	DSP Spectral Pre-compensation for Bandwidth-Limited Devices	61
5.2	Building Blocks of a 10 Gbit/s SCM WDM PON	63
5.2.1	Physical PON Architecture	63
5.2.2	Offline DSP Framework	64
5.2.3	Offset Optical Filtering	65
5.2.4	Upstream Impairments	66
5.3	Summary	67
6	Experimental Demonstrations of M-QAM SCM WDM PONs	68
6.1	10 Gbit/s QPSK SCM WDM PON	69
6.1.1	Physical PON Architecture	69
6.1.2	Downlink Performance	70
6.1.3	Uplink Performance	71
6.1.4	Parameter Sensitivities	72
6.1.5	Conclusion	73
6.2	10 Gbit/s 16-QAM/QPSK SCM WDM PON	73
6.2.1	Downlink Performance	74
6.2.2	Uplink Performance	76
6.2.3	Optimizing the Offset OBPF	77
6.2.4	Resilience to Upstream Impairments	78
6.2.5	Conclusion	80
6.3	10 Gbit/s 16-QAM SCM WDM PON	80
6.3.1	Physical PON Architecture	81
6.3.2	Offline DSP Framework	82

6.3.3	Downlink Performance	82
6.3.4	Uplink Performance	83
6.3.5	Comparison With the Shannon Limit	85
6.3.6	Discussion	86
6.3.7	Conclusion	87
6.4	Designing a Flexible 11.25 Gbit/s SCM WDM PON	87
6.4.1	Physical PON Architecture	87
6.4.2	Offline DSP Framework	88
6.4.3	Optimizing the Operating Parameters	89
6.4.4	Comparing M-QAM Channel Configurations	93
6.4.5	Discussion	95
6.5	Summary	96
7	Conclusions	97
7.1	Overview	97
7.2	Summary of Contributions	99
7.2.1	Overlapped-Subcarrier Multiplexed WDM PONs	99
7.2.2	Electronically Equalized Overlapped-Subcarrier Multiplexed WDM PONs	99
7.2.3	Pulse Shaped M-QAM Subcarrier Multiplexed WDM PONs	100
7.3	Future Research	100
7.3.1	DSP-Enabled PONs	100
7.3.2	Low-Cost Tunable Lasers for WDM PON	101
7.4	Final Thoughts	101
A	Further Details	102
A.1	Optical Signal to Rayleigh Backscattering Ratio	102
A.2	Principle of Subcarrier Multiplexing	103
A.3	Solving the Gaussian Bandwidth Approximation Model	104
A.4	Electrical Spectra for the M-QAM SCM WDM PON Scenarios	105
A.5	Additional Hardware Specifications	107
	References	124

List of Tables

<u>Table</u>	<u>page</u>
1-1 Current TDM PON standards.	5
4-1 Comparison of the Reed-Solomon FEC codes used in current PON standards.	44
4-2 Summary of the electronic equalizer parameters.	47
5-1 Summary of the bandwidth limiting components in the downlink and uplink transmission channels.	62
6-1 Operating parameters of the different M-QAM SCM WDM PON configurations.	94

List of Figures

<u>Figure</u>	<u>page</u>
1-1 Projected growth of global IP and consumer Internet traffic.	2
1-2 A general transport network with simple star topology PON.	3
1-3 A basic TDM PON architecture.	4
1-4 A basic TWDM PON architecture for NG-PON2.	6
1-5 A basic WDM PON architecture with bidirectional transmission.	8
1-6 RSOA remodulation and downlink erasure with gain clamping.	9
1-7 Measured modulation response of a butterfly-packaged RSOA.	10
1-8 The contributions of upstream impairments due to downlink and uplink transmissions.	13
1-9 A basic SCM WDM PON architecture with bidirectional transmission, wavelength reuse and downlink remodulation.	15
2-1 An example of a deployed GPON architecture.	20
2-2 An example client subscription distribution for a GPON high-speed Internet service.	23
2-3 A typical contour plot from the Gaussian bandwidth capacity tool.	24
3-1 The upstream RF channel allocation as detected at the OLT for three different SCM approaches.	26
3-2 Physical architecture of the 1.5 Gbit/s O-SCM WDM PON.	28
3-3 Measured BER performance of the 1.5 Gbit/s O-SCM system in an optical back-to-back configuration.	28
3-4 Bidirectional performance of the 1.5 Gbit/s O-SCM architecture over a 20 km WDM PON as a function of received power.	29
3-5 Bidirectional performance of the 1.5 Gbit/s O-SCM architecture over a 20 km WDM PON as a function of OLT launch power.	31
3-6 Power budget optimization of the ONU coupling ratio.	31
3-7 Illustrations of the 1 Gbit/s O-SCM channel allocation at different subcarrier frequencies and the RF spectra measured after down-conversion.	32
3-8 Physical architecture of the 2.5 Gbit/s O-SCM WDM PON.	33
3-9 Bidirectional performance of the O-SCM WDM PON over a 20 km feeder at 1.5 Gbit/s and 2.5 Gbit/s.	34

3-10	Optimization of the ONU coupling ratio with sensitivity and launch power.	35
3-11	Performance of the 2.5 Gbit/s O-SCM WDM PON with full-duplex transmission over a 20 km feeder using the 70/30 ONU coupling ratio.	36
3-12	Physical architecture of the 2.5 Gbit/s O-SCM WDM PON with BM clock and data recovery uplink receiver at the OLT.	38
3-13	Block diagram of the proof-of-concept BM receiver for SCM applications using a bang-bang Alexander phase detector.	38
3-14	Electrical eye diagrams of the received uplink signal.	39
3-15	Performance of the 2.5 Gbit/s SCM WDM PON with a stand-alone BM receiver. . .	40
4-1	Structure of the transmitted data frames.	43
4-2	Example of the data frames distribution in a captured data sequence and the cross- correlation of a received data frame aligned in time with its corresponding binary sequence.	46
4-3	Block structure of a fractionally spaced DFE.	47
4-4	Physical architecture of the 5 Gbit/s O-SCM WDM PON.	48
4-5	RF channel allocation in the 5 Gbit/s O-SCM WDM PON.	49
4-6	Physical architecture of the 5 Gbit/s O-SCM optical back-to-back test bed.	50
4-7	Optical back-to-back performance of the 5 Gbit/s O-SCM WDM PON.	51
4-8	Symmetric performance of the 5 Gbit/s O-SCM architecture over the 20 km single feeder WDM PON.	52
4-9	Operating regions of the 5 Gbit/s O-SCM architecture over the 20 km single feeder WDM PON.	53
5-1	A memoryless digital modulator.	56
5-2	Eye diagrams of multilevel PAM signals with a rectangular pulse shape.	57
5-3	Ideal I - Q constellation maps for Gray encoded QAM signals.	58
5-4	General modulation and demodulation schemes for a QAM signal.	58
5-5	Raised cosine impulse response and frequency domain spectrum.	60
5-6	Square-root raised cosine impulse response and frequency domain spectrum.	61
5-7	Magnitude response plots of the 16th order FIR filter, RSOA modulation response at 80 mA bias and pre-compensated RSOA response.	62
5-8	High level illustration of the 10 Gbit/s M-QAM SCM WDM PON including the downstream and upstream RF channel allocations.	63
5-9	Block diagram of the M-QAM transmitter DSP.	64
5-10	Block diagram of the M-QAM receiver DSP.	65

5-11 Measured profile of the JDSU VCF050 OBPF along with the upstream optical carrier's power spectra measured before and after filtering.	66
5-12 Experimental setup and measurement of the backscattering due to the downlink laser.	67
6-1 Physical architecture of the 10 Gbit/s QPSK SCM WDM PON.	69
6-2 Frequency content of the pre-emphasized downlink QPSK signal. Measured power spectrum of the received downstream signal.	70
6-3 BER performance of the downlink QPSK channel after transmission over a 20 km PON.	71
6-4 Frequency content of the pre-emphasized uplink QPSK signal loaded into the DAC memory. Measured power spectrum of the received downstream signal.	72
6-5 BER performance of the QPSK uplink channel in full-duplex operation.	72
6-6 Characterizing the impact of the downlink channel's subcarrier frequency and SRRC roll-off factor.	73
6-7 Uncompensated 16-QAM downlink channel performance for different subcarrier frequencies.	74
6-8 Effect of pre-compensation on the 2.5 Gbaud 16-QAM downlink transmission after 20 km.	75
6-9 Electrical power spectra of the uncompensated and pre-compensated uplink channel after transmission over 20 km.	76
6-10 BER performance of the uplink channel with and without spectral pre-compensation for the RSOA.	77
6-11 The impact of offset filtering and spectral pre-compensation on the uplink BER.	77
6-12 The inter-channel crosstalk's impact on the uplink channel transmission.	78
6-13 Influence of backscattering on the uplink channel performance.	79
6-14 Physical architecture of the 16-QAM SCM WDM PON.	81
6-15 Block diagram of the receiver DSP stack used for offline processing the downlink and uplink 16-QAM signals.	82
6-16 Performance of the 2.5 Gbaud 16-QAM downlink channel after transmission over a 20 km PON.	83
6-17 16-QAM uplink channel after transmission over a 20 km PON.	84
6-18 BER vs. E_b/N_0 for the downlink and uplink channels. Comparison of the 16-QAM SCM WDM PON performance with different SRRC roll-off factors to Shannon's channel capacity limit.	86
6-19 Physical architecture of the optimized M-QAM SCM WDM PON.	88
6-20 DSP stacks of the transmitter and receiver. The magnitude response of the spectral pre-compensation filters applied at the OLT and ONU transmitters.	89

6-21	Optimizing the clipping ratio for 16-QAM downlink and uplink transmissions.	91
6-22	Optimizing the SRRC roll-off factor for 16-QAM transmission channels.	91
6-23	Characterizing the effect of uplink subcarrier frequency.	92
6-24	BER performance of the downlink and uplink channels for scenarios with different modulation formats.	95
A-1	Power spectra for Scenario #1 with QPSK downlink and uplink channels.	105
A-2	Power spectra for Scenario #2 with 16-QAM downlink and QPSK uplink channels. .	105
A-3	Power spectra for Scenario #3 with 16-QAM downlink and uplink channels.	106
A-4	Power spectra for Scenario #4 with QPSK downlink and 16-QAM uplink channels. .	106

List of Abbreviations

10G-EPON	10 Gbit/s Ethernet PON
M-QAM	<i>M</i> -ary quadrature amplitude modulation
ADC	Analog-to-digital conversion
AWG	Arrayed-waveguide grating
BER	Bit error rate
BM	Burst-mode
CL	Confidence level
CW	Continuous-wave
DD	Direct detection
DDF	Distribution drop fiber
DFE	Decision-feedback equalizer
DSP	Digital signal processing
EDFA	Erbium-doped fiber amplifier
EML	Electro-absorption modulated laser
ER	Extinction ratio
FEC	Forward-error correction
FIR	Finite-impulse response
FTTH	Fiber-to-the-home
GPON	Gigabit-capable passive optical network
IM	Intensity modulation
IP	Internet protocol
ISI	Inter-symbol interference
LMS	Least-mean squared
LPF	Low pass filter

MLSE	Maximum-likelihood sequence estimation
NG-PON2	Next-generation passive optical network stage 2
NRZ	Nonreturn-to-zero
O-SCM	Overlapped-subcarrier multiplexing
OBI	Optical beat interference
OBPF	Optical band pass filter
ODN	Optical distribution network
OLT	Optical line terminal
ONU	Optical network unit
OSRBR	Optical signal to Rayleigh backscattering ratio
PAM	Pulse amplitude modulation
PAPR	Peak-to-average power ratio
PLL	Phase-locked loop
PON	Passive optical network
PRBS	Pseudo-random bit sequence
PSD	Power spectral density
QAM	Quadrature amplitude modulation
QPSK	Quadrature phase-shift keying
RB	Rayleigh backscattering
RF	Radio frequency
RN	Remote node
RS	Reed-Solomon
RSOA	Reflective semiconductor optical amplifier
SBS	Stimulated Brillouin scattering
SCM	Subcarrier multiplexing
SFO	Sampling frequency offset
SRRC	Square-root raised cosine
TDM	Time-division multiplexing

- TWDM** Time- and wavelength-division multiplexing
- VOA** Variable optical attenuator
- WDM** Wavelength-division multiplexing
- WDM PON** Wavelength-division multiplexed passive optical network
- XG-PON** 10-Gigabit-capable passive optical networks

CHAPTER 1

Introduction

THE EXPLOSIVE GROWTH OF INTERNET TRAFFIC in recent years, driven by consumers' appetite for data intensive services, is spurring the need for higher capacity communication networks. In 2012 there were an estimated 2.3 billion Internet users and more than 12 billion networked devices [11]. By 2017 global Internet traffic is expected to grow almost threefold [12]. Current access network technologies are not expected to scale to meet these traffic projections [13], and as a result, the adoption of next-generation solutions based on fiber optics will be required.

In this chapter we build the foundation of this thesis. In Section 1.1 we motivate adopting optical access networks to meet the projected demands of consumers. Section 1.2 provides a thorough overview of the state of the art, introducing the current standards and then presenting wavelength-division multiplexing (WDM) as a possible solution for next-generation access networks. We further detail the key challenges of achieving high-speed symmetric data rates of 10 Gbit/s in WDM passive optical networks (PONs) with wavelength reuse and describe the main solutions proposed in the literature. In Section 1.3 we detail the problem statement and research objectives that drive the direction of this research. Finally, Section 1.4 provides an overview of this thesis.

1.1 Motivation

1.1.1 Growth of Global Internet Traffic

Global Internet protocol (IP) traffic has increased fourfold over the past five years and is expected to increase another threefold over the next five years [11]. In Fig. 1–1(a), we see that the global traffic will continue to be dominated by fixed connections and that mobile networks are expected to increase nearly 13-fold by 2017. The total traffic in 2017 is expected to exceed 120 EB per month, or more than 1.4 ZB per year.¹

¹ Note that 1 ZB = 10^{21} B.

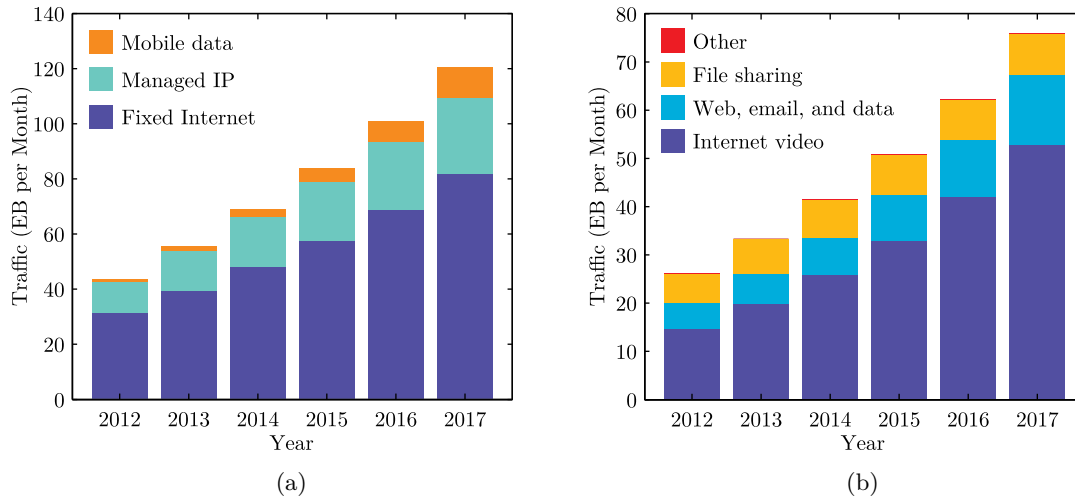


FIGURE 1–1: Projected growth of (a) global IP and (b) consumer Internet traffic [11].

Looking at the consumer traffic projections in Fig. 1–1(b), we see that Internet video will be by far the most dominant contributor to the growth. Unlike traditional multicast video traffic (i.e. broadcast television) which scales efficiently, on-demand Internet video is generally “over the top” unicast traffic. This bandwidth growth is expected to move farther down the network from the transport to metro level, as content delivery networks become the dominant source of Internet traffic [11, 14]. The growing popularity of data intensive services such as streaming on-demand Internet video and cloud-based storage will continue to drive the increase in bandwidth requirements for consumer broadband services.

1.1.2 Passive Optical Networks for Access

Previous generations of access networks allowed consumers to cost effectively connect to their Internet service provider over existing telephone and coaxial cable networks. However, as the number of Internet subscriptions and traffic demands increased, parts of these networks were replaced with optical fiber connections which have higher bandwidth, low loss and low noise. These optical access systems are referred to as fiber-to-the- x , where x can be home (H), curb (C), premises (P), neighbourhood (N), etc. indicating how close the fiber is to the user [15]. In a FTTH system, optical fiber is used to connect all the way from the service provider to the customer premises to eliminate any bandwidth bottlenecks due to legacy transmission lines. In this sense, FTTH represents a future-proof means of supplying consumers with nearly unlimited bandwidth [13].

Figure 1–2 illustrates the structure of a modern telecommunication network with a PON as the access network, which connects customer to the Internet service provider’s central office. In the PON structure, the optical distribution network (ODN) connects the optical line terminals (OLTs) at the central office to the optical network units (ONUs) at the customer premises using only passive components to minimize operational costs. At the client side, the access network can terminate directly in a home (as in FTTH), multi-dwelling unit or business [15].

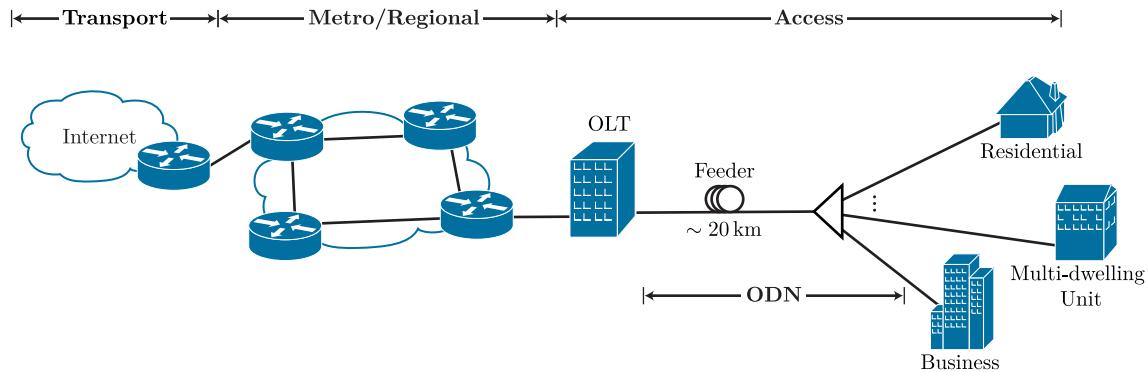


FIGURE 1–2: A general transport network with simple star topology PON.

For network providers, deploying a new fiber network is a tremendous financial investment which can take decades to complete [16]. From a hardware perspective, the economics of access networks differs greatly from that of metro and core transport networks. In addition, the competitive landscape for access services demands that customer hardware costs remain low, and that the cost per connection must be several orders of magnitude below that of the core network [17]. As a result, economics are the key driver for access network technologies [18].

The growth of consumer network traffic, dominated by Internet video and content distribution networks, makes a strong case for deploying FTTH as a future-proof access technology. Worldwide, FTTH adoption is growing with almost 80 million subscriptions in 2011 [19]. Optical access networks have the capability to support gigabit data rates over distances of tens of kilometres, which cannot be achieved with existing copper access networks. In fact, commercial FTTH services with symmetric data rates of 1 Gbit/s per user are already available in select markets [20], and service rates of 10 Gbit/s are projected to be introduced by ~ 2020 [21]. The future depends on providing increased data rates while minimizing the economic impact.

1.2 Review of the State of the Art

1.2.1 Current PON Technologies

In optical networks, the most common approaches to transmit several information channels over the same fiber link are time-division multiplexing (TDM) and WDM. In this section we introduce the current deployed TDM-based PON standards and a newly ratified standard based on a hybrid TDM and WDM.

Time-Division Multiplexed PONs

In TDM transmission systems, the data bits from different channels are interleaved in the time domain to create a composite data stream of continuous traffic [22]. In Fig. 1–3, we illustrate the basic operation of a TDM PON in a point-to-multipoint architecture. A continuous stream of bits from the OLT transmitter is composed of packets addressed to each of the ONUs on the tree topology. After propagating over the feeder fiber, a passive splitter equally divides the signal power among the N network branches where they are transmitted to the client side ONUs. The ONUs receive all of downstream packets, and recognize the data addressed to them by reading the packet headers. The OLT uses time-division multiple access to allocate transmission windows to each of the ONU clients in which they can make their uplink transmission and ensure that packet collisions do not occur.

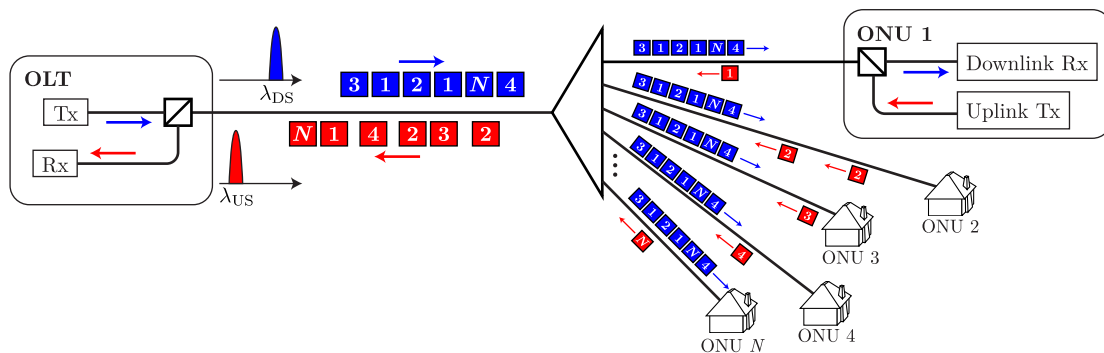


FIGURE 1–3: A basic TDM PON architecture.

Today, the most commonly deployed TDM PON standard is the gigabit-capable PON (GPON), typically supporting aggregate bandwidths of 2.488 Gbit/s downstream and 1.244 Gbit/s upstream over a 20 km feeder [23]. Coarse WDM separates the downstream and upstream wavelengths, λ_{DS} and λ_{US} , respectively. Although the GPON standards support a theoretical splitting ratio of up to

1:64, deployed configurations generally support either 16 or 32 ONUs per OLT, depending on the PON reach [24]. Assuming fair bandwidth assignment among all users on the PON, this limits the theoretical maximum rates to 78 Mbit/s and 156 Mbit/s downstream, and 39 Mbit/s and 78 Mbit/s upstream for 16 and 32 ONUs, respectively.

Recently, both the Institute of Electrical and Electronics Engineers and the International Telecommunication Union ratified TDM PON standards supporting up to 10 Gbit/s of aggregate downstream traffic, known as 10 Gbit/s Ethernet PON (10G-EPON) [25] and 10-Gigabit-capable PON (XG-PON) [26], respectively. Designed to be compatible with existing GPON infrastructure, these standards provide an upgrade pathway for network operators to meet consumer bandwidth demands in the short term without requiring any upgrades to the ODN infrastructure. Table 1–1 summarizes the main operating parameters of these three standards. With a 10 Gbit/s aggregate bandwidth and 32 ONUs, these newer standards still only support a maximum ~ 300 Mbit/s per user. Scaling TDM PONs beyond 10 Gbit/s poses many technological and economic challenges [27], which has opened up new avenues of research into hybrid TDM/WDM and pure WDM solutions to meet consumers' future bandwidth needs.

TABLE 1–1: Current TDM PON standards. DS: downstream, US: upstream.

	GPON [23]	10G-EPON [25]	XG-PON1 [26]
Standard	ITU-T G.984	IEEE 802.3av	ITU-T G.987
DS/US data rate (Gbit/s)	2.488/1.244 <i>asymmetric</i> 2.488/2.488 <i>symmetric</i>	10/1 <i>asymmetric</i> 10/10 <i>symmetric</i>	10/2.5 <i>asymmetric</i>
Split ratio	1:16, 1:32, 1:64	1:16, 1:32	1:32, 1:64
FEC	<i>optional</i> RS(255,239)	<i>mandatory</i> RS(255,223)	<i>mandatory</i> DS: RS(248,216) US: RS(248,232)
λ_{DS}	1480–1500 nm	1575–1580 nm	1575–1580 nm
λ_{US}	1260–1360 nm	1260–1360 nm	1260–1360 nm

Time- and Wavelength-Division Multiplexed PONs

In 2011, the Full-Service Access Network Group² began investigating technology options to increase PON bandwidths beyond 10 Gbit/s, known as next-generation passive optical network stage 2 (NG-PON2). In April 2012 time- and wavelength-division multiplexed (TWDM) PON was selected as the primary solution for the NG-PON2 standard [28]. Figure 1–4 illustrates the basic concept of the TWDM PON, which stacks multiple XG-PONs using coarse WDM to provide aggregate access rates of 40 Gbit/s downstream and 10 Gbit/s upstream using pairs of wavelengths $\{\lambda_1, \lambda_5\}$, $\{\lambda_2, \lambda_6\}$, $\{\lambda_3, \lambda_7\}$, and $\{\lambda_4, \lambda_8\}$.

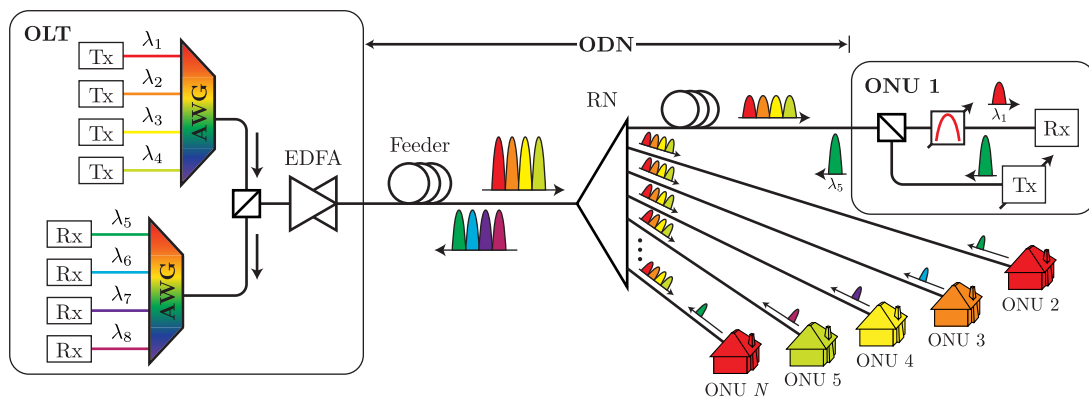


FIGURE 1–4: A basic TWDM PON architecture for NG-PON2.

The two major technology challenges for this solution occur at the client side, where the ONUs must be equipped with tunable transmitters and receivers to align their signals to any of these wavelength pairs. Meeting the performance requirements while maintaining the desired targets for cost and energy footprint is a challenging endeavour, but research is active in this area [28–31]. While TWDM PON is an attractive solution for network operators looking to provide FTTH services to a greater number of clients, like TDM PON it does not fundamentally address the projected bandwidth needs of consumers discussed in Section 1.1. The disadvantage of a traditional TDM PON is that the number of supported users, available user bandwidth and physical reach are limited due to power budget constraints by the passive power splitter at the RN [32]. A different solution

² The Full Service Access Network Group is a forum for the world’s leading telecommunications services providers, independent test labs, and equipment suppliers to work towards a common goal of truly broadband fibre access networks (<http://www.fsan.org>).

that leverages existing transport network WDM technologies in a cost effective manner will be required to meet the future targets of 10 Gbit/s per user [33–35].

1.2.2 Wavelength-Division Multiplexed PONs

Using WDM technology in PONs allows each customer to be assigned a unique communication wavelength and eliminates the need for data aggregation that limits the data rates of TDM solutions. At the same time, it provides enhanced security over point-to-multipoint solutions by enabling a virtual point-to-point connection between the client premises and the central office.

By leveraging and adapting mature technologies from transport networks, WDM PONs have the potential to supply vast amounts of bandwidth. However, since the technology choices in access networks are driven almost entirely by costs [15], we must adhere to some guiding design principles when engineering WDM PONs to ensure that the proposed solutions are economically viable for deployment [36]. For example, we must: 1) use colourless ONUs; 2) avoid using expensive external modulators; 3) use bidirectional single-fiber architectures; and 4) use optical amplifiers with restraint.

Physical WDM PON Architecture

Figure 1–5 illustrates an example WDM PON architecture. For practical deployment reasons the physical infrastructure is similar to the TDM case in Fig. 1–3, except that the optical power splitter at the RN is replaced with an athermal arrayed-waveguide grating (AWG) which does not require active cooling [37]. At the OLT, the downlink data is modulated onto different wavelengths $\lambda_1, \dots, \lambda_N$. An AWG multiplexes these wavelengths into a single optical fiber for transmission in the downstream direction. The ODN comprises a single feeder fiber and an AWG to demultiplex the client wavelengths onto each distribution drop fiber (DDF) which completes the short fiber span to the ONU transceivers located at the customer premises. A coupler at each ONU splits the downstream signal for detection and seeding of the uplink transmitter. In the upstream direction, uplink channels for different users are multiplexed at the RN and transmitted back to the OLT over the same feeder, where an AWG and circulators separate the individual channels for reception.

Colourless Optical Network Units

At the client side, it is essential to have generic ONU hardware that can operate irrespective of the transmission wavelength in order to eliminate the high cost and inventory redundancy that

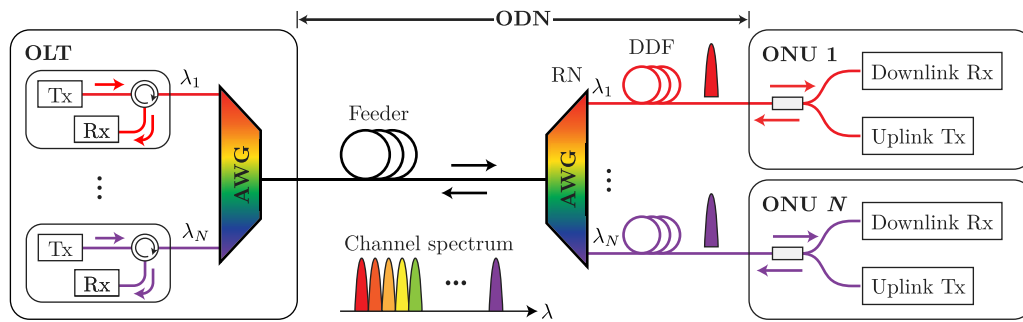


FIGURE 1–5: A basic WDM PON architecture with bidirectional transmission. Each client is assigned a single wavelength to communicate with the OLT.

would occur if each ONU model required a laser with a different wavelength. The two primary candidate technologies for these *colourless* ONUs are tunable lasers and reflective devices.

Tunable lasers. Distributed feedback lasers, multi-section distributed Bragg reflector lasers and microelectromechanically tuned vertical cavity surface emitting lasers are all possible technologies for tunable sources in access networks [29]. But to be a viable solution for WDM PON, the cost of these technologies must decrease significantly compared to current levels [29,38]. Potential methods of reducing device costs include omitting the thermoelectric cooler, wavelength locker and the integrated isolator, but doing so complicates the network’s design by requiring wavelength-control at the PON system level.

Development of inexpensive tunable sources is an ongoing research avenue [30,31,34,39], particularly in light of the recent ratification of the TWDM PON standard discussed in Section 1.2.1. Current solutions focus on low wavelength numbers (4 channels for NG-PON2), but a WDM PON with many channels spanning the optical C- and L-bands ($> 32\lambda$) will require broad tunability and high output power to overcome the ODN losses [29]. Although at this time no technology appears to be a clear candidate, future advancements may lead to better low-cost solutions for WDM PONs.

Reflective semiconductor optical amplifiers. An attractive option to eliminate the need for a tunable upstream optical source is to reuse a seed light transmitted centrally from the central office. The RSOA is a suitable device for this type of application and has numerous properties that make it attractive for use in WDM PONs. RSOAs boast a small form factor, low manufacturing cost, commercial availability, wide operating range over the optical C-band (1530 nm to 1565 nm), and their output can be directly modulated by applying a data signal to the bias of the gain medium [40].

Various approaches of providing seed wavelengths to the RSOAs have been investigated including spectrum-sliced broadband sources and remote continuous-wave (CW) laser seeding [41]. Currently, the most viable candidate architecture is a wavelength reuse scheme where a portion of the downstream signal is used to seed the reflective transmitter. This approach hinges on the gain clamping property of the RSOA which erases the downstream modulation from the seed light when the bias current and input optical power are sufficient for it to operate in the saturation regime [42].

Figure 1–6 illustrates downstream remodulation in WDM PONs. At the OLT, the downlink signal is modulated with a low extinction ratio (ER), that is, the modulation depth is small compared to the average optical power. At the ONU, a coupler taps off a portion of the downstream data for reception and the remaining light seeds the RSOA. If the bias current and input optical power are sufficient for it to operate in the saturation regime, the gain clamping property will help erase the downstream modulation from the seed light [42].

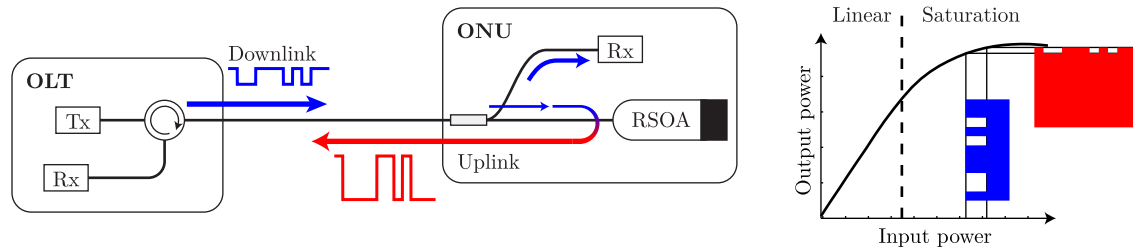


FIGURE 1–6: RSOA remodulation and downlink erasure with gain clamping. Details of the ODN have been omitted for clarity.

As illustrated in Fig. 1–6, the downlink erasure via gain saturation is imperfect, and some residual modulation remains and acts as intensity noise on the uplink signal. The uplink data can then be imprinted on the upstream signal by directly modulating the RSOA’s gain medium, sending data back to the central office on the same wavelength. The bidirectional performance can be carefully optimized by using a large ER for the upstream data and carefully tuning the downlink ER and the RSOA gain [40, 43, 44].

While this remodulation technique reduces the number of required AWG channels and provides cost advantages over tunable sources, bidirectional transmission on the same wavelength can severely limit upstream performance due to in-band crosstalk from reflections [45] and Rayleigh backscattering (RB) [46–48]. The RSOA’s gain saturation properties also effectively limit the PON’s reach to 20 km due to power budget limitations.

1.2.3 Challenges for High-Speed WDM PONs

RSOA Bandwidth Limitation

The primary limitation of RSOAs as colourless ONUs in next-generation systems is that their modulation bandwidth is fundamentally limited to ~ 3 GHz by the carrier lifetime of the gain medium, and often further reduced to ~ 2 GHz by parasitic leakage in the packaging electronics [49]. Figure 1–7 shows the measured modulation response for the commercial RSOA used throughout this thesis. Depending on the bias current, the RSOA has a modulation bandwidth of approximately 1.8 GHz to 2.2 GHz. A number of techniques have proven successful at further increasing the transmission bit rate upwards of 10 Gbit/s, falling into four major categories: electrical equalization, optical equalization, device structure and packaging optimization, and advanced modulation formats.

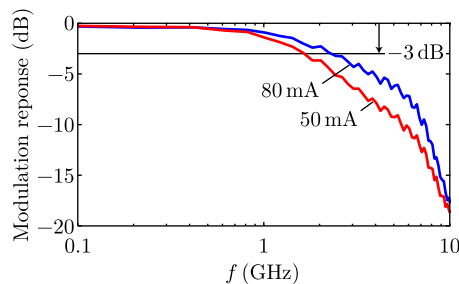


FIGURE 1–7: Measured modulation response of a butterfly-packaged RSOA (CIP SOA-RL-OEC-1550).

Electronic equalization. Modulating the RSOA with a signal beyond the -3 dB bandwidth leads to severe inter-symbol interference (ISI). As demonstrated in Fig. 1–7, the RSOA’s modulation bandwidth has a smooth roll-off with no spectral nulls. This makes it well suited for DSP based on the decision-feedback equalizer (DFE) [38, 50]. Using these electronic equalization techniques, 10 Gbit/s nonreturn-to-zero (NRZ) upstream transmissions have been demonstrated on a WDM PON using a 2.2 GHz RSOA and a DFE with 17 feedforward and 3 feedback taps [49]. Modulating a RSOA up to 25.78 Gbit/s has also been demonstrated in an optical back-to-back configuration [51], although the system is severely sensitive to dispersion and requires a dispersion compensating module for transmission over a feeder [52].

Maximum-likelihood sequence estimation (MLSE) is another electronic equalization technique that has been investigated for use with bandwidth-limited RSOAs [53–55]. Performance can be improved even further by combining MLSE and a partial response equalizer to form a partial response maximum likelihood equalizer. Combining the partial response maximum likelihood equalizer with optical filter detuning has been shown to enable 20 Gbit/s uplink transmissions over a 20 km feeder fiber [56]. Although solutions based on MLSE can achieve better performance than a DFE, they come at a cost of increased computational complexity.

Optical equalization. To achieve higher data rates, optical filtering techniques can also be used to compensate for the RSOA's limited modulation bandwidth. When an electrical signal is applied during data modulation, the refractive index changes in the RSOA generate a transient chirp in the transmitted signal. This chirping produces an undesired phase modulation along with the desired IM. Passing the chirped signal through a detuned optical filter transforms the unwanted phase modulation into IM, thereby increasing the RSOA's effective bandwidth [57]. This effect can be achieved using an offset optical band pass filter (OBPF) [57] or a delay interferometer [58]. A robust full-duplex 10 Gbit/s solution has been demonstrated [59] using this technique coupled with the DFE electronic equalization techniques discussed above. Additionally, offset filtering can also be used on its own in an effort to reduce the receiver's complexity [60].

RSOA structure and packaging. As noted previously, the RSOA's frequency response is limited by both the electron carrier dynamics and the parasitic leakage in the device packaging. A number of attempts have been made to improve the device's performance by optimizing the packaging and device structure. For example, a modulation bandwidth near that of the carrier lifetime (3.2 GHz) was demonstrated by carefully optimizing the butterfly packaging of a RSOA [51]. Additionally, the structure of the RSOA device itself can be tuned to improve performance, such as by extending the length of the gain medium [61] or by increasing the optical confinement in the active region [62, 63]. It should be noted that these three demonstrations were made in either an optical back-to-back configuration or over a dual-feeder PON configuration. Whether these improvements will be integrated into commercial RSOAs is still an unanswered question which depends entirely on the additional costs it would add to the device manufacturing process.

RSOAs can also be monolithically integrated with an electro-absorption modulator to overcome the bandwidth limitation due to direct modulation and achieve 10 Gbit/s data rates [64–66]. However, the device costs are significantly higher than for RSOAs.

Advanced modulation formats. Another means of increasing the data rates while working within bandwidth limitations is by using advanced modulation formats such as QAM which make it possible to transmit more than 1 bit of information per data symbol. These modulation formats are commonplace in the current generation of transport networks [67,68]. Applications of higher-order modulation have been investigated to some degree for access networks applications including direct duobinary modulation [69], 4-ary pulse amplitude modulation (PAM) [70], QPSK [71], orthogonal frequency-division multiplexing [72,73], discrete multi-tone [74], and carrierless amplitude and phase modulation [75].

These spectrally efficient formats alleviate some of the RSOA bandwidth restrictions because their baud rate is lower than that of a binary signal for the same data rate. This smaller signal bandwidth also reduces the impact of chromatic dispersion [22]. However, using advanced modulation formats increases the complexity of the transceivers and impacts the receiver sensitivity [50], so it is important to select modulation formats that do not require expensive external modulators when engineering solutions for next-generation PONs.

Due to the high cost of coherent transceiver components (e.g., external modulators, optical hybrids), applications based on coherent technologies focus primarily on long reach PONs (> 20 km) for rural installations [71,76,77]. The performance benefits of its superior receiver sensitivity make it more practical in that scenario compared to traditional IM and DD, even at a higher deployment cost.

Upstream Impairments From Bidirectional Transmission

In order to provide a cost-effective upgrade path for existing PON deployments, WDM PONs will be required to operate bidirectionally over a single feeder fiber [36]. For systems implementing colourless ONUs that use the same wavelength for full-duplex communication, in-band crosstalk due to RB and reflections impose severe limitations on uplink channel performance [45–47,78]. The primary sources contributing to RB and reflections in bidirectional PONs are illustrated in Fig. 1–8.

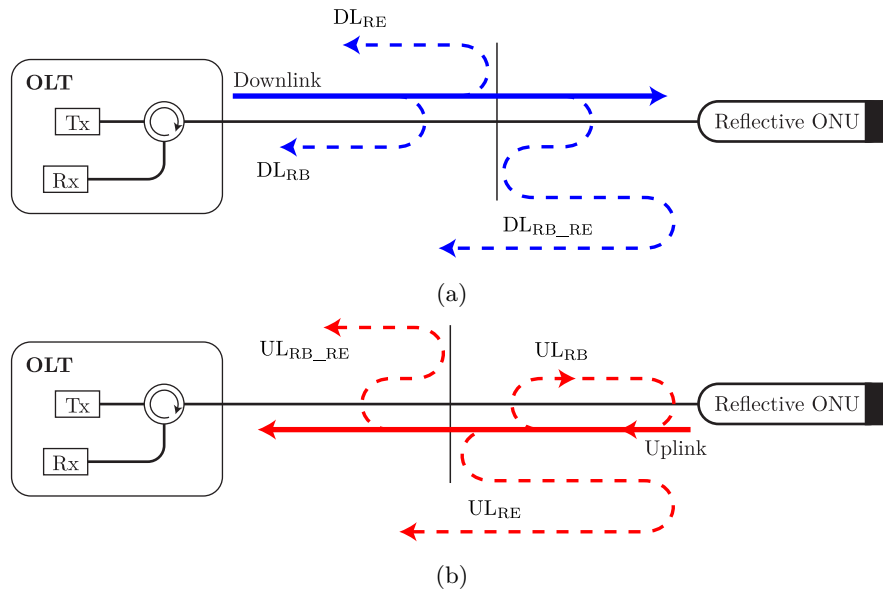


FIGURE 1–8: The contributions of upstream impairments due to (a) downlink and (b) uplink transmissions. The vertical lines represent a static reflection. Details of the ODN and ONUs have been omitted for clarity.

Figure 1–8(a) shows the contributions from the downlink signal, sometimes referred to as the carrier.³ DL_{RB} is the backscattering of the downlink signal, DL_{RE} can occur from reflections of the downlink signal due to static discontinuities (e.g., connectors, splices), and DL_{RB_RE} is the possible reflection of the backscattered signal in the upstream direction [46,47]. Of these three components, DL_{RB} is always present and reaches a constant value for fiber lengths of 20 km or greater [79], while the latter two only occur if a reflection is encountered.

Figure 1–8(b) illustrates the contributions of the uplink signal to the upstream impairments. The most detrimental element is the backscattering of the uplink data signal, UL_{RB} , which is amplified and re-transmitted by the ONU, creating a feedback loop. Similar to above, UL_{RE} can occur due to static reflections and UL_{RB_RE} is the reflection of the backscattered uplink signal in the downstream direction [46,47].

Optical isolators cannot be used to suppress reflections in single feeder PONs due to the bidirectional transmission. However, using optical connectors with oblique end faces (such as FC/APC)

³ In WDM PON architectures that use CW seeding, the seed signal is referred to as the downstream *carrier*. The carrier does not interact with the downlink data transmission because they operate on separate wavelengths.

and fusion splices throughout the network can reduce the impact of static reflections by maintaining optical return losses of better than 55 dB [80]. Therefore, RB will generally be the most dominant contribution to the upstream impairments [46].

It is important to note that the power spectral density of the RB is *coloured*, that is, the spectral content of the RB is proportional to that of the corresponding optical signal [81]. Additionally, severe optical beat interference (OBI) can occur when the downstream seed light is a coherent single-frequency laser source [82]. In this case, the OBI's frequency content is dependent on the line width of the laser source [83].

Mitigating Upstream Impairments

For WDM PONs to be feasible for next-generation deployments, the impact of these impairments must be reduced to acceptable levels while respecting the performance requirements and economic boundaries imposed by network operators. In this section we discuss a number of proposed solutions from the literature that aim to minimize the impact of upstream impairments on the performance of single feeder bidirectional WDM PONs with wavelength reuse.

ONU gain optimization. The optical signal to RB ratio (OSRBR) for the downlink and uplink signals due to the primary contributions from DL_{RB} and UL_{RB} is derived in Appendix A.1. Assuming that the OLT launch power is less than 7 dBm, the uplink channel's OSRBR is given by Eq. (A.7) as

$$OSRBR_{UL} \simeq \frac{g_{ONU} \cdot l^2}{\zeta(1 + g_{ONU}^2 \cdot l^2)},$$

where g_{ONU} is the gain of the reflective ONU, l is the total loss for a single trip through the fiber and ζ is the ratio of backscattered power to launched power. ζ can be considered a constant for a 20 km feeder and a launch power of less than 7 dBm.

The upstream impairments primarily depend on the ONU gain and the ODN losses. Carefully selecting these operating parameters and using components with high return loss values has been shown to minimize the impact on the upstream transmission in systems with NRZ modulation [84]. However, tuning g_{ONU} at the client side may be impractical for economic and complexity reasons in deployed systems, as each of the customer links will have different ODN losses and will require individual optimization.

Radio frequency subcarrier multiplexing. One method of eliminating the restrictions on g_{ONU} is to filter out the inter-channel crosstalk from the data signals using a combination of

RF SCM and electrical filtering [40]. SCM is a method of generating one or more passband signals in the electrical domain and transmitting them en masse over a high-speed optical link [85]. The optical signal containing all of the SCM channels is then detected at the receiver, where the channel of interest can be isolated using simple electrical filtering. A mathematical description of SCM can be found in Appendix A.2.

A basic concept of using SCM in a WDM PON is illustrated in Fig. 1–9. In this example, the downlink NRZ data is mixed with a RF subcarrier f_{DL} and occupies the upper portion of the electrical bandwidth. The downstream optical carrier is then modulated with the band pass downlink signal. After propagating over the ODN and photodetection at the ONU, the received band pass signal is mixed with a phase matched subcarrier to down-convert it to baseband. A coupler taps off a portion of the downstream signal to seed the RSOA transmitter.

For the upstream transmission, the uplink channel's NRZ data is up-converted onto a RF subcarrier f_{UL} which then directly modulates the RSOA's gain medium. After propagation over the ODN, the OLT receiver detects the upstream signal containing both the desired uplink passband signal centred at f_{UL} and the high frequency noise from the downlink channel due to RB, reflections and incomplete data erasure at f_{DL} . This spectral separation allows the down-conversion and low pass filter (LPF) stages to isolate the uplink signal from the out-of-band downlink noise.

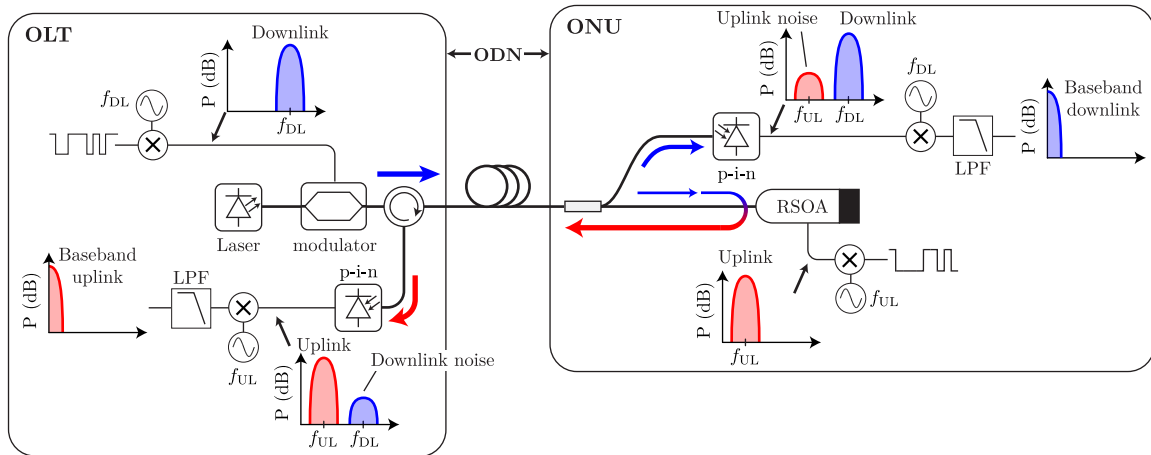


FIGURE 1–9: A basic SCM WDM PON architecture with bidirectional transmission, wavelength reuse and downlink remodulation. Low bit rates are assumed to accommodate the uplink channel within the RSOA's modulation bandwidth and details of the ODN have been omitted for clarity.

WDM PONs implementing SCM have been generally limited to symmetric data rates of 1.25 Gbit/s [86] or asymmetric rates of 2.5 Gbit/s downstream and 1.25 Gbit/s upstream [87–89] due to the low spectral efficiency of NRZ signals and the bandwidth constraints of low cost optoelectronic components. Recently, however, a symmetric 10 Gbit/s SCM WDM PON was demonstrated using a directly modulated laser [90], but it required a cost prohibitive high bandwidth photodetector at the ONU. Determining a means of producing spectrally efficient channels will be essential for the adoption of SCM in high-speed WDM PONs.

Advanced modulation formats, line coding and digital signal processing techniques.

Different modulation formats and data codings of the downlink channel have been investigated as a means of reducing the crosstalk and noise on the upstream signal [91]. Transmitting the downlink signal with differential phase-shift keying [92] or frequency-shift keying [84] results in a constant amplitude seed source for the RSOA. The performance is similar to that of a CW seed source but comes at the cost of additional complexity to the ONU receiver.

Encoding the data channels in different formats (e.g., Manchester, 8b10b, duobinary) has also been shown to mitigate the effects of RB [93–95]. These approaches are fairly similar, in that they reduce the DC component of the transmitted signal which facilitates removal of the low frequency OBI using an electrical high pass filter after photodetection [96,97]. Similar to SCM, the symmetric data rates are limited to well below 10 Gbit/s by the low spectral efficiency of the encoded signals and the optoelectronic device bandwidths of the transceivers.

DSP approaches have also been proposed to help mitigate upstream impairments. A quantized feedback equalizer has been shown to reduce the impact of the low frequency OBI contribution for upstream signals at 2.5 Gbit/s [98]. Additionally, the contribution of the coloured feedback noise from the RSOA can be mitigated with a noise predictive equalizer [99]. It should be noted that these demonstrations were performed with CW seeding and as a result neglect the impact of crosstalk and noise due to the downlink modulation.

1.3 Problem Statement and Research Objectives

Optical access networks based on WDM PONs offer higher potential data rates and greater security than existing TDM PONs. However, their viability for commercial deployment hinges entirely on economic factors. To be adoptable, it is imperative that the client side hardware must be colourless to reduce inventory redundancy and be comparable in cost to competing solutions.

RSOA-based ONU transmitters with wavelength reuse and downlink data remodulation are a well researched solution for WDM PONs, but symmetric data rates are limited by the RSOA's modulation bandwidth and upstream impairments due to bidirectional transmission. SCM is a simple and inexpensive technique to reduce the impact of inter-channel crosstalk due to RB and reflections, but it further reduces symmetric data rates due to the transmission channels' low spectral efficiency.

The primary objective of this thesis is to investigate and experimentally demonstrate new approaches to using SCM in WDM PONs while still respecting the economic and architectural constraints required by the industry. Specifically, we aim to achieve 10 Gbit/s symmetric transmission rates to meet the projected bandwidth demands for future optical access networks.

1.4 Thesis Overview

Here in Chapter 1, we introduced optical access networks as a leading candidate technology to meet consumers' future bandwidth demands. We thoroughly reviewed the state of the art from the literature and presented WDM PONs as a candidate technology for next-generation optical access networks. We further detailed the key technical challenges that must be addressed for commercial viability. The remainder of this thesis is organized as follows:

Chapter 2 outlines a collaborative project with industry partner Bell Canada to develop a bandwidth provisioning tool for their deployed GPON network. We use a Gaussian bandwidth distribution model from the literature and implement a numerical software tool with simple empirical inputs to estimate the capacity of the TDM PON's aggregate uplink connection.

In Chapter 3 we propose a novel O-SCM WDM PON to increase the symmetric data rates in WDM PONs with bidirectional transmission and RSOA-based ONUs. We demonstrate that allowing some spectral overlap between the RF channels improves the bandwidth efficiency at the expense of additional noise and inter-channel crosstalk. We experimentally demonstrate 1.5 Gbit/s full-duplex transmission over a 20 km bidirectional WDM PON and achieve BERs less than 10^{-10} . We then analytically derive the system's optical power budget and look at operating constraints due to the RSOA modulation bandwidth and the RF mixers. We further refine the O-SCM architecture and replace the OLT's external modulator with a more economical integrated transmitter. We experimentally optimize the system's optical power budget and demonstrate 2.5 Gbit/s full-duplex transmission with BERs below 10^{-10} . Furthermore, we demonstrate an O-SCM WDM PON with

a stand-alone BM receiver at the OLT to perform clock and data recovery, instantaneous phase acquisition and RF down-conversion of the 2.5 Gbit/s uplink channel.

Chapter 4 presents a 5 Gbit/s O-SCM WDM PON with an improved RF channel allocation scheme. We develop a DSP-based offline analysis framework to electronically equalize the uplink signal and remove the ISI that results from the bandwidth-limited RSOA transmitter. We achieve full-duplex operation and characterize the system's BER over a 20 km single feeder PON.

Chapter 5 provides an introduction to implementing higher-order M -ary QAM (M-QAM) and pulse shaping with IM/DD optoelectronics. We further outline the key building blocks of the 10 Gbit/s SCM WDM PON architecture including the development of new offline transmitter and receiver DSP stacks, spectral pre-compensation, offset optical filtering and a characterization of the upstream impairments.

Chapter 6 describes a series of experiments with the M-QAM SCM WDM PON architecture developed in Chapter 5 at data rates of 10 Gbit/s and beyond. We propose three uplink/downlink channel configurations: 1) QPSK/QPSK; 2) QPSK/16-QAM; and 3) 16-QAM/16-QAM. In each case we experimentally characterize the system's full-duplex operation over a 20 km single feeder WDM PON in terms of BER. The efficacy of DSP spectral pre-compensation is verified and we demonstrate the uplink channel's resilience to upstream impairments such as RB, reflections and stimulated Brillouin scattering (SBS). We then further optimize the ODN and operating parameters to increase the channel line rates to 11.25 Gbit/s and account for the FEC overhead. We then demonstrate the architecture's flexibility by directly comparing the BER performance of all permutations of QPSK and 16-QAM channels on a fixed optical test bed.

We conclude this thesis in Chapter 7, where we summarize the key concepts and highlight our contributions to the field of study. Additionally, we suggest research directions that will be important for the future development and adoption of WDM PONs.

CHAPTER 2

Bandwidth Capacity Estimation for a Deployed Gigabit-Capable PON

AN OPERATOR'S ABILITY to accurately forecast bandwidth usage on their network is paramount to their business. A delicate balance must be maintained between over allocating capacity, which wastes resources and capital, and under allocating capacity, which could starve clients of essential services. This chapter describes the work completed in partnership with engineers at Bell Canada to develop a software tool that helps to estimate the network's bandwidth capacity during the deployment process of their Bell Fibe™ fiber optic based residential service.¹ This project provided foundational knowledge of real-world industry concerns which proved invaluable in the research described in later chapters.

This chapter is organized as follows: Section 2.1 briefly introduces the project goals and a generalized network architecture. Section 2.2 summarizes the bandwidth model and Section 2.3 outlines a usage example. Finally, the chapter is concluded in Section 2.4.

2.1 Introduction

Figure 2-1 illustrates a generalized architecture for a GPON as part of an operator's network. Each PON tree connects up to 32 client ONUs to the network operator's central office through a TDM architecture consisting of a DDF, optical power splitter and a feeder fiber. At the central office, a rack of OLT cards combines the PON data traffic from all of the active clients onto an aggregate connection to the operator's IP network. Here we assume that N is the total number of active clients during peak activity periods. The data traffic capacity of this aggregate link, highlighted in red, has to be carefully managed as client subscriptions increase and additional ONUs are added to the PONs. The engineers at Bell identified this link as a primary bottleneck

¹ Bell Fibe™ is a triple-play FTTH/FTTN service offering Internet, television and telephony (<http://www.bell.ca/Fibe-TV>).

during initial deployment and an upgrade path for future growth of the service. It is therefore the focus of our efforts.

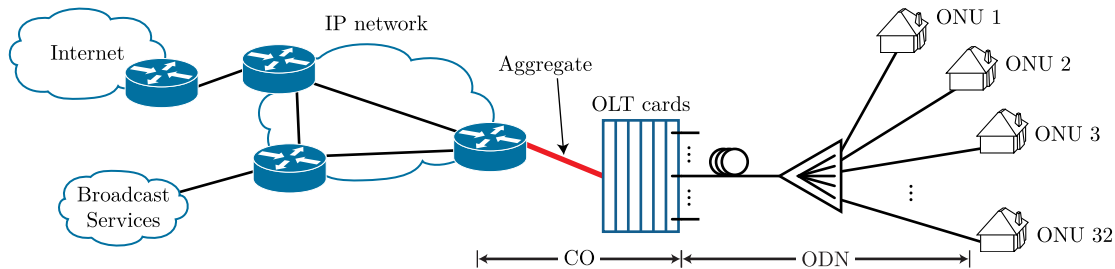


FIGURE 2–1: An example of a deployed GPON architecture. The aggregate connection between the PONs and the operator’s IP network is highlighted in red.

2.2 Modelling GPON Bandwidth Capacity

In addition to providing high-speed Internet access, FTTH subscriptions typically comprise a variety of services including high-definition broadcast IP television, video on demand and voice over IP telephony as added revenue streams for the network operator. For Bell’s GPON we first focused on modelling the aggregate link’s capacity to support high-speed Internet service to customers using a Gaussian model based on work by Haßlinger [100–102] and Hartleb [103]. A portion of the aggregate capacity is reserved to account for the other FTTH services.

2.2.1 Extreme Capacity Estimates

In general, access network providers offer consumers a choice of data rates for their HSI services. These subscription levels are usually defined by the maximum peak bit rates offered to the clients at various price points. However, due to variability of Internet traffic, mean data rates can often fall well below the peak rates [104]. Here we can use the mean and peak rates to estimate the *best-* and *worst-case* scenarios for estimating the aggregate link’s capacity.

The most desirable scenario for a service provider is when each active client uses only their mean bandwidth, providing a relatively predictable capacity for the network. We can estimate this best-case capacity as

$$C_{\text{HSI},\min} = \sum_{i=1}^N \mu_i, \quad (2.1)$$

where μ_i is the mean data rate for each of the N active clients. However, because μ_i is generally much less than the client's subscribed capacity, this can provide a drastic underestimate during peak traffic periods.

At the other extreme, the least desirable situation is when each client is using their maximum subscribed rate, C_i . We can then estimate this capacity as

$$C_{\text{HSI,max}} = \sum_{i=1}^N C_i. \quad (2.2)$$

This overestimates the network traffic and leads to underutilized capacity. Neither of these scenarios are realistic estimates, but they provide the upper and lower bounds for the capacity estimates in the next section.

2.2.2 Gaussian Bandwidth Capacity Model

The bursty nature of data traffic on the Internet is a well known phenomenon [105]. At longer time scales (> 1 s) the distribution of this bursty traffic has been shown to approach that of a Gaussian due to the statistical multiplexing nature of these networks [100, 106, 107]. This is generally considered to be a good approximation, although there are increasing deviations in the outer ranges greater than $|2\sigma|$ from the mean [102].

In formulating our model, we need to first estimate the amount of data accessed by each user on the network. The traffic on an aggregated network link is usually generated by statistically independent sources, therefore the mean and variance of the aggregate supply can be computed as the sum of the mean and variance of each involved source by way of the central limit theorem [103]. Although likely an over estimate [108], we can approximate that the mean data rate and standard deviation of the aggregated network link are given by

$$\mu_R \approx \sum_{i=1}^N \mu_i \quad (2.3)$$

$$\sigma_R \approx \sqrt{\sum_{i=1}^N \mu_i (C_i - \mu_i)}, \quad (2.4)$$

for a superposition of N independent data sources with different subscribed access capacities C_i and mean per user data rates μ_i .

Deployed TDM PON systems, such as GPON, can prevent packet losses and improve customer quality of service by using buffering to smooth out some of the bursty traffic. Here we model the

system using a bufferless approach to provide a simplified worst case scenario [103]. The general bufferless model begins with the loss probability p_{loss} , often called the blocking probability, which is given by the ratio of the mean loss rate r_{loss} to the mean traffic rate μ_R .

$$p_{loss} = \frac{r_{loss}}{\mu_R} \quad (2.5)$$

$$r_{loss} = \int_{x>C} (x - C) dF_R(x), \quad (2.6)$$

where generally F_R is the rate distribution function, $C = \mu_R + m \cdot \sigma_R$ is the required capacity and m is a multiplier of the standard deviation σ_R in excess of the mean rate μ_R [102]. Here, we replace F_R with a Gaussian rate distribution function and simplify, resulting in

$$p_{loss} = \frac{\sigma_R}{\mu_R} \cdot (\phi(m) - m \cdot \Phi(m)), \quad (2.7)$$

where

$$\phi(m) = \frac{1}{\sqrt{2\pi}} \cdot e^{-\frac{m^2}{2}}$$

$$\Phi(m) = \int_m^{\infty} \phi(x) dx.$$

The resulting Eqs. (2.3), (2.4) and (2.7) can be combined to provide a closed form analytical solution which can be solved numerically to determine the required link aggregate capacity for high-speed Internet access, $C_{HSI,Gaussian} = C(\mu_R, \sigma_R, p_{loss})$.

2.3 Usage Example

Using the Gaussian capacity model outlined in the previous section, we built a numerical software package to estimate the network capacity of the aggregate connection in Fig. 2-1 and provide a visual tool for the network operator to project growth requirements. In this section we will provide an example to illustrate the tool's utility.

Figure 2-2 shows an example client subscription distribution for the available high-speed Internet service, assuming that the aggregate supports up to $N = 1000$ active clients. Given the service distribution information along with an assumed $p_{loss} = 10^{-6}$, we can numerically solve Eq. (2.7) over a range of μ_i and N using the Newton-Raphson method.² In the contour plot in Fig. 2-3, we

² See Appendix A.3 for more details.

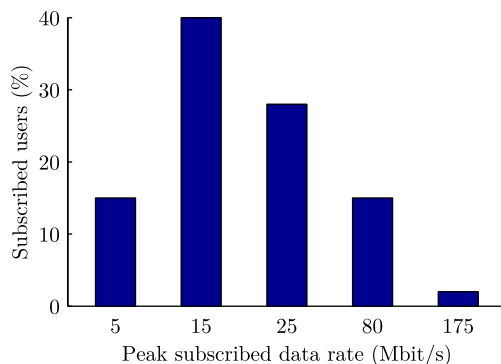


FIGURE 2–2: An example client subscription distribution for a GPON high-speed Internet service.

define three operating regions that depend on the available total capacity of the link connecting the PONs to the operator’s IP network. These define situations where the aggregate link connecting the rack of OLT cards to the IP network may be upgraded to support more users. The contour values (1 Gbit/s, 2 Gbit/s and 4 Gbit/s) are defined by the upgrade path of the hardware. Additionally, we define the oversubscription factor [104]

$$\mathcal{F}_{os} = \frac{N_{Gaussian}}{N_{max}} \quad (2.8)$$

where $N_{Gaussian}$ and N_{max} are the number of users supported by the Gaussian model and worst-case peak bandwidth provisioning, respectively. \mathcal{F}_{os} is a measure of how *aggressively* an operator wants to statistically multiplex the bandwidth provided to its users, with typical values ranging from 5 to 20.

In order to illustrate the usefulness of this tool, we look at two example scenarios in Fig. 2-3. In the first scenario, the initial state is marked with a (o) in region I with 400 subscribers and a mean per user data rate $\mu_i \approx 1$ Mbit/s. The network operator can empirically determine μ_i for different periods of the day using their internal usage statistics. In this case the 1 Gbit/s aggregate link can support up to 475 active clients while maintaining a \mathcal{F}_{os} between 10 and 15. If the number of subscribers on the PON increases by 50% to 600 clients, while maintaining a constant μ_i , the operating point (Δ) moves to region II where the aggregate link must be upgraded to 2 Gbit/s in order to maintain $\mathcal{F}_{os} \sim 15$.

In the second scenario we will look at the effect of an increase in data consumption over a short period of time, where the client base remains constant. This could occur, for example, with

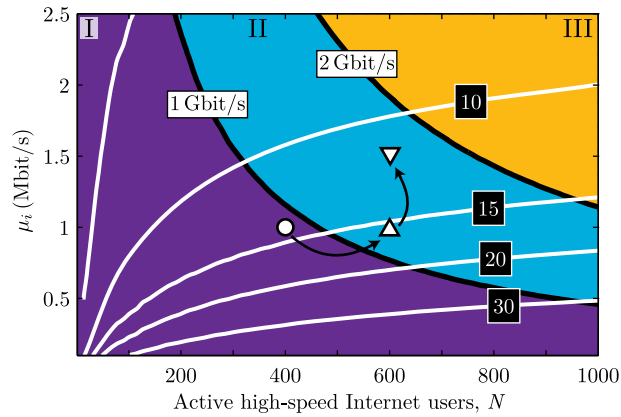


FIGURE 2–3: A typical contour plot from the Gaussian bandwidth capacity tool. The coloured regions define operating ranges for total available aggregate bandwidth for the PON. The white overlay contours show at what \mathcal{F}_{os} the network is operating.

the introduction of a new on-demand streaming Internet video service by a third party provider. Here the operating point moves vertically (∇) if μ_i increases by 50% to 1.5 Mbit/s. In this case the PONs are still operating well within region II with an aggregate link speed of 2 Gbit/s and \mathcal{F}_{os} between 10 and 15.

2.4 Summary

In this chapter we demonstrated a software tool that a network operator can use to gauge the health of their network and plan for future network upgrades. The model uses simple empirical inputs and subscriber distribution information to estimate the bandwidth capacity of the aggregate connection between the PONs and the operator’s IP network. This analytical tool can be further extended to include additional client services such as broadcast IP television, voice over IP telephony and video on demand. However, these extensions depend heavily on the network architecture, hardware and the choice of services offered by the operator and were therefore not considered in this thesis.

CHAPTER 3

Overlapped-Subcarrier Multiplexing for WDM PONs

SUBCARRIER MULTIPLEXING is a simple and attractive approach to mitigate the upstream impairments in reflective WDM PONs, but symmetric transmission data rates have been limited by inefficient bandwidth implementations. In this chapter we will introduce the concept of O-SCM to improve the symmetric data rates in WDM PONs with downlink remodulation and RSOA-based ONU transmitters without significantly increasing the transceivers' cost or complexity when compared to other SCM solutions.

This chapter is organized as follows: Section 3.1 introduces the concept of O-SCM for bidirectional WDM PONs and compares it to traditional SCM solutions. In Section 3.2 we outline the first experimental demonstration at 1.5 Gbit/s and evaluate the system's performance in terms of BER. We also present an analytical model of the optical power budget and discuss some basic design constraints. Section 3.3 details a second experimental demonstration with full-duplex 2.5 Gbit/s transmission over a 20 km PON using a more economical downlink transmitter. Important system parameters are characterized, and we then verify the system's BER performance. Section 3.4 outlines a collaborative experiment to demonstrate the BM reception of an O-SCM WDM PON uplink channel at 2.5 Gbit/s. Finally, the chapter is summarized in Section 3.5.

3.1 Overlapped-Subcarrier Multiplexing

As introduced in Section 1.2, SCM is a promising technique to mitigate the impact of upstream impairments by separating the frequency spectra of the uplink and downlink channels in the electrical domain. This separation enables the suppression of in-band crosstalk due to RB and reflections through simple electrical filtering [40, 86, 87]. The main drawback of separating the channels with SCM is that it results in low bandwidth utilization, and therefore a reduced spectral efficiency. Without channel separation, the system performance is severely limited by crosstalk. As noted in Section 1.2.3 this is particularly detrimental to the upstream transmission.

As a compromise, we propose an overlapped-SCM approach where a portion of the downlink noise spectrum is allowed to overlap with a portion of the uplink channel. This allows us to further investigate the design trade-off between bandwidth efficiency and crosstalk. Figure 3–1 illustrates the concept of the O-SCM approach and compares it to two example conventional SCM implementations.

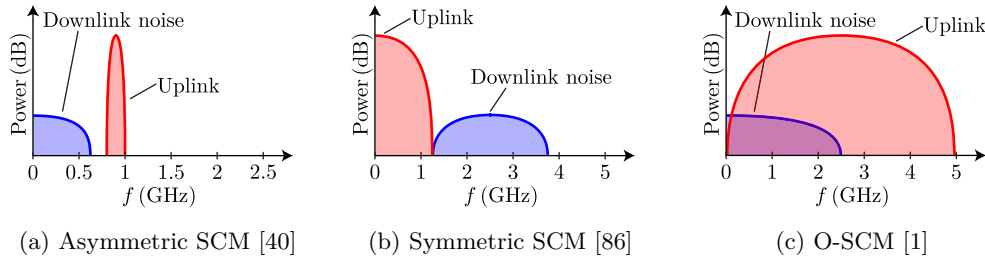


FIGURE 3–1: The upstream RF channel allocation as detected at the OLT for three different SCM approaches.

In Fig. 3–1(a) we see the case of asymmetric transmission channels, where the 100 Mbit/s uplink channel on a 0.9 MHz subcarrier is separated from the residual noise of a 622 Mbit/s baseband downlink channel. A guard band separates the two channels to facilitate electrical filtering at the OLT receiver. The data rates are kept well below 1 Gbit/s to ensure that the uplink channel resides within the modulation bandwidth of the RSOA.

Figure 3–1(b) illustrates the channel allocation of a more conventional SCM implementation with symmetric 1.25 Gbit/s data rates. The two channels are tightly packed, with the first-null bandwidth of the baseband NRZ uplink channel adjacent to that of the downlink channel noise. In this example the downlink channel is placed on a 2.5 GHz subcarrier, allowing the baseband uplink channel to operate within the RSOA bandwidth. A LPF at the OLT will greatly reduce the downlink crosstalk after photodetection.

The concept of an O-SCM channel allocation is shown in Fig. 3–1(c). We see that the 2.5 Gbit/s uplink channel is on a 2.5 GHz subcarrier, with a first-null bandwidth extending from 0 GHz to 5 GHz. Half of this channel overlaps with the residual noise from the 2.5 Gbit/s baseband downlink channel. This increases the data rates and bandwidth utilization efficiency at the expense of an acceptable performance penalty due to the crosstalk.

3.2 Initial Demonstration at 1.5 Gbit/s

In this section we present the first demonstration of an O-SCM WDM PON architecture that aims to increase resiliency to upstream impairments compared to baseband remodulation techniques, while providing more efficient bandwidth utilization than conventional SCM techniques [5]. Experiments during the initial investigation are performed at relatively moderate data rates to reduce the effect of the RSOA's limited modulation bandwidth.

3.2.1 Physical PON Architecture

Figure 3-2 illustrates the architecture of the O-SCM WDM PON, which respects the existing infrastructure constraints and design guidelines described in Section 1.2.2. The OLT transmitter comprises a Mach-Zehnder modulator that externally modulates a 1550.08 nm distributed feedback laser at 1.5 Gbit/s with a NRZ $2^{15} - 1$ pseudo-random bit sequence (PRBS). The Mach-Zehnder modulator is biased so that the downlink NRZ signal has an ER < 2.5 dB. An erbium-doped fiber amplifier (EDFA) and a variable optical attenuator (VOA) control the OLT launch power $P_{\text{OLT_Tx}}$ at the output of the circulator. The ODN comprises a 20.35 km feeder of standard single mode fiber (SMF-28e+), a 100 GHz AWG and a 1.5 km DDF. At the ONU, 10% of the downstream signal is tapped off for detection by the receiver comprised of a p-i-n photoreceiver, a RF amplifier and a LPF¹ to remove out-of-band noise. The remaining 90% of the downstream signal seeds a RSOA with peak gain from 1530 nm to 1570 nm and 2 GHz modulation bandwidth. The 90% coupling ratio facilitates downlink erasure and remodulation by ensuring that the RSOA operates in the saturation regime.

The uplink transmitter consists of a pulse-pattern generator that outputs a 1.5 Gbit/s NRZ $2^{31} - 1$ PRBS which is amplified and then mixed with a RF subcarrier $f_{\text{UL}} = 1.5$ GHz. A bias-tee provides the amplified $4 V_{\text{p-p}}$ signal with a 50 mA bias current to ensure that the uplink operates at ER $\gg 2.5$ dB. The OLT receiver consists of a 50 GHz OBPF to remove out-of-band optical amplified spontaneous emission noise, and a p-i-n photodiode. The upstream signal is then converted back to baseband using a phase-matched local oscillator at 1.5 GHz and a matching mixer. Finally, a LPF¹ removes out-of-band noise.

¹ Picosecond 4th order Bessel-Thomson (933 MHz bandwidth)

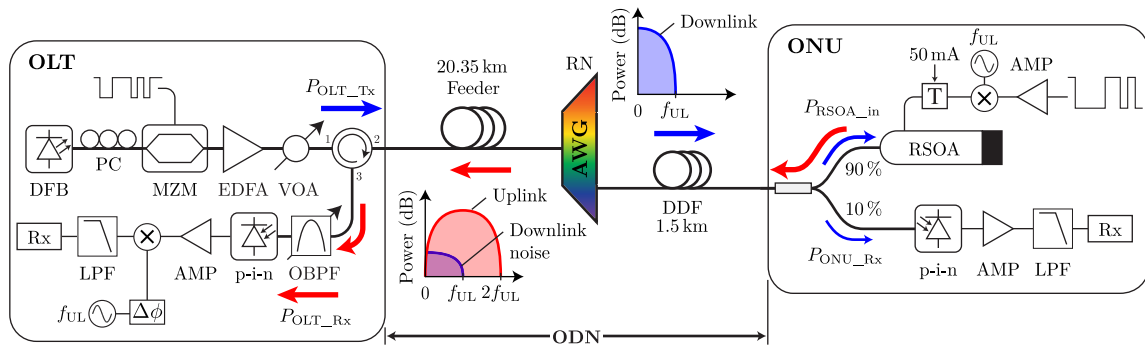


FIGURE 3–2: Physical architecture of the 1.5 Gbit/s O-SCM WDM PON. The downlink NRZ signal is sent at baseband, while the uplink is placed on a 1.5 GHz RF subcarrier. $\Delta\phi$: electrical phase delay, AMP: RF amplifier, AWG: arrayed waveguide grating (100 GHz channel spacing), Mixers: Mini-Circuits ZX05-C42MH, MZM: Mach-Zehnder modulator, OBPF: JDS Fitel TB9 (50 GHz bandwidth), PC: polarization controller, p-i-n: HP 11982A (12 GHz bandwidth), RSOA: CIP SOA-RL-OEC-1550, T: RF bias-tee.

3.2.2 Optical Back-to-Back Performance

To first characterize the system in a reference optical back-to-back configuration, both the feeder and DDF are removed from the setup in Fig. 3–2 in order to eliminate the RB contribution. The BER performance in terms of received optical power is shown in Fig. 3–3.

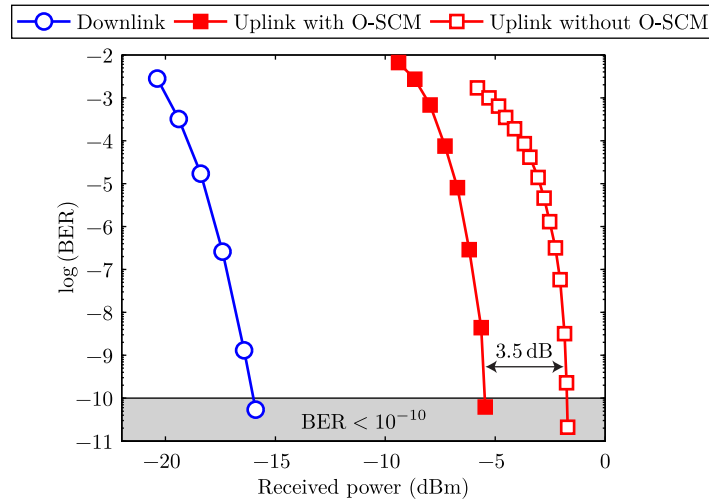


FIGURE 3–3: Measured BER performance of the 1.5 Gbit/s O-SCM system in an optical back-to-back configuration.

The downlink transmission performs well, with a sensitivity of approximately -16 dBm to achieve a $\text{BER} < 10^{-10}$. Two different configurations of the uplink were tested, both with and without O-SCM. For the case without O-SCM, we removed the RF mixers but the rest of the

transceivers remained the same. Here we see that O-SCM reduces the inter-channel crosstalk and lowers the minimum optical power to operate at $\text{BER} < 10^{-10}$ by more than 3.5 dB.

3.2.3 Full-Duplex Operation Over a 20 km WDM PON

We replace the feeder fiber and DDF to continue the characterization in a more realistic symmetric scenario. In Fig. 3–4 the downlink channel, which is largely unaffected by crosstalk, performs similarly to the back-to-back case. For the uplink channel without O-SCM, an error floor is reached at $\text{BER} \sim 10^{-9}$. With the aid of O-SCM, the uplink channel achieves a sensitivity of -10 dBm. Comparing the uplink and downlink channels, there remains a 6 dB penalty in sensitivity due to the impact of upstream impairments.

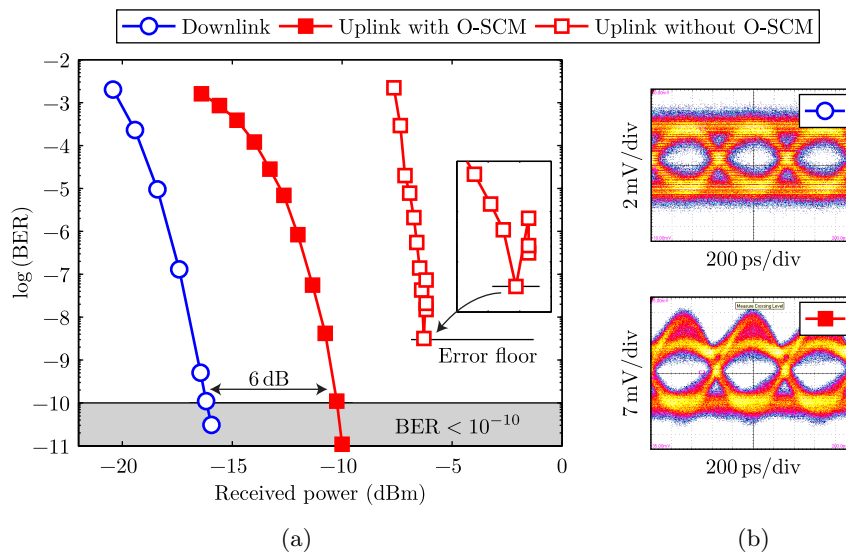


FIGURE 3–4: Bidirectional performance of the 1.5 Gbit/s O-SCM architecture over a 20 km WDM PON as a function of received power. (a) Measured downlink and uplink BERs. The inset clarifies the existence of an error floor near 10^{-9} in the case without O-SCM. (b) Example eye diagrams at $\text{BER} \sim 10^{-10}$.

It is interesting to note the performance difference between Figs. 3–3 and 3–4. We see that the downlink performs consistently but the uplink sensitivity is actually *worse* in the back-to-back case. This is likely due to the additional contribution of noise from the RSOA due to any reflections in the system. As noted in Section 1.2.3, the impact of impairments originating from the uplink signal can be minimized by tuning the ONU gain to 3 dB less than the ODN losses [84]. This cannot be accomplished in the back-to-back case due to lack of losses in the ODN.

3.2.4 Optical Power Budget

Using the PON architecture in Fig. 3-2 as a guideline, we can analytically outline the power budget of the O-SCM WDM PON. First, the input power to the ONU p-i-n photoreceiver is

$$P_{\text{ONU_Rx}} = P_{\text{OLT_Tx}} - L_{\text{ODN}} - L_{10\%}, \quad (3.1)$$

where L_{ODN} and $L_{10\%}$ are the insertion losses of the ODN and 10% coupler branch. On the other branch of the coupler, the input power to the RSOA is then

$$P_{\text{RSOA_in}} = P_{\text{OLT_Tx}} - L_{\text{ODN}} - L_{90\%}. \quad (3.2)$$

The ODN losses include the feeder losses L_{feeder} , AWG insertion losses L_{AWG} and the DDF losses L_{DDF} , where

$$L_{\text{ODN}} = L_{\text{feeder}} + L_{\text{AWG}} + L_{\text{DDF}}. \quad (3.3)$$

Similarly, we can define the power of the signal at the OLT receiver as

$$P_{\text{OLT_Rx}} = g_{\text{RSOA}}(P_{\text{RSOA_in}}) \cdot P_{\text{RSOA_in}} - L_{90\%} - L_{\text{ODN}} - L_{\text{circ}_{2-3}} - L_{\text{OBPF}} \quad (3.4)$$

where $g_{\text{RSOA}}(P_{\text{RSOA_in}})$ is the gain of the RSOA,² and $L_{90\%}$, $L_{\text{circ}_{2-3}}$ and L_{OBPF} are the insertion losses of the 90% coupler branch, circulator ports 2 to 3 and the OBPF respectively.

Looking at Eqs. (3.1) to (3.4), we can see that $P_{\text{ONU_Rx}}$ depends on the choice of launch power and ONU coupling ratio, whereas $P_{\text{OLT_Rx}}$ also depends on the RSOA gain. To better illustrate the need to balance the power budget, we show the symmetric BER performance as a function of $P_{\text{OLT_Tx}}$ in Fig. 3-5. Here we see that using the 90/10 coupler results in a 7 dB disparity in the launch power required for each of the channels to operate at $\text{BER} < 10^{-10}$.

In Fig. 3-6 we use the analytical power budget to estimate the best ONU coupling ratio. Recall from Fig. 3-4 that the minimum received powers to achieve $\text{BER} < 10^{-10}$ over the 20 km feeder are -16 dBm and -10 dBm for the downlink and uplink channels, respectively. Using Eqs. (3.1) to (3.4), we can then numerically estimate the OLT launch power necessary to achieve these received powers for different coupler combinations. The results are shown in Fig. 3-6(a). The power balance is achieved at the crossing point where approximately 65% of the optical power seeds the RSOA

² Recall from Fig. 1-6 that the RSOA's gain depends on the input optical power.

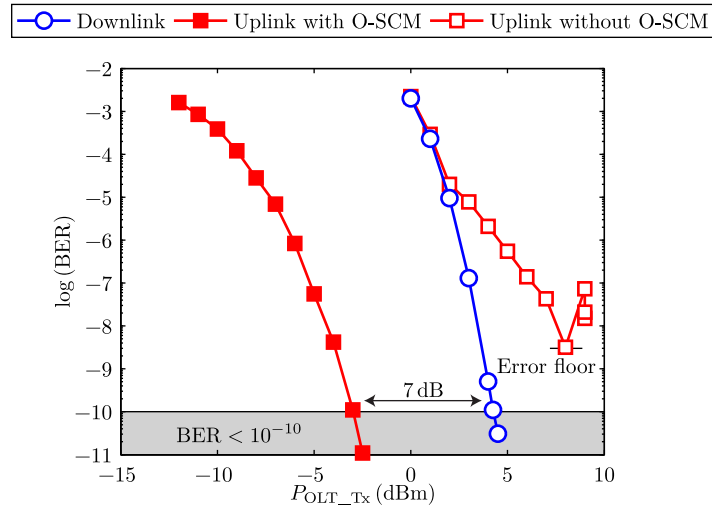


FIGURE 3–5: Bidirectional performance of the 1.5 Gbit/s O-SCM architecture over a 20 km WDM PON as a function of OLT launch power.

and $P_{OLT_Tx} > -2$ dBm will allow both channels to operate at BERs below 10^{-10} . Figure 3–6(b) shows the characterization of the RSOA which is used to estimate $g_{RSOA}(P_{RSOA_in})$ in the power budget.

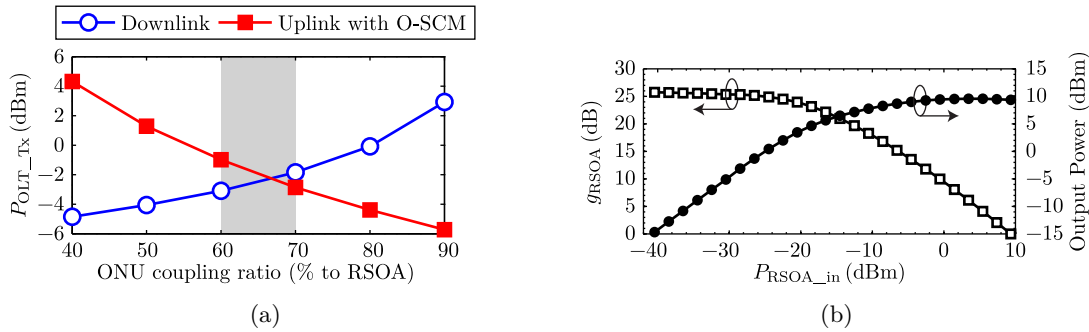


FIGURE 3–6: Power budget optimization of the ONU coupling ratio. (a) Launch power required to achieve BER $< 10^{-10}$. (b) Measured gain profile characteristics of the RSOA.

3.2.5 Operating Constraints for O-SCM

As discussed in Section 1.2.3, the RSOA’s primary drawback is its limited modulation bandwidth. In this experiment the two transmission channels overlap, leaving some residual noise to impact the upstream performance. Increasing the subcarrier frequency reduces the channels’ spectral overlap but extends the uplink channel towards the RSOA bandwidth boundary. In Fig. 3–7

we can qualify the trade-off between the crosstalk and RSOA bandwidth and optimize the uplink's performance by tuning f_{UL} and looking at its effect on the signal's Q factor.

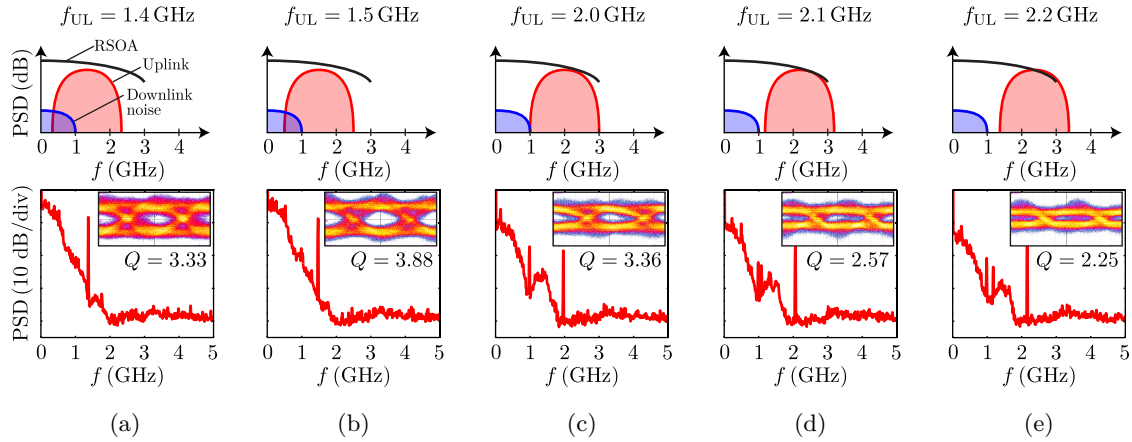


FIGURE 3-7: Illustrations of the 1 Gbit/s O-SCM channel allocation at different subcarrier frequencies (top) and the RF spectra measured after down-conversion (bottom). The spikes are due to the local oscillator leakage caused by the poor isolation of the RF mixers.

In order to fit both channels within the RSOA bandwidth, the symmetric data rate is reduced to 1 Gbit/s. The upper illustrations demonstrate the allocation of the transmission channels with respect to the RSOA bandwidth. The lower plots show the corresponding electrical spectra, eye diagrams and Q factors measured after photodetection, down-conversion and low pass filtering. Figures 3-7(a) and 3-7(b) demonstrate the cases with overlapped channels and maintain the uplink well within the RSOA bandwidth. Here the performance is limited by the inter-channel crosstalk and the 1 GHz to 4.2 GHz RF bandwidth of the mixers.

In Figs. 3-7(c) to 3-7(e) we see the more conventional SCM implementation. Here though, as f_{UL} increases, the uplink channel becomes bounded by the RSOA's modulation bandwidth and the eye opening begins to close. In this case a 1.5 GHz subcarrier results in the best Q factor and balances the design trade-offs, which will become much more important at higher bit rates.

3.3 Optimized O-SCM WDM PON Operating at 2.5 Gbit/s

In this section we continue to characterize the performance of the O-SCM WDM PON. Changes to both the RF hardware and optoelectronic transmitters enable symmetric data rates to increase to 2.5 Gbit/s. The most obvious change at the OLT is that a butterfly packaged electro-absorption

modulated laser (EML) replaces the expensive distributed feedback laser and Mach-Zehnder modulator transmitter. The EML's small packaging, commercial availability and cost effectiveness make it ideal as a downlink transmitter. Additionally, we experimentally investigate the impact of the ONU coupling ratio on balancing the system's optical power budget and characterize the system's BER performance at this optimum condition.

3.3.1 Changes to the Physical PON Architecture

Figure 3-8 outlines the PON architecture used throughout these experiments. A pulse-pattern generator drives the EML with a NRZ $2^{15} - 1$ PRBS at $1 V_{p-p}$ and biased at $-250 mV$ to set the downlink ER to 2.4 dB. Fixing the EML's integrated thermoelectric cooler at $22.5^\circ C$ stabilizes the output wavelength at 1549.36 nm, corresponding to the centre of the AWG's channel. An EDFA and VOA control the power launched into the ODN. An EDFA and VOA control the power launched into the ODN.

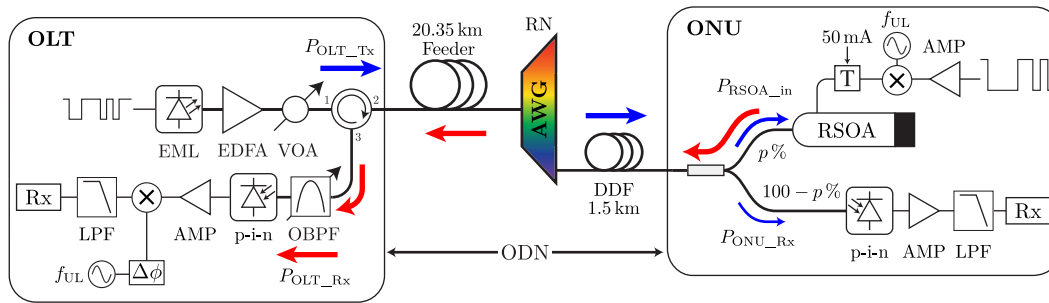


FIGURE 3-8: Physical architecture of the 2.5 Gbit/s O-SCM WDM PON. $\Delta\phi$: electrical phase delay, AMP: RF amplifier, AWG: arrayed waveguide grating (100 GHz channel spacing), EML: CyOptics E4560 (11 GHz bandwidth), OBPF: JDS Fitel TB9 (50 GHz bandwidth), p-i-n: HP 11982A (12 GHz bandwidth), RSOA: CIP SOA-RL-OEC-1550, T: RF bias-tee.

At the ONU, the 90/10 coupler from the previous experiments is replaced by a series of couplers in 10% increments in order to optimize the operating power budget of the PON. For the upstream transmission, a NRZ $2^{23} - 1$ PRBS is up-converted onto a subcarrier that matches the first-null bandwidth of the baseband NRZ signal. For example, $f_{UL} = 1.5 GHz$ when the data rate is 1.5 Gbit/s. Similar to the previous architecture, the bias-tee and RF amplifier set the signal swing to $4 V_{p-p}$ and the RSOA bias current at 50 mA for direct modulation. At the OLT receiver, the 50 GHz OBPF is centred on the carrier wavelength to remove out-of-band amplified spontaneous emission noise. The p-i-n photodiode detects the uplink signal, which is then amplified, down-converted to baseband and low pass filtered.

3.3.2 BER Performance for 2.5 Gbit/s Symmetric Operation

To verify the operation of the EML as the OLT transmitter, we first reproduce the 1.5 Gbit/s experiments from Section 3.2 over a 20 km PON using the same RF hardware and operating conditions for the optical components. Note that the suboptimal 90/10 ONU coupler is used for comparison purposes. To operate at 2.5 Gbit/s we increase the subcarrier frequency and driving clock to 2.5 GHz and replace the mixers³ and LPFs⁴ to accommodate the increased bandwidth. Figure 3–9 compares the BER performance of the O-SCM WDM PON operating at 1.5 Gbit/s and 2.5 Gbit/s using the new EML transmitter.

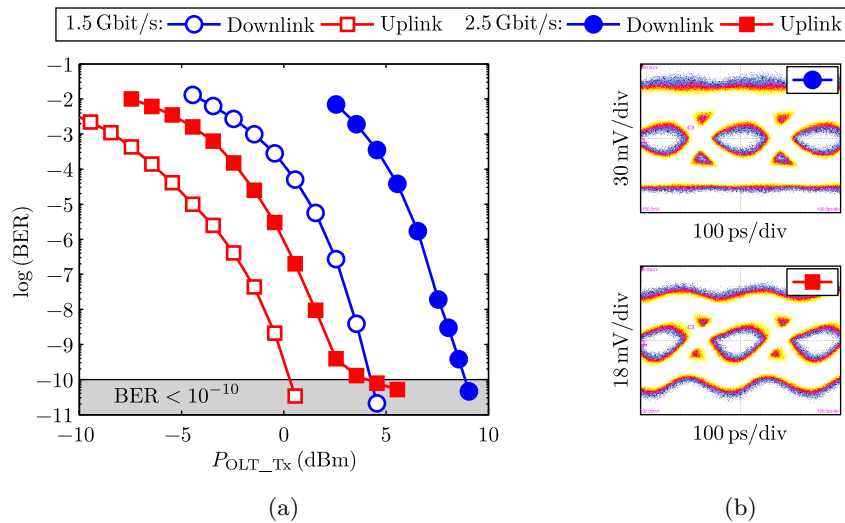


FIGURE 3–9: Bidirectional performance of the O-SCM WDM PON over a 20 km feeder at 1.5 Gbit/s and 2.5 Gbit/s. (a) Downlink and uplink BER as a function of launch power. (b) Example eye diagrams at $\text{BER} \sim 10^{-10}$.

First, we can look at the BER performance in terms of P_{OLT_Tx} in Fig. 3–9(a). Raising the bit rate to 2.5 Gbit/s requires increasing the launch power by 4 dB and 5 dB for the uplink and downlink, respectively, in order to achieve a BER below 10^{-10} . The uplink channel, which spans a first-null bandwidth from 0 GHz to 5 GHz, is impacted by the 2 GHz RSOA modulation bandwidth. The uplink channel’s BER approaches a floor at launch powers beyond 5 dBm, indicating that the RSOA is deeply saturated, such that the uplink signal becomes power limited. The penalty on the

³ Marki Microwave M10208MP

⁴ Picosecond 4th order Bessel-Thomson (1.875 GHz bandwidth)

downlink channel is primarily due to the increased dispersion as a result of the higher bit rates. The eye diagrams in Fig. 3–9(b) demonstrate clear openings for $\text{BER} < 10^{-10}$, although the uplink signal retains some residual intensity noise due to the local oscillator clock leakage discussed earlier.

3.3.3 Optimizing the ONU Coupler

As noted previously, using a 90/10 coupler at the ONU results in an unbalanced power budget where one channel requires a significantly higher OLT launch power than the other to operate at $\text{BER} < 10^{-10}$. The power budget developed in Section 3.2.4 estimates that a 65/35 coupling ratio at the ONU will balance the $P_{\text{OLT_Tx}}$ required to achieve symmetric transmission. In order to verify this experimentally, we repeated the BER measurements at 2.5 Gbit/s as a function of launch power for a series of coupling ratios. The results are summarized in Fig. 3–10.

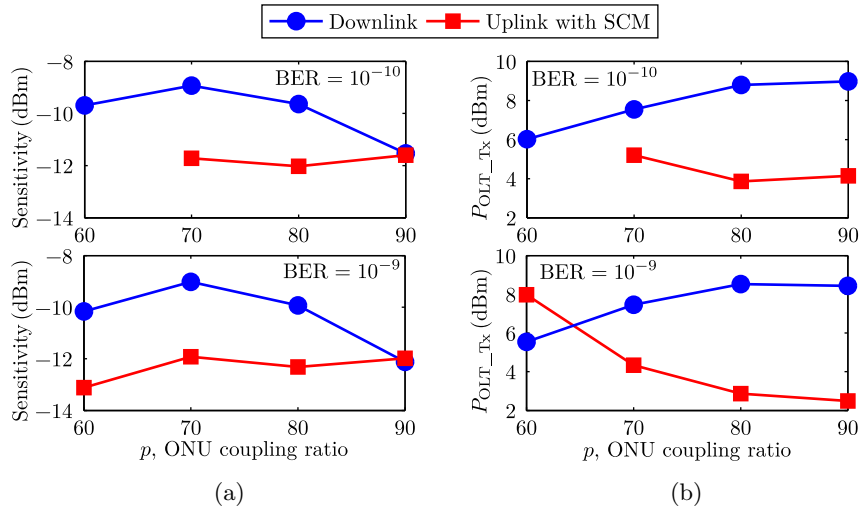


FIGURE 3–10: Optimization of the ONU coupling ratio with (a) sensitivity and (b) launch power for BER thresholds of 10^{-10} (top) and 10^{-9} (bottom).

Looking at the receiver sensitivities and launch power requirements in Fig. 3–10, we can notice some general trends. On the left hand side, the 60/40 coupler favours the downlink channel performance where a large portion of the downstream signal is sent to the p-i-n for detection. Here, we see that the uplink cannot achieve a $\text{BER} < 10^{-10}$ due to an error floor encountered near 10^{-9} corresponding to the onset of SBS at $P_{\text{OLT_Tx}} > 7$ dBm. On the right hand side of the curves, the coupling ratio provides more input power to the RSOA. Less launch power is therefore needed to achieve the required BER for the uplink, but much more power is needed for the downlink. This is the case of the 90/10 coupler in Fig. 3–9. The crossing point at 65 % corresponds to the coupling

ratio that balances the power budgets and minimizes the $P_{\text{OLT_Tx}}$ needed for symmetric operation. This agrees well with the previous power budget estimate in Section 3.2.4. In Fig. 3–11 we present the system performance with a 70/30 coupler, which is the closest available coupler to the optimum.

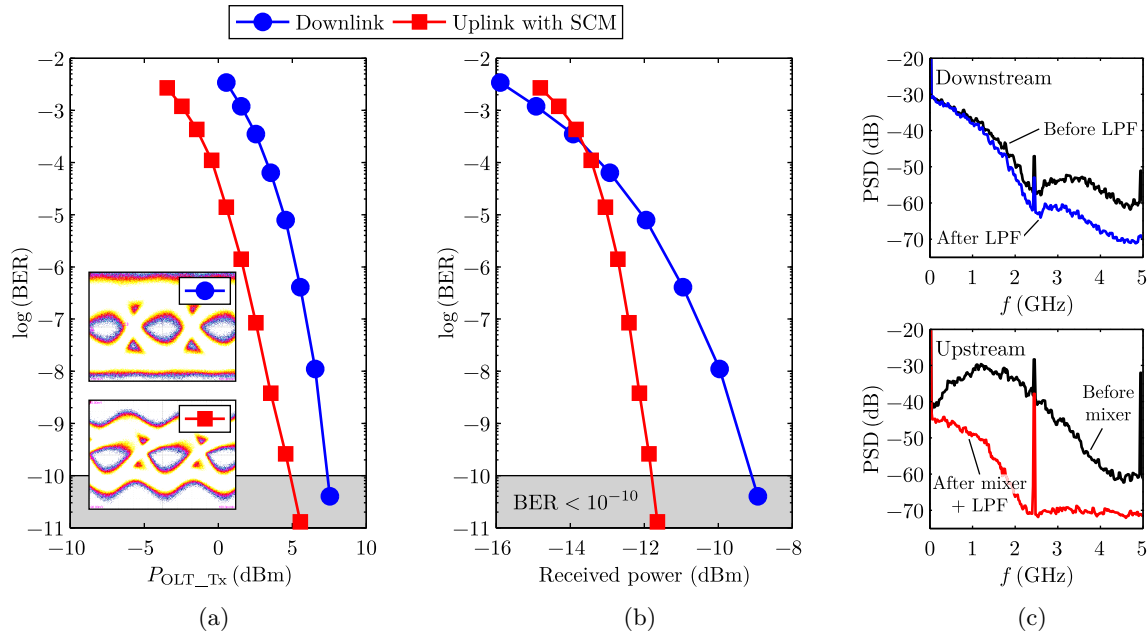


FIGURE 3–11: Performance of the 2.5 Gbit/s O-SCM WDM PON with full-duplex transmission over a 20 km feeder using the 70/30 ONU coupling ratio. Channel BER as a function of (a) OLT launch power and (b) received optical power. Eye diagrams for both channels are inset for $\text{BER} \sim 10^{-10}$. (c) Electrical power spectra of the received downstream (top) and upstream (bottom) signals as measured after photodetection.

In Figs. 3–11(a) and 3–11(b) we see that symmetric operation with BERs below 10^{-10} is achievable for both channels without the need for FEC, DSP or dispersion compensation. The required minimum launch power is 7 dBm which is within the specifications for next-generation TDM PONs [25, 26]. In terms of received power, the performance of the uplink becomes better than that of the downlink channel. This is a design trade-off of using the coupling ratio to optimize $P_{\text{OLT_Tx}}$, while fixing the other transmission parameters. Although not verified, finely tuning the downlink ER or RSOA gain may help to improve this sensitivity imbalance.

The electrical frequency spectra in Fig. 3–11(c) help to illustrate the operating principle of the O-SCM WDM PON. Looking first at the downstream, we see that the LPF suppresses some of the high frequency (> 2 GHz) RB noise that originates from the uplink channel. In the upstream spectrum, the up-converted uplink channel (measured before the mixer) extends beyond 4 GHz. In

principal, the peak power of the uplink channel should be centred around the 2.5 GHz subcarrier frequency, but here the RSOA's limited modulation bandwidth attenuates the higher frequencies. This effectively limits the uplink data rate to 2.5 Gbit/s without the aid of electronic equalization. After detection, amplification and filtering, the baseband signal extends from baseband to 2.5 GHz, as expected. Here we also note the presence of a strong tone at f_{UL} from the clock used for down-conversion. This is due to a power mismatch between the input received signal and the clock signal, causing clock leakage into the down-converted signal. The impact of this tone is a periodic intensity noise, as demonstrated in the uplink eye diagram. Fine tuning the specifications of the mixer pair could help alleviate this leakage.

3.4 A 2.5 Gbit/s O-SCM WDM PON With a Burst-Mode OLT Receiver

In PON systems, one of the implementation difficulties that arises is achieving clock synchronization for accurate data sampling. This primarily affects the OLT receiver due to the inherent bursty nature of upstream transmissions, which can have variations in both amplitude and phase due to varying optical path lengths [15]. In deployed systems, a BM clock and data recovery circuit must be used to achieve a fast lock in order to minimize the amount of data lost during synchronization. In PONs using SCM, it is also important to maintain the correct phase of the subcarrier clock signal, f_{UL} , that down-converts the SCM channel back to baseband. In this section, we characterize the performance of a 2.5 Gbit/s SCM WDM PON using a BM receiver at the OLT [8]. The receiver is tested by applying phase steps within the uplink data without introducing silence periods. This scenario effectively simulates phase instabilities that may be caused by inexpensive ONU components.

3.4.1 Physical PON Architecture

Figure 3–12 illustrates the architecture of the 20 km SCM WDM PON used in this experiment. The operating parameters are those of the optimized 70/30 case described above in Section 3.3.3. At the OLT receiver, we note that the mixer and 2.5 GHz local oscillator are replaced with a BM receiver that performs clock and data recovery, instantaneous phase acquisition and RF down-conversion of the SCM uplink channel.

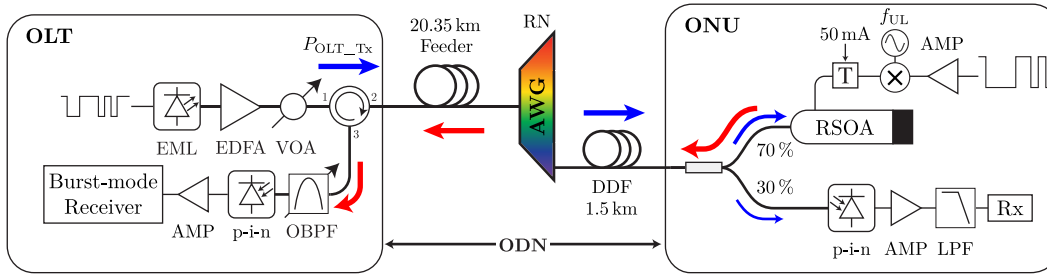


FIGURE 3–12: Physical architecture of the 2.5 Gbit/s O-SCM WDM PON with BM clock and data recovery uplink receiver at the OLT. AMP: RF amplifier, AWG: arrayed waveguide grating (100 GHz channel spacing), EML: CyOptics E4560 (11 GHz bandwidth), OBPF: JDS Fitel TB9 (50 GHz bandwidth), p-i-n: HP 11982A (12 GHz bandwidth), RSOA: CIP SOA-RL-OEC-1550, T: RF bias-tee.

3.4.2 Burst-Mode Receiver Design for SCM Applications

The architecture of the proof-of-concept SCM BM receiver, based on semi-blind space domain oversampling, is shown in Fig. 3–13. The 2.5 Gbit/s upstream signal on a $f_{UL} = 2.5$ GHz subcarrier enters the receiver where it is split into three paths. A clock recovery unit⁵ extracts a 5 GHz reference clock CK_0 from the up-converted input signal, which is then passed to a set of phase shifters that generate multiple clocks with low skew. These two new clock signals, $CK_{-\frac{\pi}{2}}$ and $CK_{+\frac{\pi}{2}}$, have phase offsets from CK_0 by $-\frac{\pi}{2}$ rad and $+\frac{\pi}{2}$ rad, respectively. These phase shifted clocks are then passed to a phase picker circuit.

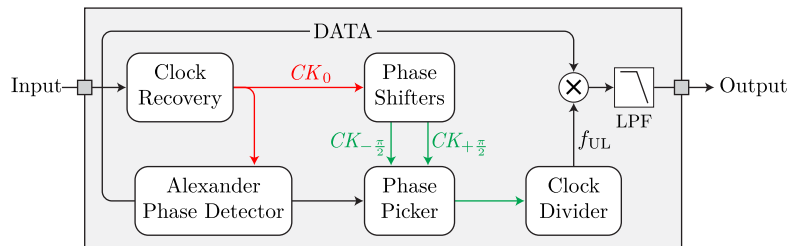


FIGURE 3–13: Block diagram of the proof-of-concept BM receiver for SCM applications using a bang-bang Alexander phase detector.

At the same time, a bang-bang Alexander phase detector [109] compares the input data signal to the reference clock CK_0 to determine whether it is leading or lagging. At the next stage, the phase picker circuit uses the phase detector's output as a control signal to select between $CK_{+\frac{\pi}{2}}$

⁵ Centellax TR1C1-A

and $CK_{-\frac{\pi}{2}}$ as the clock signal that is most in phase with the data signal. The selected clock, at 5 GHz, is at twice the desired subcarrier frequency. A clock divider then reduces the recovered clock frequency by one half, resulting in a phase matched f_{UL} which drives the down-conversion of the SCM uplink signal back to baseband. A LPF⁶ then removes out-of-band noise and suppresses the clock leakage.

Figure 3–14 shows example electrical eye diagrams of the received uplink signal for different phase shifts, as measured at the input of the BM receiver. The frequency divided 2.5 GHz clocks CK_0 (red) and $CK_{\pm\frac{\pi}{2}}$ (green) are also overlaid to demonstrate the operation of the BM clock and data recovery. In each case, the bold dashed line indicates the optimum sampling instant to align with the middle of the data signal’s eye opening. In Fig. 3–14(a) where no phase offset exists, CK_0 is the only valid clock signal. For the cases in Figs. 3–14(b) and 3–14(c), where the clocks are offset by $-\frac{\pi}{2}$ and $+\frac{\pi}{2}$ respectively, the receiver has the ability to select the best clock between $CK_{+\frac{\pi}{2}}$ and $CK_{-\frac{\pi}{2}}$ to perform down-conversion.

This proof-of-concept receiver uses a two-state phase detector, and as a result, the output can only select between the two phase offset clocks $CK_{+\frac{\pi}{2}}$ and $CK_{-\frac{\pi}{2}}$. In order to give this receiver the ability to instantaneously track phase variations over a full 0 rad to $\pm\pi$ rad range, we propose replacing the Alexander phase detector with a linear Hogge phase detector [110]. In this case, the output of the linear phase detector would simply control a phase shifter that adjusts the phase of CK_0 before being passed to the clock divider and mixer for signal down-conversion.

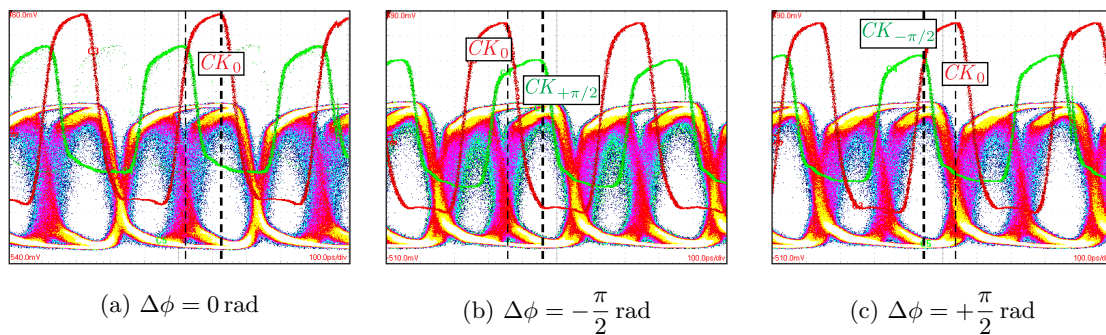


FIGURE 3–14: Electrical eye diagrams of the received uplink signal. The overlaid clock signals are shown for different phase shifts $\Delta\phi$. The bold dashed line indicates the optimum sampling instant to align with the middle of the data signal’s eye opening.

⁶ Picosecond 4th order Bessel-Thomson (1.875 GHz bandwidth)

3.4.3 Experimental Results

The performance of the uplink channel with the OLT BM receiver is shown in Fig. 3–15. In Fig. 3–15(a) we measure the Q factor of the baseband uplink signal as a function of $P_{\text{OLT_Tx}}$ for different phase offsets. As expected the Q factor increases with launch power, similar to the case in Fig. 3–11 where the BER performance improves with $P_{\text{OLT_Tx}}$. To provide an operating threshold, we measured a 14.25 dB Q factor that corresponds to a $\text{BER} = 10^{-10}$ at $P_{\text{OLT_Tx}} = 6.6$ dBm.

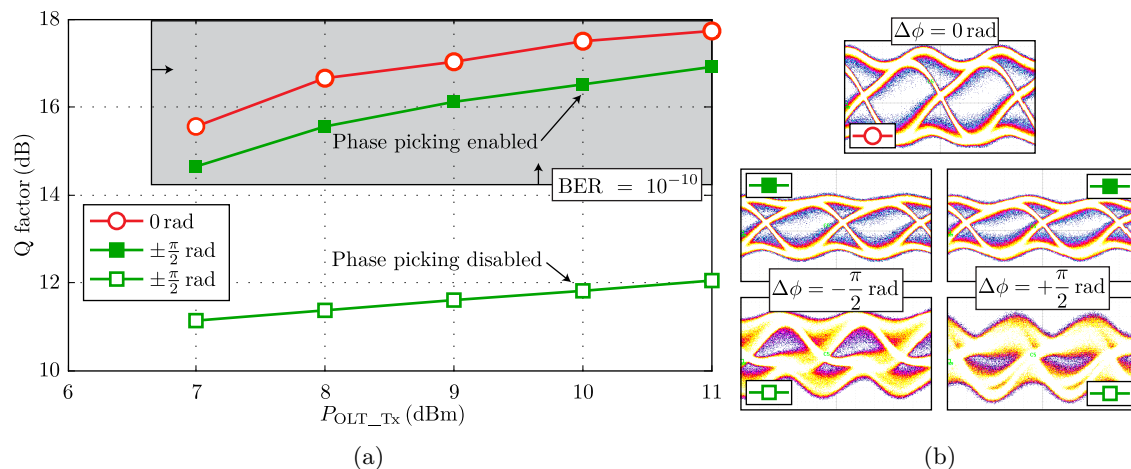


FIGURE 3–15: Performance of the 2.5 Gbit/s SCM WDM PON with a stand-alone BM receiver. (a) Q factor of the uplink channel as a function of OLT launch power for various phase shifts between the uplink data and the recovered clock. (b) Corresponding electrical eye diagrams of the uplink SCM signal after down-conversion to baseband.

In the first case, the best performance is achieved by manually tuning CK_0 to the optimized state where no phase shift is introduced ($\Delta\phi = 0$). This provides the upper bound on the performance of the SCM WDM PON. When a phase offset of either $-\frac{\pi}{2}$ rad or $+\frac{\pi}{2}$ rad is introduced to the uplink, the operation of the BM receiver is tested. The uplink can still achieve a Q factor above the operating threshold when the instantaneous phase picker selects the correct clock, either $CK_{+\frac{\pi}{2}}$ or $CK_{-\frac{\pi}{2}}$. When the phase picker is disabled and the incorrect clock is selected for down-conversion, the performance of the uplink signal degrades by more than 4 dB. Figure 3–15(b) shows eye diagrams of the down-converted signals as measured after the BM receiver.

3.5 Summary

In this chapter we introduced the concept of O-SCM for WDM PONs, which increases the bandwidth efficiency and symmetric data rates compared to conventional SCM approaches. We

experimentally investigated the system's symmetric operation at 1.5 Gbit/s in optical back-to-back and bidirectional 20 km single feeder PON configurations and presented an analytical model of the system's optical power budget to optimize the coupling ratio at the ONU. We then characterized the O-SCM architecture at 2.5 Gbit/s using a more realistic EML downlink transmitter and experimentally validated the effect of the ONU coupling ratio on the power budget. The BER performance of the system with the optimum 70/30 ONU coupler is then presented. Furthermore, we demonstrated a proof-of-concept O-SCM WDM PON with a stand-alone BM receiver at the OLT that performs clock and data recovery, instantaneous phase acquisition and RF down-conversion of the 2.5 Gbit/s uplink channel.

CHAPTER 4

Electronically Equalized 5 Gbit/s Overlapped-SCM WDM PON

THE CONCEPT of O-SCM was introduced in Chapter 3 as a viable technology for next-generation WDM PONs, but symmetric transmission rates were limited to 2.5 Gbit/s due to the RSOA's modulation bandwidth. In this chapter we describe the design and characterize the performance of a second generation O-SCM WDM PON architecture operating at 5 Gbit/s [2]. Two key improvements help to alleviate the bandwidth effects of the RSOA: 1) The downlink channel is placed on a RF subcarrier and the uplink is transmitted at baseband. This simplifies the ONU transmitter design and maintains a 5 GHz first-null bandwidth for the uplink channel. 2) The introduction of an offline DSP analysis framework at the OLT receiver to facilitate electronic equalization of the uplink signal. Together these improvements allow the symmetric data rates to be increased to 5 Gbit/s over a 20 km single feeder PON.

This chapter is organized as follows: Section 4.1 outlines the development of the offline analysis framework; including the data frame structure, data capture, and electronic equalization to remove the ISI from the bandwidth-limited uplink transmission. In Section 4.2 we introduce the improved O-SCM WDM PON physical architecture. Section 4.3 presents an experimental investigation of the system's full-duplex BER performance. Finally, we summarize and conclude the chapter in Section 4.4.

4.1 Offline Analysis and DSP Equalization Framework

As outlined in Section 1.2.3, the primary limitation of the uplink transmission bitrate is the 2 GHz modulation bandwidth of the RSOA. Electronic equalization has been shown to reduce the effects of ISI allowing bit rates beyond 2.5 Gbit/s for the uplink channel [49, 53–55]. To perform these equalization techniques, we capture the received data using a real-time oscilloscope and then subsequently process it offline. This software framework leverages network-based data capturing

and multi-core processing to enable measurements to be performed quickly, enabling system optimization and rapid prototyping that would be unfeasible with a hardware equalizer.

The analysis software comprises four main components: 1) the creation of frame based data patterns, 2) network-based data capturing with a real-time oscilloscope; 3) data alignment, sampling and decision optimization; and 4) electronic equalization.

4.1.1 Data Frame and Structure

In order to perform accurate BER measurements, traditional BER testers compare the received signal to industry standard PRBS patterns. For offline processing, a similar approach is taken where a known bit pattern is transmitted and used at the receiver to calculate the BER. However, it is impractical to use such extremely long bit sequences (such as a $2^{23} - 1$ PRBS) due to the memory limitations of the real-time oscilloscope. To overcome this we have devised a frame based data pattern, illustrated in Fig. 4–1, which is transmitted by the pulse-pattern generators.

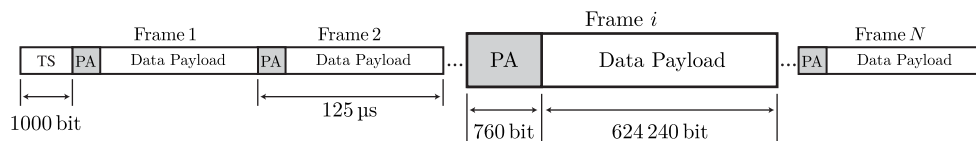


FIGURE 4–1: Structure of the transmitted data frames. PA: preamble, TS: training sequence.

At onset, a standard PRBS pattern (downlink: $2^{15} - 1$, uplink: $2^{23} - 1$) is generated and encoded with a Reed-Solomon (RS) FEC code, which is widely used in communication systems and is especially useful in channels that are susceptible to burst errors [50]. RS is a block coding technique where the data is grouped into m bit symbols, with an encoded block length of $n = 2^m - 1$ symbols, and can correct at least t symbol errors. The choice of block size and parity is normally denoted $RS(n,k)$, where $k = n - 2t$ symbols is the block size of the data payload. Table 4–1 summarizes the two most popular codes for PONs which are compatible with current GPON [23] and 10G-EPON [25] standards.

The FEC encoded PRBS data is then segmented into 624 240 bit frames. A unique 760 bit preamble is appended to the beginning of each frame to provide a signature for processing at the receiver, adding a negligible $\sim 0.1\%$ to the total overhead. The preamble length is selected to ensure a total frame size of 625 000 bit, which at 5 Gbit/s is compatible with the 125 μs upstream frame duration in existing GPON standards [23]. A 1000 bit training sequence is placed at the front

TABLE 4–1: Comparison of the RS FEC codes used in current PON standards.

Parameter	RS(255,239)	RS(255,223)
Encoded block size, n (Symbol)	255	255
Symbol size, m (bit)	8	8
Parity symbols, $2t$	16	32
Payload symbols, k	239	223
Correctable symbol errors	8	16
Coding overhead	6.3%	12.5%
Encoded BER threshold	1.8×10^{-4}	1.1×10^{-3}

of the data sequence and initializes the equalizer taps at the OLT receiver on system start-up. It is therefore not considered to be part of the operating overhead. The final data frame patterns are loaded onto a pulse-pattern generator mainframe that drives the uplink and downlink transmitters for the transmission experiments.

This frame-based technique provides three main advantages: 1) each frame is uniquely identifiable and extractable from the received data sequence to facilitate training symbols during equalization and BER calculations; 2) each frame’s start can be resynchronized to account for sampling drift, analogous to clock-synchronization in deployed GPON systems; and 3) frame alignment and equalization can be efficiently computed in parallel using a multi-core processor.

4.1.2 Network-Based Data Acquisition

One of the key challenges of offline analysis for high-speed communication systems is the sheer overhead of capturing and processing the transmission data. In order to streamline this process, we developed a MATLAB script that uses the standard commands for programmable instruments interface to communicate with the real-time oscilloscope over the lab’s Ethernet network. Large records of more than 10 MSa are often needed for each captured sequence in order to accurately measure the BER down to sufficient levels. If saved as a plain text file, the captured data sequence would exceed 1 GB. Instead, the script transfers the int16 precision data points over the network in 2^{18} bit blocks and saves them to a time-stamped binary data file occupying just 80 MB. These data files can then be processed immediately or kept for later analysis.

As noted above, it is important to ensure that we capture enough bits to make a BER measurement that is accurate to a certain precision. Because experimental BER measurements are a statistical process, we can define an acceptable confidence level (CL) that the system’s true BER is

less than the specified BER [111]. To measure a specific BER threshold for offline processing, the minimum number of captured bits is given by

$$N_{\text{bit}} \geq \frac{-\ln(1 - \text{CL})}{\text{BER}}, \quad (4.1)$$

where typically $\text{CL} = 95\%$. Similarly when sampling a binary waveform with a real-time oscilloscope, the number of captured bits is

$$N_{\text{bit}} = \frac{R_b}{R_s} \times M_{\text{scope}}, \quad (4.2)$$

where R_b is the data bit rate, and R_s and M_{scope} are the oscilloscope's sampling rate and memory depth, respectively. Rearranging Eq. (4.1) and substituting in Eq. (4.2) results in

$$M_{\text{scope}} \geq \frac{R_s}{R_b} \frac{-\ln(1 - \text{CL})}{\text{BER}}, \quad (4.3)$$

which defines the minimum record size required to calculate a BER for a given CL. Equation (4.3) proves very useful to reduce the captured file size and to optimize the offline processing and BER calculation time. We note however that an additional margin must be made to account for the overhead due to the training sequence and preamble bits.

4.1.3 Data Frame Alignment and BER Calculation

In order to analyze and characterize the received data frames, they must first be identified and extracted from the recorded bit pattern; Figure 4–2 helps to illustrate this process. Each transmitted frame is up-sampled to match the sampling rate of the received data and then the preambles are cross-correlated with the received signal to identify the index i of each frame in the sequence. Knowing the fixed frame size, the complete frames are extracted from the sequence and assembled into a matrix for post-processing and BER calculations. We note that the captured sequence is bookended with truncated frames due to the repeated output from the pulse-pattern generators. These incomplete frames are discarded and not used in the offline analysis.

Once the matrix of received frames is assembled, they are downsampled to $2\text{Sa}/\text{bit}$ and the unequalized BER is calculated by optimizing the sampling point and decision amplitude to minimize the BER. This process is analogous to optimizing the timing delay and decision threshold voltage of a hardware BER tester. After this step, the uplink channel undergoes post-compensation with

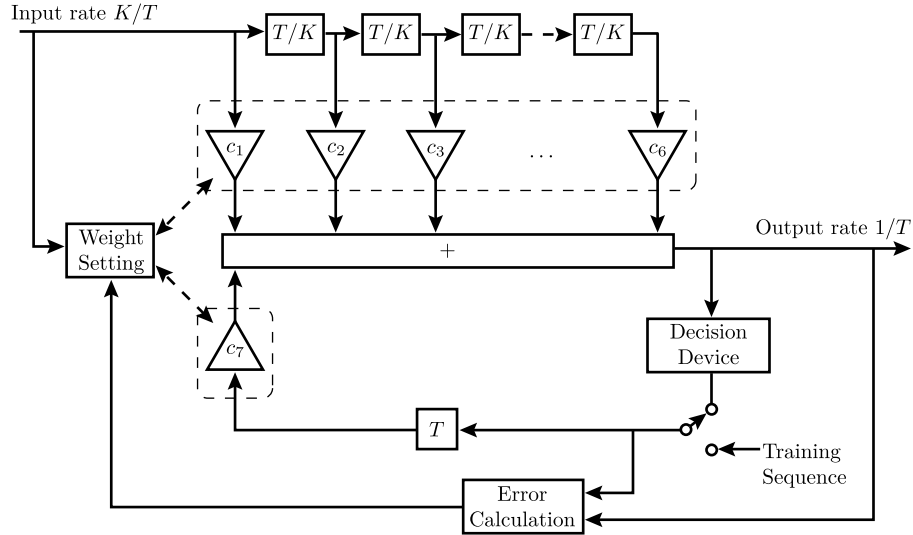


FIGURE 4-3: Block structure of a fractionally spaced DFE, where $K = 2$ is the number of input samples per symbol and $1/T$ is the output sample rate.

TABLE 4-2: Summary of the electronic equalizer parameters.

Parameter	Value
Training sequence length	1000 bit
Minimum LMS step size	0.02
Feedforward taps	6
Feedback taps	1
Forward tap spacing	1/2-symbol
Feedback tap spacing	1-symbol

4.2 Physical PON Architecture

The bidirectional architecture of the second generation O-SCM WDM PON is illustrated in Fig. 4-4. The OLT transmitter consists of an EML centred at 1549.36 nm. The EML is driven at $1 \text{ V}_{\text{p-p}}$ by a 5 Gbit/s NRZ $2^{15} - 1$ PRBS-based data sequence up-converted on a 5 GHz subcarrier. Following the EML, an EDFA and a VOA control the OLT launch power $P_{\text{OLT_Tx}}$. In a realistic deployment this EDFA would be used to simultaneously amplify many user wavelengths, sharing the investment costs among the customer base. The ODN comprises a 20.35 km feeder of standard single mode fiber (SMF-28e+), a 100 GHz AWG and a 1.5 km DDF.

At the ONU, a coupler taps off 40% of the downstream signal to the receiver composed of a commercial p-i-n photoreceiver and RF down-conversion circuit. A real-time oscilloscope performs

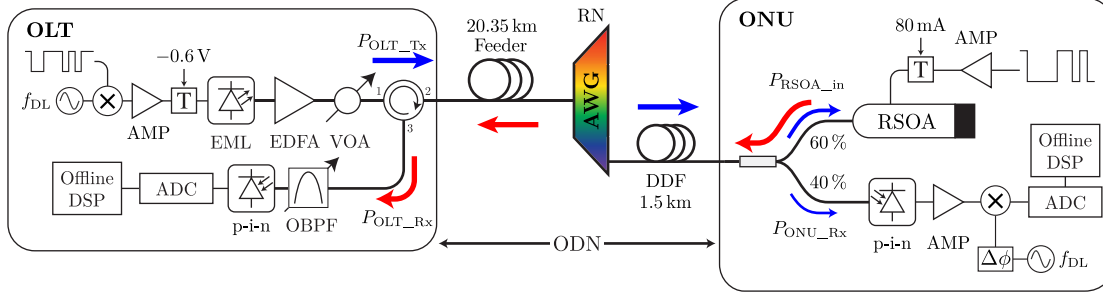


FIGURE 4–4: Physical architecture of the 5 Gbit/s O-SCM WDM PON. $\Delta\phi$: electrical phase delay, ADC: Agilent Infiniium DSCZ93204A, AMP: RF amplifier, AWG: arrayed waveguide grating (100 GHz channel spacing), EML: CyOptics E4560 (11 GHz bandwidth), Mixers: Marki Microwave M1-0412MP, OBPF: JDSU VCF050 (0.3 nm bandwidth), p-i-n: Discovery Semiconductors DSC-R402 (10 GHz bandwidth), RSOA: CIP SOA-RL-OEC-1550, T: RF bias-tee.

high-speed analog-to-digital conversion (ADC) and captures the received downlink signal for offline processing. The remaining 60% seeds the RSOA with enough input power to operate in gain saturation. The uplink transmitter uses a butterfly packaged RSOA directly modulated with a $2^{23} - 1$ PRBS-based bit sequence at $4V_{p-p}$ and biased at 80 mA, with peak gain from 1530 nm to 1570 nm. This results in an optical output with a large uplink ER ~ 9.5 dB to ensure sufficient downlink data erasure and therefore data remodulation. The unamplified OLT receiver comprises an OBPF, commercial p-i-n photoreceiver and an ADC to capture the baseband uplink signal.

It is important to note some key differences when comparing Fig. 4–4 to the previous architecture in Fig. 3–8. First, the downstream transmission is no longer transmitted at baseband and instead is placed on a 5 GHz subcarrier. As illustrated in Fig. 4–5, this downlink SCM channel extends in the frequency domain from 0 GHz to 10 GHz, which is within the specified bandwidth of the EML and the p-i-n photodetector. In the upstream direction, the baseband 5 Gbit/s uplink channel occupies the same 0 GHz to 5 GHz electrical channel bandwidth as in Chapter 3 but it operates at twice the bit rate.

Secondly, we note that the coupling ratio and RSOA bias current at the ONU have changed. Similar to Chapter 3, the coupling ratio is re-optimized and the 60/40 ratio was found to best balance the power budget of both channels. Here, we attribute the need to favour the downlink channel with more power to overcome the effects of dispersion from the 10 GHz null-to-null electrical bandwidth and the added noise from the SCM transmitter and receiver electronics. Increasing the RSOAs operating current to 80 mA improves the modulation bandwidth to ~ 2.2 GHz along

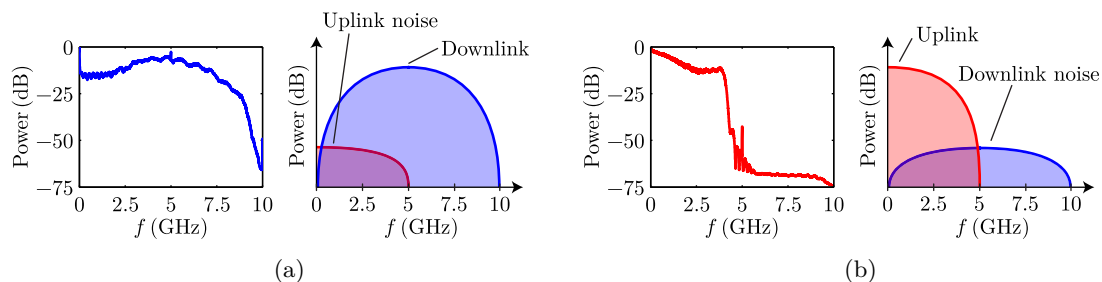


FIGURE 4–5: RF channel allocation in the 5 Gbit/s O-SCM WDM PON. Measurements and illustrations of the received (a) up-converted downlink and (b) baseband uplink signal spectra are shown. The real-time oscilloscope analog bandwidth was limited to 9 GHz and 4 GHz when capturing the downlink and uplink signals, respectively.

with additional gain and power to the upstream signal (see Fig. 1–7). Lastly, instead of using a commercial BER tester, the BER performance of each channel is calculated offline using a custom analysis software framework that facilitates DSP post-compensation equalization and FEC decoding of the captured signals. The details of this software package were outlined in Section 4.1.

4.3 Experimental Results at 5 Gbit/s

The following section presents the experimental characterization of the 5 Gbit/s O-SCM WDM PON. We begin by presenting an optical back-to-back characterization to demonstrate the efficacy of the analysis framework described in Section 4.1. We then proceed to a full-duplex demonstration over a 20 km PON test bed using fully optimized operating parameters. In lieu of using analog electrical filters, the real-time oscilloscope’s acquisition bandwidth is set to act as a sharp LPF to reduce the out-of-band noise and clock leakage from the RF mixers.

The real-time oscilloscope captures the data signals at a sampling rate of $R_s = 20$ GSa/s (4 Sa/bit at 5 Gbit/s) to a memory depth of 20.5 MSa. Using Eq. (4.3), we can confirm that a capture length of 20.5 MSa is sufficient to accurately estimate a BER down to 10^{-6} with a 95% CL:

$$\begin{aligned}
 M_{\text{scope}} = 20.5 \text{ MSa} &\geq \frac{20 \text{ GSa/s} - \ln(1 - 0.95)}{5 \text{ Gbit/s}} \frac{1}{10^{-6}} \\
 &\geq 12 \text{ MSa}.
 \end{aligned}$$

The 4 Sa/bit data is downsampled to 2 Sa/bit using a polyphase filter method with an additional 10 point finite-impulse response (FIR) filter to reduce aliasing effects, and then subsequently analyzed using the framework detailed in Section 4.1.

4.3.1 Optical Back-to-Back Performance

To begin characterizing the 5 Gbit/s architecture, we first remove the feeder and DDF to create the basic optical back-to-back configuration illustrated in Fig. 4-6. Similar to Chapter 3, this eliminates the RB contribution to the upstream noise and provides a means to verify the analysis framework’s operation.

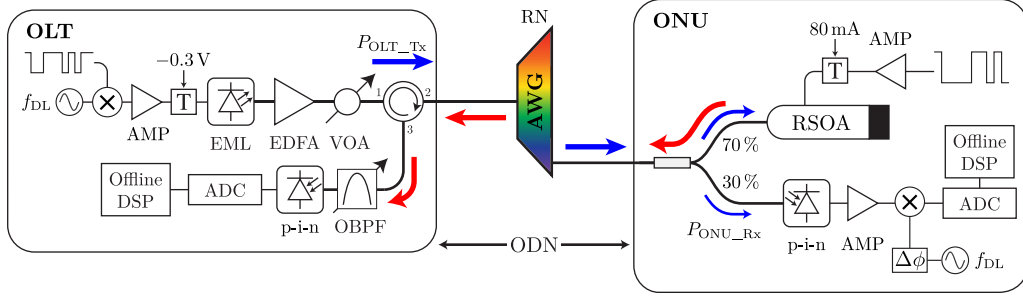


FIGURE 4-6: Physical architecture of the 5 Gbit/s O-SCM optical back-to-back test bed. $\Delta\phi$: electrical phase delay, ADC: Agilent Infiniium DSCZ93204A, AMP: RF amplifier, AWG: arrayed waveguide grating (100 GHz channel spacing), EML: CyOptics E4560 (11 GHz bandwidth), Mixers: Marki Microwave M1-0412MP, OBPF: JDSU VCF050 (0.3 nm bandwidth), p-i-n: Discovery Semiconductors DSC-R402 (10 GHz bandwidth), RSOA: CIP SOA-RL-OEC-1550, T: RF bias-tee.

In this preliminary experiment, a suboptimal 70/30 coupler divides the downstream signal at the ONU. This initial choice was based on the coupler used in Chapter 3. Similarly, the bias voltage of the EML is not fully optimized for the back-to-back test. Figure 4-7 summarizes the system’s BER performance for symmetric transmission. Assuming that the data is FEC encoded, the key performance markers are where the BER drops below the thresholds for the RS(255,239) and RS(255,223) codes listed in Table 4-1. These values correspond to the undecoded BERs that result in $\text{BER} < 10^{-12}$ after error correction [25], and therefore any BER measurements below these thresholds are assumed to be within the system’s operating range.

Looking first at the downlink signal in Fig. 4-7(a), we see that the BER begins to taper off after $P_{\text{OLT_Tx}} = 0$ dBm and reaches a floor above the calculation threshold of 10^{-6} . BERs below the FEC thresholds are achieved for launch powers of -1 dBm and 1 dBm corresponding to receiver sensitivities of -11 dBm and -9 dBm for RS(255,239) and RS(255,223), respectively. For the uplink channel in Fig. 4-7(b), performance without equalization is similar to that of the downlink channel. However, with the aid of a post-compensation equalizer, the BERs quickly fall below the calculation threshold for $P_{\text{OLT_Tx}} > -1$ dBm. The electronic equalizer reduces the OLT launch power required

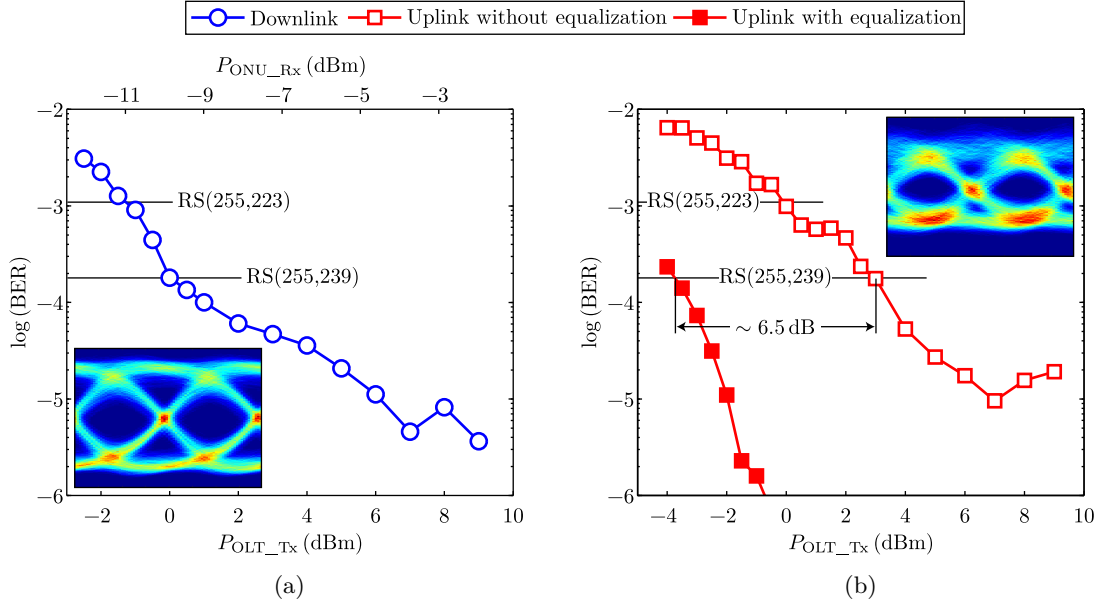


FIGURE 4–7: Optical back-to-back performance of the 5 Gbit/s O-SCM WDM PON. Eye diagrams of the unequalized data captured at $P_{\text{OLT_Tx}} = 5$ dBm are inset.

to achieve BERs below 10^{-4} by more than 6.5 dB. We note here that the received power at the OLT only varies between -0.1 dBm to 2 dBm over the 10 dB range of launch powers, indicating that the RSOA was deeply saturated and the downlink signal is efficiently erased.

4.3.2 Full-Duplex Operation Over a 20 km WDM PON

As illustrated in Fig. 4–4, the feeder fiber and DDF are replaced in the ODN and the system parameters are fully optimized to demonstrate the architecture’s performance in a more realistic scenario. The ONU coupling ratio (60/40) and downlink ER (~ 5.1 dB) balance the performance of both channels under full-duplex operation. We then repeat the BER measurements and characterize the system performance as a function of $P_{\text{OLT_Tx}}$ in Fig. 4–8.

In Fig. 4–8(a) the downlink channel performs in a power limited fashion where the BER steadily decreases in a waterfall curve with increasing $P_{\text{OLT_Tx}}$. The downlink’s minimum launch powers for operating are 1 dBm and 3 dBm which correspond to receiver sensitivities of -13 dBm and -11 dBm for the RS(255,223) and RS(255,239) FEC codes, respectively.

The uplink channel’s performance during symmetric operation is shown in Fig. 4–8(b). The uplink BER never reaches below 10^{-2} when the data is unequalized due to the severe ISI caused by the RSOA’s narrow modulation bandwidth, as evident from the large intensity noise present in the

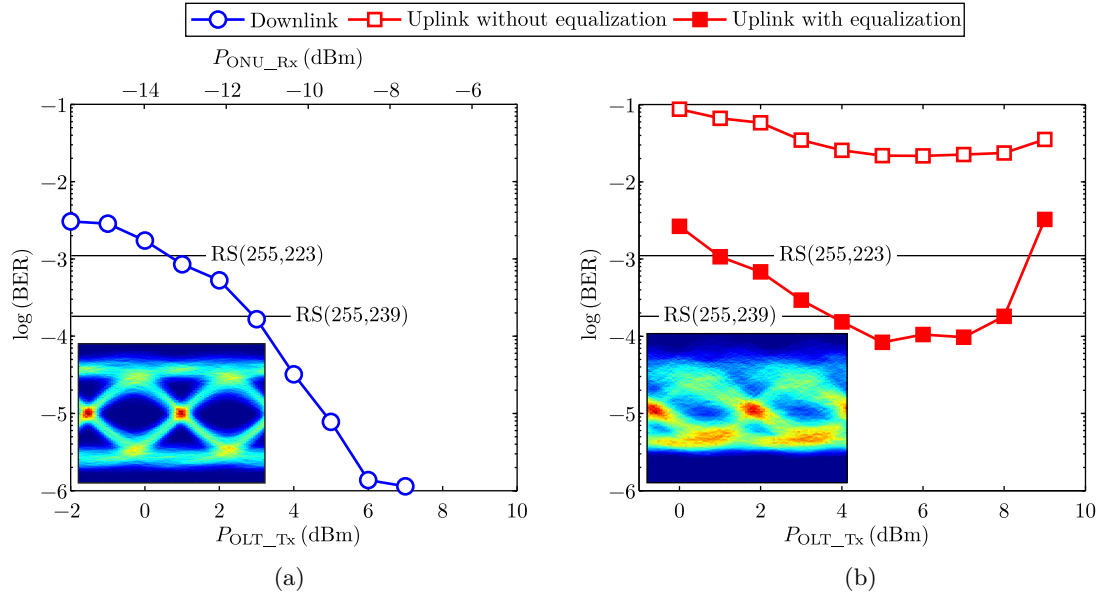


FIGURE 4–8: Symmetric performance of the 5 Gbit/s O-SCM architecture over the 20 km single feeder WDM PON. Measured BER of the (a) downlink and (b) uplink channels. Eye diagrams of the unequalized data captured at $P_{OLT_Tx} = 5$ dBm are inset.

inset eye diagram. This demonstrates the necessity of electronic equalization at bit rates beyond 2.5 Gbit/s. Using a DFE equalizer with 6 forward and 1 feedback taps improves the uplink BER in some cases by more than two orders of magnitude. Looking at the equalized uplink data, we notice three distinct regions to the BER curve. When $P_{OLT_Tx} < 4$ dBm, the uplink performance is primarily power limited and steadily improves as the RSOA achieves gain saturation. The best region for the uplink is from $P_{OLT_Tx} = 4$ dBm to 7 dBm where the RSOA is saturated and the downlink channel is efficiently erased. However, because the upstream power is restricted by the RSOA's saturated gain, it reaches an error floor near 10^{-4} as the system becomes RB noise limited. At launch powers beyond 7 dBm the uplink performance quickly degrades as SBS becomes the dominant upstream impairment and the electronic equalizer loses its efficacy.

This noise floor is primarily due to the baseband transmission overlapping with the OBI. It is interesting to note that an uplink error floor was not encountered in the previous architecture, where the SCM uplink channel was separated from the low frequency noise after down-conversion and filtering. This is a design trade-off, where the uplink is sent at baseband to maximize upstream bit rate, but some OBI can be tolerated with the aid of FEC.

Figure 4–9 compares the BER curves for both transmission directions, assuming electronic equalization of the uplink channel. Here we can define two operating regions over which both channels operate below the FEC thresholds. The lower boundary is fixed by the minimum launch power required for full-duplex transmission. This operating point is dictated by the typical design trade-offs common to bidirectional WDM PONs using remodulation: downlink ER, RSOA gain and ONU coupling ratio. As demonstrated in Chapter 3, selecting a suboptimal coupling ratio results in an imbalance between the uplink and downlink power budgets. This results in an offset between their respective operating ranges, thus reducing the system’s overall operating regions. At high launch powers (≥ 8 dBm) the system’s uplink channel performance degrades as upstream impairments, such as RB and SBS, become more dominant and cannot be tolerated by the O-SCM technique.

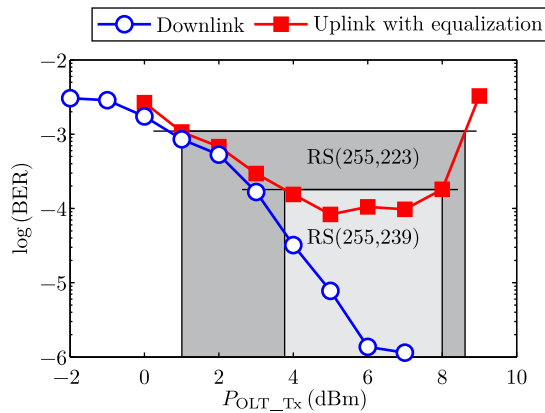


FIGURE 4–9: Operating regions of the 5 Gbit/s O-SCM architecture over the 20 km single feeder WDM PON. The shaded regions represent launch powers where both channels operate below the BER thresholds listed in Table 4–1.

The choice of the channels’ FEC encoding normally depends on the quality of service requirements of the network operators and industry standards. If we assume that both channels are encoded in RS(255,223) the system operates over a wide range of launch powers from 1 dBm to 8.5 dBm. The drawback is a higher 12.5% coding overhead that reduces the net bit rate to ~ 4.4 Gbit/s. If both channels use RS(255,239) the operating region shrinks to a range between 4 dBm to 8 dBm, but the coding overhead is reduced by half to 6.3% and a net bit rate of ~ 4.7 Gbit/s. In this case though, the uplink channel may not leave enough margin below the FEC threshold to meet the network operator’s quality of service requirements.

It is well known that increasing the transmission power in WDM PONs using remodulation does not necessarily provide better performance [46]. Assuming RS(255,223) coding, this O-SCM WDM PON architecture relaxes this launch power design constraint to a wide 7.5 dB range by providing enhanced resilience to RB and reflections while maintaining efficient use of the RSOA's modulation bandwidth to enable higher transmission rates. Thus operators are given additional flexibility to help manage network variations in real-world deployments.

4.4 Summary

In this chapter we presented a second generation O-SCM architecture for WDM PONs. Experimentally, we demonstrated full-duplex transmission at 5 Gbit/s over a 20 km single feeder PON using low cost IM/DD transceivers and data remodulation. Electronic equalization through offline processing compensated for the limited bandwidth of a directly modulated RSOA-based colourless ONU transmitter. Full-duplex operation commences at a low 1 dBm OLT launch power and spans up to 8.5 dBm assuming standards compatible RS FEC encoding. The experimental results demonstrate greater bandwidth efficiency than other SCM techniques and a twofold increase in symmetric data rates from the previous O-SCM implementation in Chapter 3. The low launch power requirements and tolerance to uplink impairments ease some well known design constraints for bidirectional WDM PONs and provide additional flexibility for very little additional cost, thus making the design an attractive solution for network operators.

CHAPTER 5

10 Gbit/s SCM WDM PONs with Higher-Order Modulation Formats

IN RECENT YEARS, DSP has proven to be an effective technique in transport network systems by replacing expensive optical components with high-speed transceiver electronics [67,68]. There is great potential for access networks to build upon these signal processing techniques using lower speed electronic components to achieve significant performance increases from economical optoelectronic transmitters.

In Chapter 3 we introduced the concept of O-SCM WDM PONs, where portions of the uplink and downlink channels are allowed to overlap in order to improve the channels' symmetric bit rates. In Chapter 4 the SCM channel spanned the entire 10 GHz bandwidth of the optoelectronic hardware, effectively limiting the symmetric bit rate of this approach to 5 Gbit/s. Although a 10 Gbit/s SCM WDM PON was recently demonstrated [90], it required cost prohibitive high bandwidth (30 GHz) receivers at the ONU. It is clear that we must take a new approach in order to achieve symmetric 10 Gbit/s rates if we limit ourselves to economical 10 GHz optoelectronic components.

In this chapter we outline the development of a third generation SCM WDM PON architecture that provides symmetric bit rates in excess of 10 Gbit/s within a limited 10 GHz of electrical bandwidth. Instead of NRZ binary modulation, the new DSP-based architecture implements higher-order QAM formats to provide greater bandwidth efficiency. The addition of SRRC pulse shaping further increases the channels' spectral efficiency, facilitating separation of the upstream and downstream electrical spectra and enabling full-duplex operation within the bandwidth limits of our commercial optoelectronics.

This chapter is organized as follows: Section 5.1 briefly discusses the concepts of higher-order modulation and pulse shaping, and introduces DSP spectral pre-compensation as a way of transmitting pulse shaped QAM signals with cost effective RF and optoelectronic hardware. In Section 5.2 we describe the primary building blocks of realizing a M-QAM SCM WDM PON, including the

physical architecture, DSP transmitter and receiver stacks, and optical enhancement with offset filtering. Additionally, we characterize the backscattered optical power from the ODN and verify the onset launch power for SBS. Finally, the chapter is summarized in Section 5.3.

5.1 Spectrally Efficient M-QAM SCM WDM PONs

In the previous chapters, the data for each channel was modulated onto the laser intensity using a NRZ binary scheme. This is one of the simplest and the most widely implemented modulation scheme in digital communication systems [22]. In this section, we will expand the concept of digital modulation and introduce more complex schemes to improve spectral efficiency by transmitting more information in a smaller channel bandwidth.

5.1.1 Generating M-QAM Signals with IM/DD Optoelectronics

In Fig. 5–1, we illustrate a simple modulator where binary data is separated into k bit blocks and each block sequence is mapped into a signal $s_m(t)$, where $1 \leq m \leq 2^k$. The data can be encoded into $s_m(t)$ using amplitude, phase, frequency or combinations thereof. In this investigation, we will focus on modulation schemes that allow us to maintain simple IM/DD transceivers.

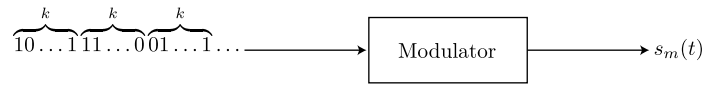


FIGURE 5–1: A memoryless digital modulator [50].

Pulse Amplitude Modulation Signals

A PAM signal is defined [50] as

$$s_m(t) = A_m p(t), \quad 1 \leq m \leq M \quad (5.1)$$

where $M = 2^k$, $p(t)$ is a real valued pulse signal, and

$$A_m = 2m - 1 - M, \quad m = 1, 2, \dots, M \quad (5.2)$$

is the information carrying signal amplitude. In its simplest form Eq. (5.1) represents a NRZ signal when $k = 1$, $A_m = \pm 1$ and $p(t)$ is a rectangular pulse. When $k > 1$, each of the M constellation points maps to a k bit symbol. Figure 5–2 illustrates eye diagrams for two example PAM signals.

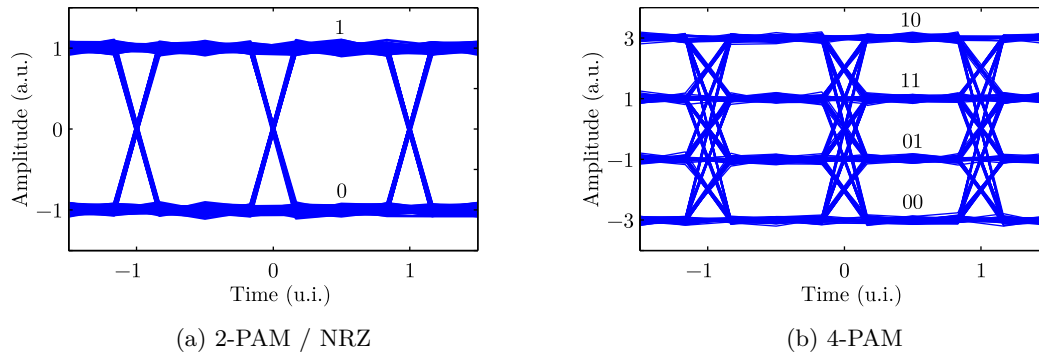


FIGURE 5-2: Eye diagrams of multilevel PAM signals with a rectangular pulse shape at $3S_a/\text{Symbol}$. The inset labels show the binary symbol value of each level assuming Gray encoding.

Quadrature Amplitude Modulation Signals

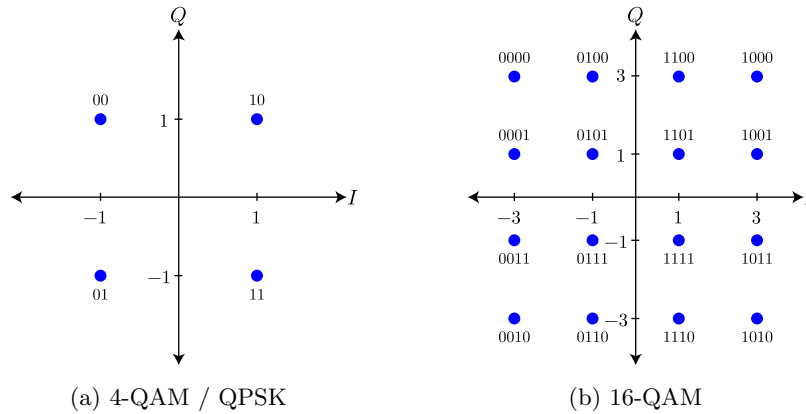
A QAM signal is generated by combining two PAM signals that are placed onto two quadrature orthogonal carriers. The resultant signal is expressed as follows

$$\begin{aligned}
 s_m(t) &= \Re[(A_{mi} + jA_{mq})g(t)e^{j2\pi f_{sc}t}], \quad m = 1, 2, \dots, M, \quad 0 \leq t \leq T \\
 &= A_{mi}g(t) \cos(2\pi f_{sc}t) - A_{mq}g(t) \sin(2\pi f_{sc}t)
 \end{aligned} \tag{5.3}$$

where A_{mi} and A_{mq} are the information carrying amplitudes of the quadrature carriers and $g(t)$ is the signal pulse [50]. The information contained in $s_m(t)$ can now be mapped into a two-dimensional constellation where each point represents a k bit symbol. Figure 5-3 shows two example I - Q constellations for the special case where A_{mi} and A_{mq} take discrete values $\{(2m - 1 - M), m = 1, 2, \dots, M\}$ forming rectangular constellations for QPSK ($M = 4$) and 16-QAM ($M = 16$).¹ In this case the symbols are organized using a Gray coding scheme, where adjacent symbols only differ by one binary digit. This helps to minimize errors during decoding due to amplitude noise [50]. Gray coding is assumed for all QAM constellations throughout this thesis.

Figure 5-4 illustrates a simplified QAM transmission scheme. At the transmitter shown in Fig. 5-4(a), the binary data is mapped into symbols $A_m = A_{mi} + jA_{mq}$. The in-phase and quadrature amplitudes are mixed onto two orthogonal carriers and recombined to form the M-QAM signal

¹ Although the labels QPSK and 4-QAM can be used interchangeably to describe a QAM signal of order $M = 4$, for clarity the former will be used throughout this thesis.


 FIGURE 5–3: Ideal I - Q constellation maps for Gray encoded QAM signals.

$s_m(t)$. In Fig. 5–4(b), the received signal $r(t)$ is mixed with phase matched orthogonal carriers to recover the in-phase $I(t) = A_{mi}g(t)$ and quadrature-phase $Q(t) = A_{mq}g(t)$ signal components after low pass filtering.

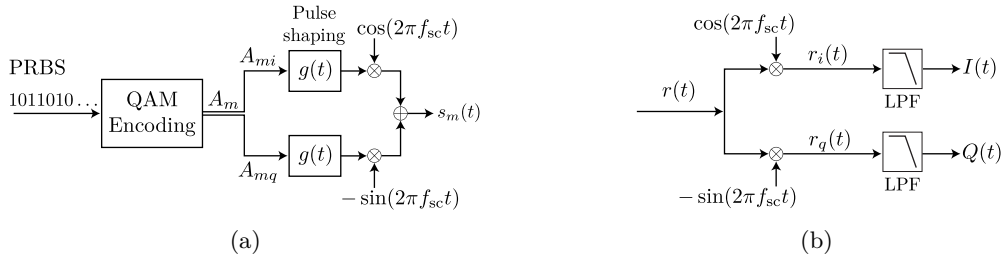


FIGURE 5–4: General (a) modulation and (b) demodulation schemes for a QAM signal.

Assuming an ideal transmission channel, the demodulation process is given by

$$r_i(t) = \cos(2\pi f_{sc}t) \cdot r(t) \quad (5.4)$$

$$= I(t) \cos(2\pi f_{sc}t) \cos(2\pi f_{sc}t) - Q(t) \sin(2\pi f_{sc}t) \cos(2\pi f_{sc}t)$$

$$= \frac{1}{2}I(t) + \frac{1}{2} \left[\cancel{I(t) \cos(4\pi f_{sc}t)} - \cancel{Q(t) \sin(4\pi f_{sc}t)} \right]$$

$$= \frac{1}{2}I(t) \quad (5.5)$$

and

$$r_q(t) = -\sin(2\pi f_{sc}t) \cdot r(t) \quad (5.6)$$

$$\begin{aligned} &= I(t) \cos(2\pi f_{sc}t) (-\sin(2\pi f_{sc}t)) - Q(t) \sin(2\pi f_{sc}t) (-\sin(2\pi f_{sc}t)) \\ &= \frac{1}{2}Q(t) - \frac{1}{2} \left[\cancel{I(t) \sin(4\pi f_{sc}t)} + \cancel{Q(t) \cos(4\pi f_{sc}t)} \right] \\ &= \frac{1}{2}Q(t), \end{aligned} \quad (5.7)$$

where the residual high frequency components are efficiently removed by a LPF stage with a cutoff frequency of less than $2f_{sc}$.

5.1.2 Square-Root Raised Cosine Pulse Shaping

The frequency spectrum of the PAM and QAM signals is influenced by the signal pulse shape. As we encountered in Chapter 4 with the RSOA, if a signal's bandwidth exceeds that of the band-limited channel then ISI will result from the adjacent information symbols. It is therefore important to transmit information channels with high spectral efficiency in order to operate within these bandwidth limits. According to the Nyquist pulse shaping criterion, certain signal pulse shapes can result in zero ISI [50]. One such pulse shape is the raised cosine, which has frequency characteristics

$$X_{RC}(f) = \begin{cases} T & \text{if } 0 \leq |f| \leq \frac{1-\alpha}{2T} \\ \frac{T}{2} \left\{ 1 + \cos \left[\frac{\pi T}{\alpha} \left(|f| - \frac{1-\alpha}{2T} \right) \right] \right\} & \frac{1-\alpha}{2T} \leq |f| \leq \frac{1+\alpha}{2T} \\ 0 & |f| > \frac{1+\alpha}{2T}, \end{cases} \quad (5.8)$$

where α is called the *roll-off factor* with values in the range $0 \leq \alpha \leq 1$ and T is the symbol duration.

The impulse response for the raised cosine spectrum is then given by

$$x_{RC}(t) = \frac{\sin\left(\frac{\pi t}{T}\right) \cos\left(\frac{\pi \alpha t}{T}\right)}{\frac{\pi t}{T} \left(1 - \frac{4\alpha^2 t^2}{T^2}\right)}. \quad (5.9)$$

Figure 5-5 illustrates the time and frequency domain of a raised cosine pulse for different roll-off factors. As α is reduced from 1 to 0, the bandwidth occupied by the signal decreases from the symbol rate $R_s = \frac{1}{T}$ to $\frac{1}{2T}$. At $\alpha = 0$ the frequency response is that of an ideal LPF.

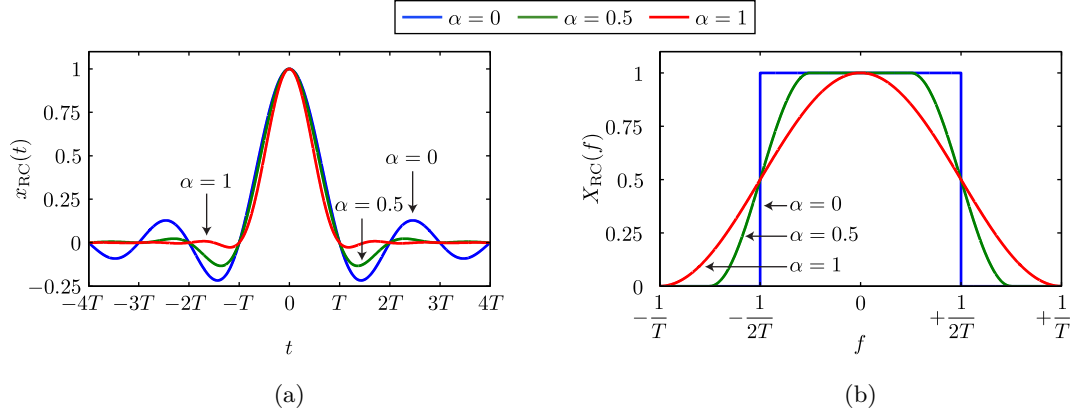


FIGURE 5-5: Raised cosine (a) impulse response and (b) frequency domain spectrum. We note that $x_{RC}(t)$ has zero-crossings at $t = \pm T, \pm 2T, \dots$ which satisfies the Nyquist pulse shaping criterion.

In practical implementations the filtering stage can be divided between the transmitter and receiver. Known as *matched filtering*, the cascade of transmitter and receiver filters approximates the overall response of the raised cosine spectrum. In an ideal channel with matched filtering

$$X_{RC} = G_T(f)G_R(f) = |G_T(f)|^2 \quad (5.10)$$

where $G_T(f)$ and $G_R(f)$ are the frequency responses of the transmitter and receiver filters, respectively. We can solve for the filter response of the matched SRRC filters

$$G_T(f) = \sqrt{|X_{RC}(f)|} \exp^{-j2\pi f t_0} \quad (5.11)$$

$$G_R(f) = G_T^*(f) = \sqrt{|X_{RC}(f)|} \exp^{+j2\pi f t_0} \quad (5.12)$$

where t_0 is an arbitrary delay [50]. In the time domain, the impulse response of the SRRC pulse is

$$x_{SRRC}(t) = \frac{\left(\frac{4\alpha t}{T}\right) \cos\left[\frac{\pi(1+\alpha)t}{T}\right] + \sin\left[\frac{\pi(1-\alpha)t}{T}\right]}{\left(\frac{\pi t}{T}\right) \left[1 - \left(\frac{4\alpha t}{T}\right)^2\right]}. \quad (5.13)$$

Figure 5-6 illustrates the time and frequency domain response of the SRRC filter for different roll-off factors. Again we see that as α is reduced from 1 to 0, the bandwidth occupied by the signal decreases from $R_s = \frac{1}{T}$ to $\frac{1}{2T}$. In the time domain, decreasing α adds more ripples and extends the pulse duration. Generating SRRC pulses with small α therefore requires higher-order FIR filters, providing greater spectral efficiency at the expense of added complexity.

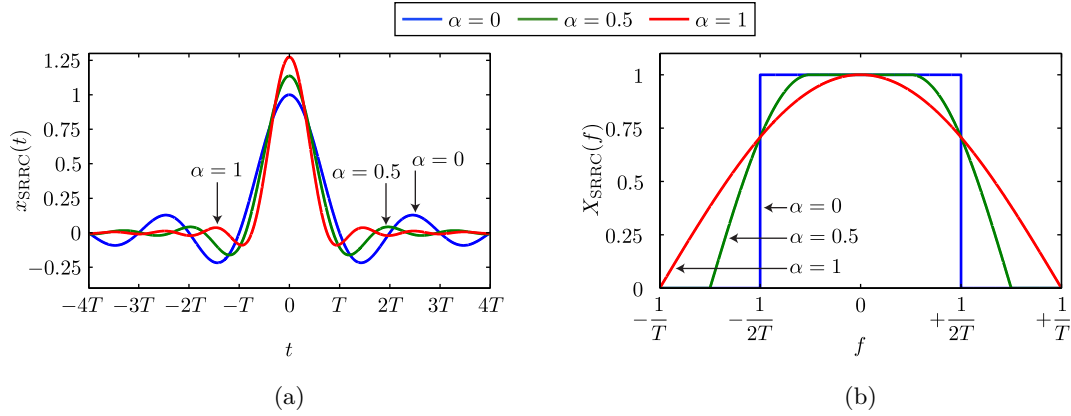


FIGURE 5–6: SRRC (a) impulse response and (b) frequency domain spectrum.

Using Eq. (5.3) we can now specify a SRRC pulse shaped band pass QAM signal of order M

$$s_m(t) = A_{mi}x_{\text{SRRC}}(t) \cos(2\pi f_{sc}t) - A_{mq}x_{\text{SRRC}}(t) \sin(2\pi f_{sc}t), \quad m = 1, 2, \dots, M \quad (5.14)$$

with a first-null channel bandwidth

$$B = (1 + \alpha) \times R_s. \quad (5.15)$$

Equations (5.14) and (5.15) will be the basis for designing the downlink and uplink channels throughout the rest of this chapter.

5.1.3 DSP Spectral Pre-compensation for Bandwidth-Limited Devices

An important condition for the SRRC matched filtering in Eq. (5.10) is that the channel should be ideal. That is, the frequency response of the channel $C(f) = 1$ for $|f| \leq f_c$, where f_c is the cutoff frequency of the band-limited channel. In the case of an optical transmission system, the channel response includes the optical fiber as well as the transceiver hardware. Here we assume that the fiber's response is flat for our moderate baud rates, and so we focus our attention to the electronics and optoelectronic components in the transceivers.

We can look at the bandwidth limiting components summarized in Table 5–1 to determine how this assumption affects the design of our M-QAM SCM WDM PON. All of the major downlink channel components are rated for operation at ~ 10 GHz or above, and the uplink's obvious bottleneck is the RSOA. We again stress that because of the RSOA's slow bandwidth roll-off, even

transmitting SRRC pulse shaped channels within the 2 GHz band will result in ISI. To overcome this we need a means of approximating a flat channel response.

TABLE 5–1: Summary of the bandwidth limiting components in the downlink and uplink transmission channels. Note that this is the -3 dB electrical bandwidth.

Downlink		Uplink	
Component	Bandwidth (GHz)	Component	Bandwidth (GHz)
p-i-n photoreceiver	9.5	RSOA (80 mA)	2.2
RF amplifier	10	p-i-n photoreceiver	9.5
EML	11	RF amplifier	10
RF bias-tee	15	RF bias-tee	12
RF DC blocks	18	RF DC blocks	18
RF attenuators	18	RF attenuators	18

In the literature, analog resistor-capacitor circuits have been used as high pass filters to extend the modulation bandwidth of RSOAs [57,59,63,112] by attenuating the lower frequency components of the uplink binary signal and providing more relative power to the high frequency components. The high pass filter effectively acts as the inverse to the RSOA’s modulation response roll-off, resulting in a flatter frequency response over the band of interest.

Figure 5–7 illustrates an example of how we can apply a similar approach in DSP by designing a FIR filter that approximates the inverse of the RSOA’s modulation response. Here we see that cascading a pre-compensation filter $H_{\text{FIR}}(f)$ to the RSOA with frequency response $H_{\text{RSOA}}(f)$ results in an effectively flat output response $X(f) = H_{\text{FIR}}(f) \cdot H_{\text{RSOA}}(f)$. The resulting modulation output now extends to ~ 6 GHz, albeit at a lower signal power.

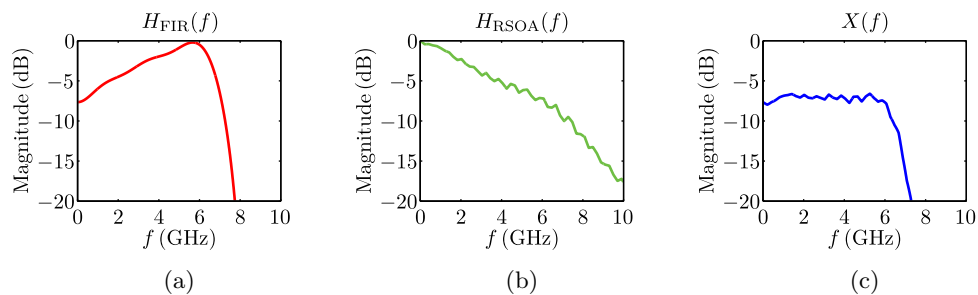


FIGURE 5–7: Magnitude response plots of the (a) 16th order FIR filter, (b) RSOA modulation response at 80 mA bias and (c) pre-compensated RSOA response.

As we will see in the experimental demonstrations that follow in Chapter 6, a similar approach can be used for the downlink signal to compensate for the moderate roll-off of the p-i-n and EML as the M-QAM channel approaches the upper bounds of the 10 GHz operating bandwidth.

5.2 Building Blocks of a 10 Gbit/s SCM WDM PON

A primary challenge in designing a SCM solution is to ensure that the uplink and downlink RF channels are sufficiently separated to facilitate band pass filtering. In this section we will outline the building blocks needed to implement a M-QAM SCM WDM PON with wavelength reuse and RSOA-based colourless ONU transmitters. We will implement the spectrally efficient M-QAM transmission channels introduced in Section 5.1 to facilitate a symmetric 10 Gbit/s solution that fits both channels within a 10 GHz band. We intentionally limit ourselves to using 10 GHz hardware in order to maintain economic viability and to leverage the commercially available hardware designed for existing 10 Gbit/s TDM PON standards.

5.2.1 Physical PON Architecture

In Fig. 5–8 we illustrate the concept behind the RF channel allocation using the pulse shaped M-QAM modulation technique described in Section 5.1. The downlink channel will reside in the high frequency section of the 10 GHz band on a subcarrier f_{DL} . Whereas the uplink channel, on a subcarrier f_{UL} , will occupy the lower frequency portion to reduce the effects of the RSOA's modulation bandwidth. In the upstream transmission, residual noise from the downlink RF channel will remain present due to reflections and RB. The optical architecture of the PON is similar to previous experiments, with the new addition of an offset OBPF at the OLT receiver to optically enhance the upstream signal. This will be discussed more thoroughly in Section 5.2.3.

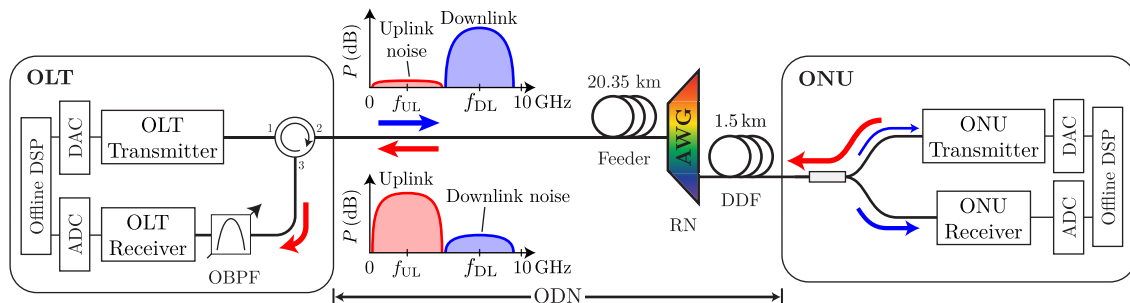


FIGURE 5–8: High level illustration of the 10 Gbit/s M-QAM SCM WDM PON including the downstream and upstream RF channel allocations.

5.2.2 Offline DSP Framework

Using the techniques described in Section 5.1, we developed a new DSP framework to transmit and receive SRRC pulse shaped M-QAM signals over a single feeder WDM PON with wavelength reuse. These spectrally efficiency signals will allow the downlink and uplink channels to coexist within the available 10 GHz bandwidth, while achieving 10 Gbit/s full-duplex data rates. Block diagrams of the DSP performed on the transmitted and received signals are outlined in Figs. 5–9 and 5–10, respectively.

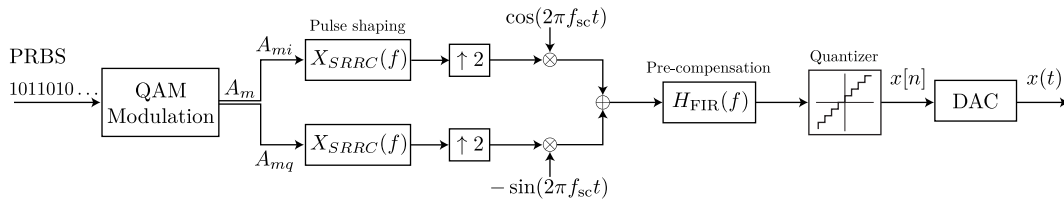


FIGURE 5–9: Block diagram of the M-QAM transmitter DSP.

For the transmitters, PRBSs of length $2^{23} - 1$ and $2^{31} - 1$ are first generated for the downlink and uplink respectively. A short 1 kSymbol preamble is then added to the beginning of each data sequence and the binary data is mapped into M-QAM symbols. The sequence is then truncated to fit within the 512 kSymbol memory of the DAC. A SRRC pulse shaping filter is then applied to the in-phase and quadrature-phase shaping components to increase spectral efficiency and reduce the effect of ISI. Each component is then upsampled and mixed with an orthogonal carrier at the desired RF subcarrier frequency f_{sc} , and then combined to form an equivalent band pass signal [50]. A FIR filter emphasizes the higher frequency portion of the signal to pre-compensate the channels' bandwidth limiting components. This enables the M-QAM electrical signals to be transmitted using low-cost optoelectronics by creating a flat power spectrum over the RF channel of interest. The signal is then quantized to 6 bit precision and transferred to the Micram VEGA II DAC for transmission. The DAC is operated at 20 GSa/s regardless of the baud rate and M-QAM order to maintain the 10 GHz of total channel bandwidth.

At the receiver, a real-time oscilloscope acts as an ADC to capture the data stream $r(t)$ at 40 GSa/s. After downsampling, the signal is mixed with phase matched orthogonal carriers to recover the in-phase and quadrature-phase signals, which then undergo SRRC matched filtering to eliminate ISI and remove out-of-band noise. After the timing synchronization and QAM decision blocks, the preamble symbols are used to remove the phase-locked loop (PLL) phase ambiguity.

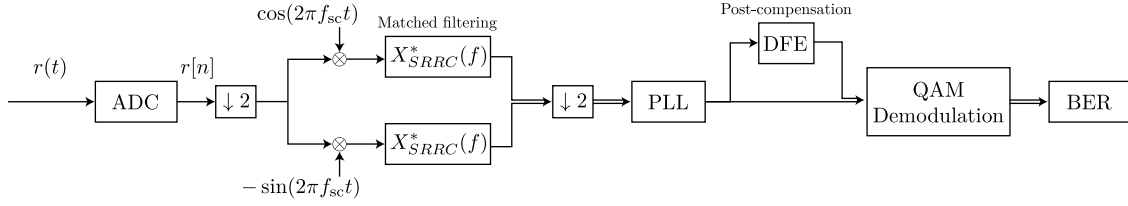


FIGURE 5–10: Block diagram of the M-QAM receiver DSP.

Additional post-compensation is optionally performed with a DFE to remove any residual ISI that remains due to a mismatch of the SRRC filters. The equalizer taps are initially trained using the preamble symbols and then dynamically adjusted using the LMS algorithm. The signal is then demodulated to binary data for BER calculation.

5.2.3 Offset Optical Filtering

In addition to the electronic compensation, we use an offset OBPF at the OLT receiver to optically enhance the upstream signal. Optical filter detuning has been shown to increase the RSOA's effective bandwidth by transforming the unwanted phase modulation due to the device's transient chirp into IM [57, 112]. The frequency response of the OBPF is given as

$$|H(w)|^2 = a + b\Delta f(w), \quad (5.16)$$

where a and b are the coefficients of attenuation and $\Delta f(w)$ is the slope of the filter at the offset wavelength. Around the offset wavelength operating point, the filter transforms the frequency variations into intensity variations as

$$P_{\text{out}}(w) = P_{\text{in}} \left[a + b\frac{\alpha}{2}(jw) \right], \quad (5.17)$$

where $\alpha = 2I \frac{d\phi}{dI}$ is the RSOA chirp parameter, I is the RSOA input current intensity, and ϕ is the phase of the output field. The factor jw represents a high pass contribution from the transformation of the phase modulation into IM by using the slope of the filter [57, 112]. The dependence on the filter's slope indicates that a sharp roll-off is essential to implement this technique. Figure 5–11 shows the OBPF profile and location of the upstream optical carrier. We define the filter offset as

$$\Delta\lambda = \lambda_{\text{OBPF}} - \lambda_{\text{UL}}, \quad (5.18)$$

where λ_{OBPF} is the centre of the filter's passband and λ_{UL} is the uplink carrier's peak wavelength.

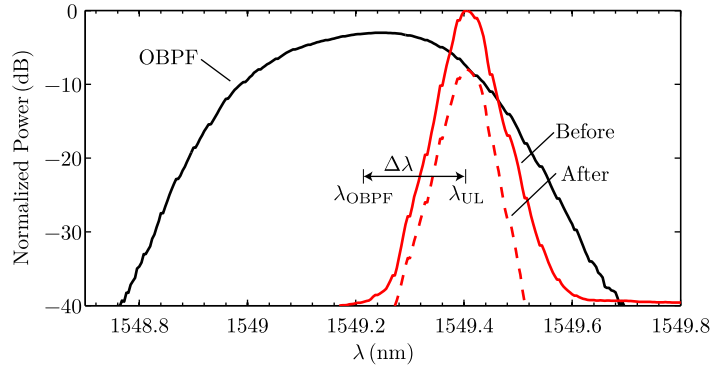


FIGURE 5–11: Measured profile of the JDSU VCF050 OBPF along with the upstream optical carrier’s power spectra measured before and after filtering. The optical powers were normalized to the peak power of the upstream carrier. $\Delta\lambda = -0.18$ nm.

Implementing offset optical filtering in a deployed WDM PON poses some system design challenges. Bulk enhancement of all WDM channels with a single device will be necessary to make it cost effective, and sensitivity to wavelength drift of the upstream carrier needs to be considered closely. A delay interferometer has been demonstrated to simultaneously enhance up to 34 WDM channels, assuming use of a commercial wavelength locker [113]. Recently, a narrow bandwidth AWG was used at the OLT to both enhance and demultiplex the WDM channels across the optical C-band with a wavelength drift tolerance of 10 GHz [60]. Electronic equalization has also been shown to increase tolerance to wavelength drift [59].

5.2.4 Upstream Impairments

As outlined in Section 1.2.3, there are three primary contributors to upstream impairments in bidirectional WDM PONs: Reflections, inter-channel crosstalk and RB [46]. In this study, we minimize the impact of static reflections by using optical connectors with oblique end facets, and reduce inter-channel crosstalk by separating the two transmission channels with SCM. In Fig. 5–12 we characterize the amount of backscattered optical power originating from the downstream signal.

The setup for the measurement is illustrated in Fig. 5–12(a). An EDFA and VOA control the CW launch power P_{Tx} of an EML laser with $\lambda = 1549.4$ nm. The CW light is launched into the ODN, where the reflective ONU is removed and the end of the DDF is capped. The average power of the backscattered signal P_3 is measured at port 3 of the circulator. Using Eq. (A.1) we can

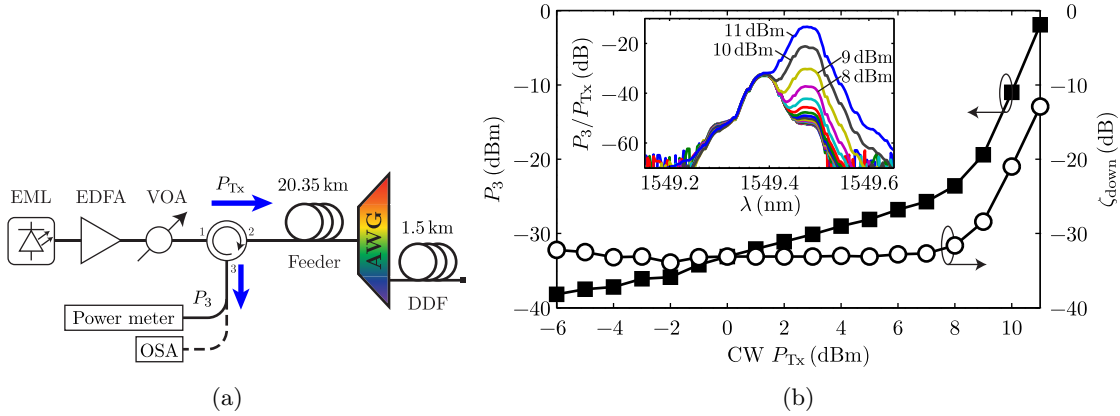


FIGURE 5–12: (a) Experimental setup and (b) measurement of the backscattering due to the downlink laser ($\lambda = 1549.4$ nm). OSA: optical spectrum analyzer.

determine the ratio of backscattered power to launch power [79]

$$\zeta_{\text{down}} = \frac{P_3}{P_{\text{Tx}}}.$$

Figure 5–12(b) shows the measurements of backscattered power and ζ_{down} . For $P_{\text{Tx}} \leq 7$ dBm, the ratio ζ_{down} remains fairly constant at approximately -33 dB, agreeing with values found in the literature [79]. When the CW launch power is further increased the backscattered power increases rapidly with the onset of SBS. The spectra of the backscattered signals are measured with an optical spectrum analyzer to verify this behaviour. The central peak is the *elastic* scattering due to RB, which maintains the same $\lambda = 1549.4$ nm as the carrier laser. As the launch power is increased further, a second peak begins to form with an optical frequency offset of ~ 10 GHz due to the *inelastic* SBS process.

5.3 Summary

This chapter presented the development of a third generation SCM WDM PON architecture. We motivated pulse shaped QAM signals as a way to improve spectral efficiency compared to NRZ solutions, which will enable symmetric 10 Gbit/s data channels to reside within the 10 GHz operating bandwidth. Furthermore, we outlined the key components and technologies necessary to experimentally implement the proposed architecture including a new DSP analysis framework, spectral pre-compensation for bandwidth-limited components and offset optical filtering. In Chapter 6 we will experimentally verify the performance of this third generation SCM WDM PON architecture.

CHAPTER 6

Experimental Demonstrations of M-QAM SCM WDM PONs

IN CHAPTER 5 we introduced the concept of higher-order modulation as a means of achieving symmetric data rates in excess of 10 Gbit/s for a third generation SCM WDM PON architecture. There we outlined how a combination of SRRC pulse shaping, spectral pre-compensation, offset optical filtering and electronic equalization can enable the two transmission channels to reside in just 10 GHz of electrical bandwidth. In this chapter we will confirm these results experimentally over a 20 km single feeder bidirectional WDM PON with wavelength reuse.

The rest of the chapter is organized as follows: In Section 6.1 we experimentally demonstrate the first SCM WDM PON with 5 Gbaud QPSK channels and look at the system's sensitivity to downlink subcarrier frequency and SRRC roll-off factor. In Section 6.2 we experimentally investigate the performance of a SCM WDM PON with 2.5 Gbaud 16-QAM downlink and 5 Gbaud QPSK uplink channels. We optimize the OBPF's wavelength offset, demonstrate the efficacy of spectral pre-compensation to transmit M-QAM signals on economical IM/DD transceivers, confirm the BER performance of the transmission channels and characterize the uplink's resilience to upstream impairments. In Section 6.3 we experimentally show the first SCM WDM PON with two 2.5 Gbaud 16-QAM channels. The channels' BER performance is characterized for different SRRC roll-off factors for both CW seeding and full-duplex scenarios, and the spectral efficiency of the 16-QAM channels is compared to the Shannon limit. In Section 6.4 we use a fixed and fully optimized optical test bed and offline processing code to directly compare the performance and design trade-offs of the architecture for all permutations of QPSK and 16-QAM channel formats. The line rate of each channel is increased to 11.25 Gbit/s to account for the 12.5% overhead of the RS(255,223) FEC encoding, providing a truly symmetric 10 Gbit/s payload. Finally, this chapter is summarized in Section 6.5

6.1 10 Gbit/s QPSK SCM WDM PON

In the following section, we characterize the performance of a SCM WDM PON with QPSK modulation for both the downlink and uplink channels. We achieve 10 Gbit/s bidirectional data rates over a single 20 km feeder and demonstrate BERs below the RS(255,223) FEC threshold for a wide range of OLT launch powers from 0 dBm to 9 dBm. At the time of publication, this was the first experimental demonstration of a symmetric 10 Gbit/s WDM PON with wavelength reuse and QPSK transmission using IM/DD for both the uplink and downlink directions [9].

6.1.1 Physical PON Architecture

The single feeder architecture used in this experiment is illustrated in Fig. 6–1. The OLT transmitter consists of a Micram VEGA II DAC with 6 bit precision driving an EML centred at 1549.57 nm. Following the EML, a booster EDFA and a VOA control the launch power P_{OLT_Tx} . The ODN comprises a 20.35 km feeder of standard single mode fiber (SMF-28e+), a 100 GHz AWG and a 1.5 km DDF and a 1.5 km DDF.

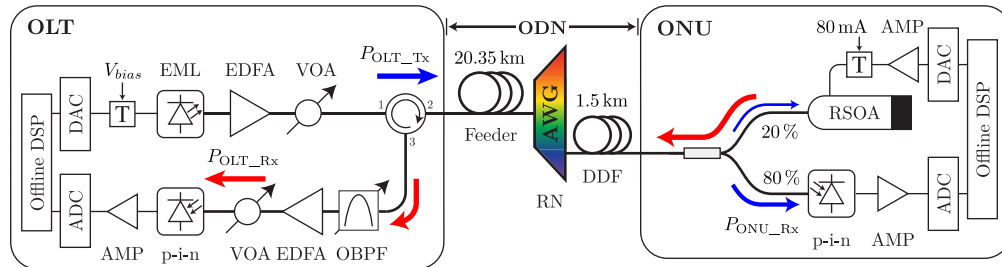


FIGURE 6–1: Physical architecture of the 10 Gbit/s QPSK SCM WDM PON. ADC: Agilent Infiniium DSC-X 93204A, AMP: RF amplifier, AWG: arrayed waveguide grating (100 GHz channel spacing), EML: CyOptics E4560 (11 GHz bandwidth), OBPF: JDSU VCF050 (0.3 nm bandwidth), p-i-n: Discovery Semiconductors DSC-R402 (10 GHz bandwidth), RSOA: CIP SOA-RL-OEC-1550, T: RF bias-tee.

At the ONU, a coupler taps off 80 % of the downstream signal for detection by the receiver comprised of a p-i-n photoreceiver, a RF amplifier, and a real-time oscilloscope performing 8 bit precision ADC. The remaining 20 % of the downstream signal seeds a RSOA with peak gain from 1530 nm to 1570 nm and 2.2 GHz modulation bandwidth. The RSOA uplink transmitter is directly modulated at $4V_{p-p}$, biased at 80 mA, and driven by a second DAC. The OLT receiver consists of a 0.3 nm tunable OBPF, a pre-amplifier EDFA and a VOA to fix the received power at $P_{OLT_Rx} = -2$ dBm, along with a p-i-n photoreceiver, RF amplifier and a similar ADC to capture the received signal.

In addition to the DSP pre-compensation, the effective uplink bandwidth is further increased by offsetting the centre of the OBPF from the upstream wavelength by an optimized $\Delta\lambda = -0.18$ nm.

6.1.2 Downlink Performance

We first characterize the 5 Gbaud QPSK downlink channel. The downlink signal has a roll-off factor of $\alpha_{DL} = 0.35$ and is centred on a $f_{DL} = 7.66$ GHz subcarrier to minimize overlap with the uplink channel. Figure 6–2(a) shows the frequency spectrum of the downlink signal that is loaded into the DAC, where the downlink channel occupies the upper portion of the electrical bandwidth. This leaves the low frequency portion of the bandwidth for the uplink channel. Figure 6–2(b) shows the measured power spectrum of the downstream signal received at the ONU. Here we note the presence of uplink channel RB noise due to the simultaneous upstream transmission.

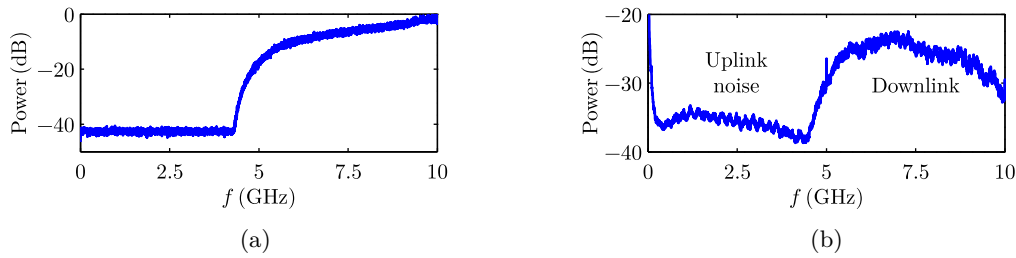


FIGURE 6–2: (a) Frequency content of the pre-emphasized downlink QPSK signal. (b) Measured power spectrum of the received downstream signal.

Figure 6–3 demonstrates the BER performance of the downlink channel during symmetric operation. Without electronic post-compensation at the receiver, the BER approaches an error floor near the FEC threshold at 10^{-3} . The spectra in Fig. 6–2 show that the transmitted channel extends beyond the 10 GHz channel bandwidth. Additionally, the received signal indicates that the channel band has become distorted at high frequencies primarily due to a sub-optimal pre-emphasis filter. We attribute the poor performance of the unequalized case to unwanted ISI resulting from SRRC filter mismatch, which violates the Nyquist pulse shaping criteria [50].

Adding a DFE with 4 forward and 1 backward symbol-spaced taps to the ONU receiver reduces the measured BER significantly. The electronic equalizer effectively removes the residual ISI due to the mismatched filter. This greatly improves the downlink BER performance and reduces the system’s sensitivity to channel distortion. As a result, the equalized downlink BER drops below the FEC threshold at $P_{OLT_Tx} > -2$ dBm corresponding to a receiver sensitivity of -13 dBm. The BER remains below the FEC threshold up to 9 dBm of launch power.

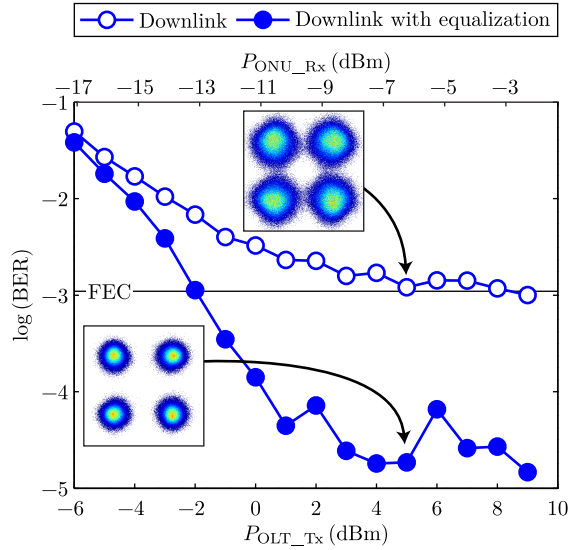


FIGURE 6-3: BER performance of the downlink QPSK channel after transmission over a 20 km PON. Constellation diagrams at $P_{OLT_Tx} = 5$ dBm are inset as indicated.

6.1.3 Uplink Performance

The uplink channel is a 5 Gbaud QPSK signal with a SRRC roll-off factor of $\alpha_{UL} = 0.15$ spanning a null-to-null bandwidth of 5.75 GHz. The uplink subcarrier frequency $f_{UL} = 2.97$ GHz minimizes the bandwidth effects of the RSOA while isolating the uplink channel from the low frequency OBI noise. Figure 6-4(a) shows the channel allocation of the upstream signal. A combination of spectral pre-emphasis at the transmitter and optical enhancement of the offset OBPF compensate for the RSOA's limited bandwidth. The received spectra in Fig. 6-4(b) demonstrates that the uplink channel extends with a flat response up to 6 GHz, far beyond the transmitter's ~ 2 GHz modulation bandwidth. It is important to note that the uplink channel overlaps with the downlink by approximately 1.5 GHz and so some level of inter-channel crosstalk will be present.

Figure 6-5 presents the uplink channel BER as a function of P_{OLT_Tx} . As the launch power increases, the uplink signal becomes power limited as the RSOA reaches gain saturation. The uplink signal operates below the FEC threshold for launch powers from 0 dBm up to 9 dBm. The addition of a DFE with 4 forward and 1 backward symbol-spaced taps at the OLT receiver further reduces the BER floor to 10^{-4} providing extra margin for the network operator. Maintaining this performance at such high launch powers demonstrates the system's resistance to upstream impairments such as RB, reflections and SBS.

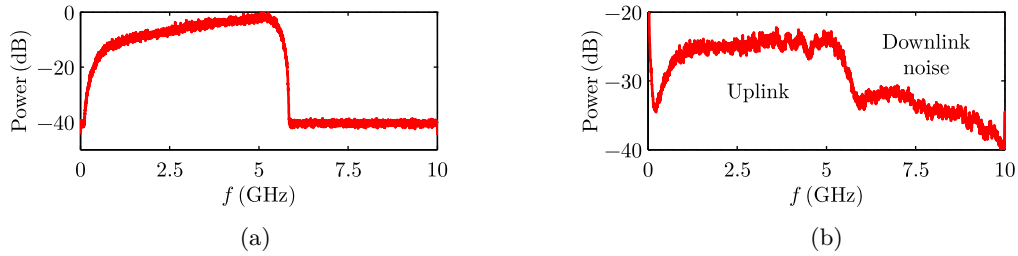


FIGURE 6–4: (a) Frequency content of the pre-emphasized uplink QPSK signal loaded into the DAC memory. (b) Measured power spectrum of the received downstream signal. We note the presence of the residual downlink channel which is amplified and reflected by the RSOA.

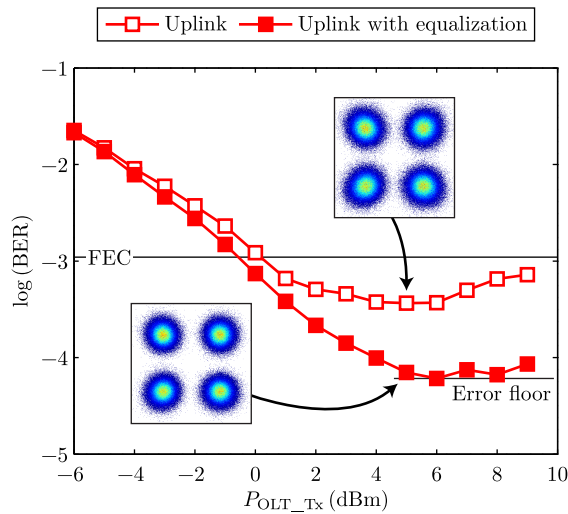


FIGURE 6–5: BER performance of the QPSK uplink channel in full-duplex operation. Constellation diagrams at $P_{OLT_TX} = 5$ dBm are inset as indicated.

6.1.4 Parameter Sensitivities

In Fig. 6–6 we investigate the system’s sensitivity to different downlink channel parameters while in full-duplex operation. In Fig. 6–6(a) we maintain $\alpha_{DL} = 0.35$ and shift the channel by varying the subcarrier frequency. At low f_{DL} , the upper portion of the downlink channel is no longer distorted and performs well below the FEC threshold both with and without equalization. This increases the amount of spectral overlap between the two channels and adds to the additional inter-channel crosstalk in the upstream signal. As a result, the uplink BER performance degrades. Increasing $f_{DL} > 7.5$ GHz reduces the inter-channel crosstalk on the upstream but causes distortion to the downlink channel as it further extends into the 10 GHz channel boundary. The choice of $f_{DL} = 7.66$ GHz used above provides a good performance balance between the two channels.

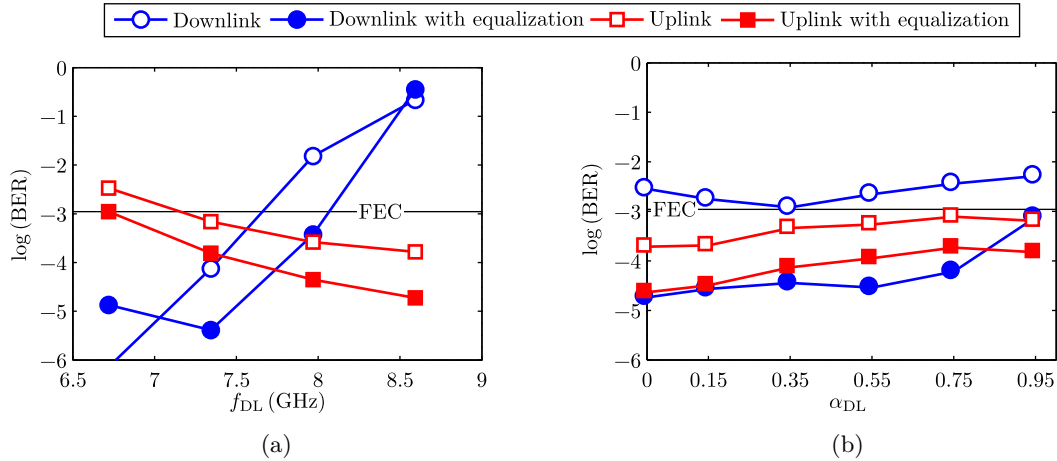


FIGURE 6–6: Characterizing the impact of the downlink channel’s (a) subcarrier frequency and (b) SRRC roll-off factor. P_{OLT_TX} is fixed at 5 dBm.

In Fig. 6–6(b) we vary the roll-off factor of the downlink SRRC pulse shaping to change the channel’s null-to-null bandwidth. f_{DL} was slightly reduced to 7.5 GHz for this measurement. In terms of BER performance, the downlink is quite insensitive to α_{DL} , except at 0.95 where the channel extends well beyond the 10 GHz boundary. As α_{DL} increases, the uplink channel’s BER slowly degrades as the inter-channel crosstalk from the downlink signal becomes more significant, but the BER never reaches above the FEC threshold.

6.1.5 Conclusion

In this section we presented a preliminary demonstration of a single feeder 10 Gbit/s QPSK SCM WDM PON architecture using low cost IM/DD optoelectronics and DSP techniques. We verified the system’s full-duplex performance over 20 km single feeder PON and achieved BERs below the RS(255,223) FEC threshold over a wide range of launch powers from 0 dBm to 9 dBm. Additionally we investigated the system’s sensitivity to the downlink channel’s subcarrier frequency and pulse shaping roll-off factor.

6.2 10 Gbit/s 16-QAM/QPSK SCM WDM PON

This section expands upon the concepts proposed in our initial demonstration in Section 6.1 by migrating the downlink channel from 5 Gbaud QPSK to 2.5 Gbaud 16-QAM. This improves the spectral efficiency and provides robust resistance to the inter-channel crosstalk due to reflections and RB. We use DSP spectral pre-compensation, offset optical filtering and electronic equalization to

compensate for the bandwidth-limited RSOA-based ONU transmitter. We demonstrate symmetric operation over a wide range of OLT launch powers from 1 dBm to 9 dBm, assuming standard RS(255,223) FEC codes with 12.5% overhead. The physical architecture and operating parameters used in this experiment are the same as those described in Section 6.1.1.

6.2.1 Downlink Performance

The downlink channel consists of a 2.5 Gbaud 16-QAM signal with a SRRC roll-off factor $\alpha_{DL} = 0.35$. In Fig. 6–7 we determine the downlink’s sensitivity to f_{DL} by moving the channel across the available electrical band. We first isolate the downlink transmission by blocking the input port to the RSOA to remove the upstream transmission and eliminate any crosstalk contribution. The downlink BER is then measured at different subcarrier frequencies without any spectral pre-compensation. When $f_{DL} \leq 6.5$ GHz the channel resides well within the ideal portion of the channel where the response is essentially flat. Here the SRRC pulse shaped transmissions achieve BERs $< 10^{-4}$ without any pre- or post-compensation. As f_{DL} increases beyond 6.5 GHz, the BER quickly degrades to a plateau of 10^{-2} as the channel pushes towards the 10 GHz boundary of the bandwidth-limited components. This distorts the upper portion of the channel causing a mismatch of the SRRC filter applied at the ONU receiver and thus violates the Nyquist pulse shaping criterion.

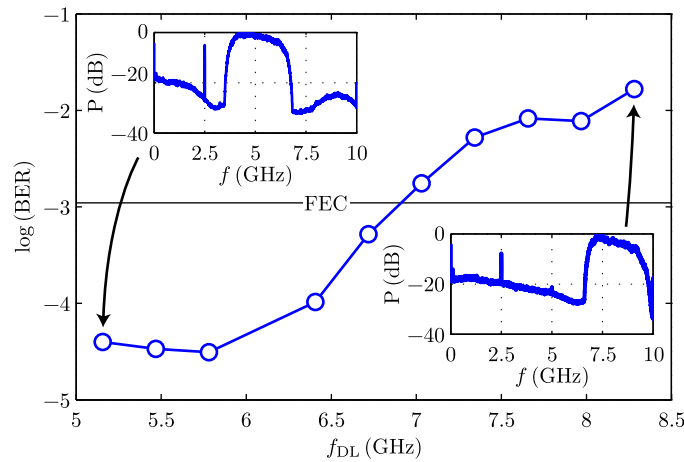


FIGURE 6–7: Uncompensated 16-QAM downlink channel performance for different sub-carrier frequencies. The electrical power spectra inset for 5.16 GHz and 8.28 GHz show the location of the channel within the available 10 GHz bandwidth. The OLT launch power is fixed at 5 dBm.

For symmetric transmission during the remaining experiments, the downlink is centred on a 7.66 GHz subcarrier to provide enough spectral separation from the uplink channel to minimize

inter-channel crosstalk while also reducing the distortion effects of the channel. An optimized 16th order FIR filter with 50 ps tap spacing is applied to the signal to pre-compensate for the roll-off of the channel.

Figure 6–8(a) presents a study of the downstream BER performance as a function of P_{OLT_Tx} with and without the aid of spectral pre-compensation. The resulting BER of the uncompensated downlink channel reaches an error floor near 10^{-2} due to severe ISI. When the transceiver distortion is pre-compensated for at the OLT, the downlink channel achieves BERs below the RS(255,223) FEC threshold for P_{OLT_Tx} greater than 0 dBm and quickly reaches the calculation floor of 10^{-5} . For $P_{OLT_Tx} \geq 5$ dBm the pre-compensation results in a BER improvement of at least three orders of magnitude. By using an optimized pre-compensation filter, no electrical equalization is required at the ONU and thus simplifies its design. Figures 6–8(b) and 6–8(c) show the spectra of the downstream signal with and without pre-compensation.

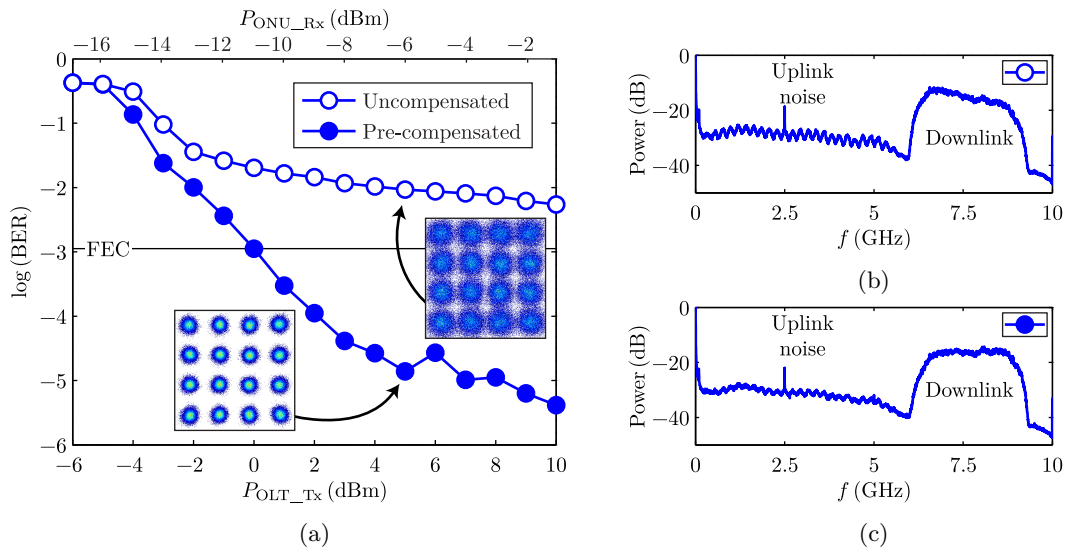


FIGURE 6–8: Effect of pre-compensation on the 2.5 Gbaud 16-QAM downlink transmission after 20 km. (a) BER performance with and without spectral pre-compensation. Constellation diagrams at $P_{OLT_Tx} = 5$ dBm are inset as indicated. The corresponding P_{ONU_Rx} at the ONU indicates a received power sensitivity of -11 dBm. Electrical power spectra of the (b) uncompensated and (c) pre-compensated downlink channel at $P_{OLT_Tx} = 5$ dBm. We note the presence of uplink channel RB noise due to the bidirectional nature of the proposed PON system.

6.2.2 Uplink Performance

The uplink channel comprises a 5 Gbaud QPSK signal with a roll-off factor $\alpha_{UL} = 0.15$ transmitted on a 2.97 GHz subcarrier. The smaller roll-off factor allows the uplink channel to occupy a null-to-null bandwidth of only 5.75 GHz. Maintaining the uplink channel away from baseband also provides some spectral separation from the low frequency RB beat noise [94]. Using the uplink electrical power spectra in Fig. 6–9, we observe that the combination of DSP pre-compensation and offset optical filtering results in a *flat* received power spectrum throughout the 6 GHz channel band.

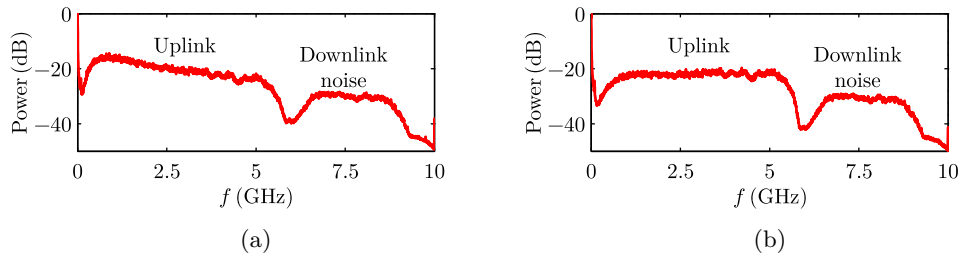


FIGURE 6–9: Electrical power spectra of the (a) uncompensated and (b) pre-compensated uplink channel after transmission over 20 km. $P_{OLT_Tx} = 5$ dBm and $\Delta\lambda = -0.18$ nm. We also note the presence of the residual downlink channel noise which is amplified and reflected by the RSOA.

In Fig. 6–10 we characterize the BER performance of the uplink transmission both with and without spectral pre-compensation. The uncompensated transmission cannot operate below the FEC threshold without an additional post-compensation DFE stage at the receiver. We see in Fig. 6–9(a) that the received uplink signal has a power imbalance of nearly 10 dB over the width of the channel. Similar to NRZ modulated signals [49], the RSOA’s smooth bandwidth roll-off enables the DFE to remove the residual ISI and achieve BERs below the FEC threshold for $P_{OLT_Tx} \geq 0$ dBm. Pre-compensating for the RSOA roll-off flattens the uplink channel, lowers the minimum launch power by 6 dB and sustains the operation up to 9 dBm of launch power. The BER reaches an error floor near 10^{-4} , which can further be reduced to $\sim 3 \times 10^{-5}$ with a DFE.

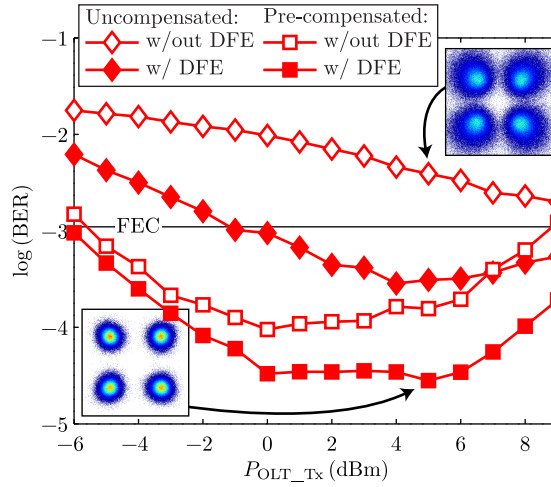


FIGURE 6–10: BER performance of the uplink channel with and without spectral pre-compensation for the RSOA. Constellation diagrams are inset as indicated. The OBPF is offset by -0.18 nm resulting in an average loss of 6.6 dB, including its insertion losses.

6.2.3 Optimizing the Offset OBPF

Optical filter detuning has been shown to increase the RSOA's effective bandwidth by transforming the unwanted phase modulation due to the device's transient chirp into IM [57, 60]. Figure 6–11 demonstrates the sensitivity of the uplink performance to the OBPF offset. For the uncompensated transmission, the uplink BER only dips below the FEC threshold at -0.27 nm. As found previously for NRZ signals [57], adding a DFE at the receiver reduces the wavelength sensitivity and widens the operating region of the offset filtering to 0.13 nm (~ 16 GHz).

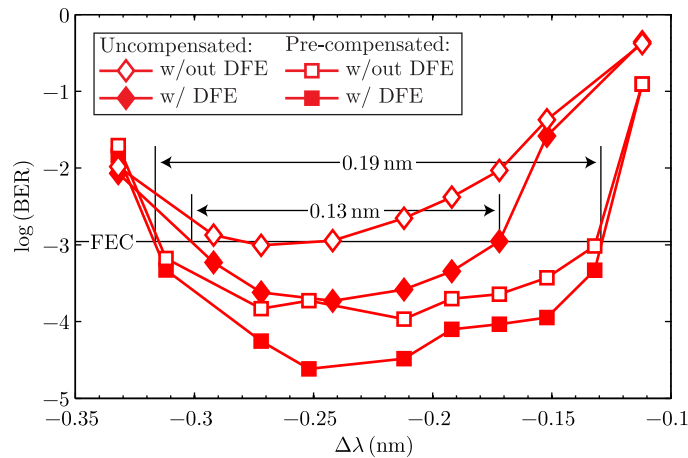


FIGURE 6–11: The impact of offset filtering and spectral pre-compensation on the uplink BER. $P_{\text{OLT_Tx}}$ is fixed at 5 dBm.

The ONU pre-compensation filter is optimized for each $\Delta\lambda$ to provide an upper bound on the system performance. In this case, the trends of the curves are the same regardless of whether or not a DFE is used. Pre-compensation reduces optical losses by achieving operation at the minimum $\Delta\lambda = -0.13$ nm. It simultaneously widens the operating region of the offset filtering to 0.19 nm (~ 24 GHz), which significantly lowers the system's overall sensitivity to laser wavelength drift. This improvement may be due in part to the added sensitivity resulting from pre-amplification at the OLT.

6.2.4 Resilience to Upstream Impairments

In wavelength reuse systems where the RSOA is seeded with a modulated downlink signal, inter-channel crosstalk results from incomplete erasure of the downlink data and impacts the uplink transmission [43]. The impact of inter-channel crosstalk on the uplink channel BER performance is shown in Fig. 6–12.

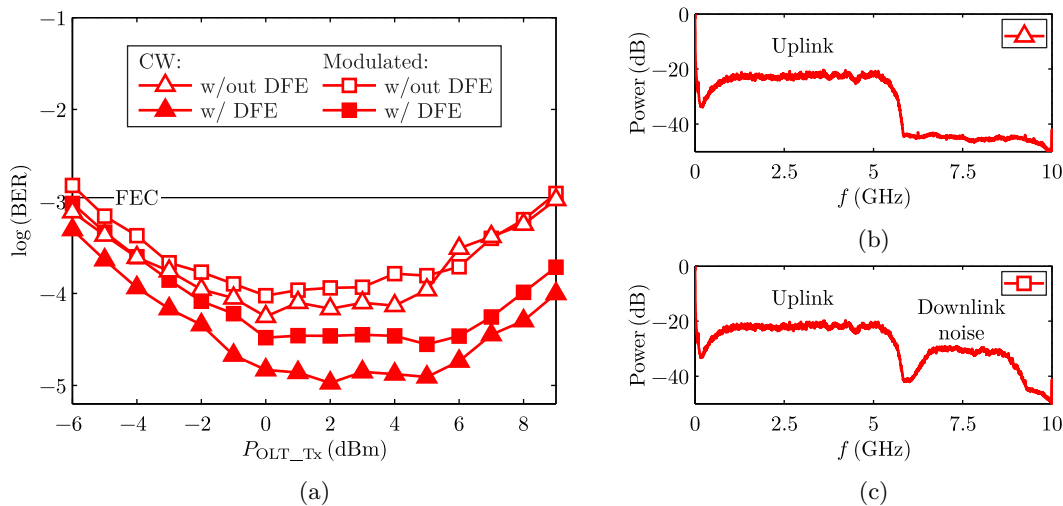


FIGURE 6–12: The inter-channel crosstalk's impact on the uplink channel transmission. (a) BER performance as a function of OLT launch power. Electrical power spectra of the received upstream signal with (b) CW and (c) modulated downlink seed light. $P_{OLT_Tx} = 5$ dBm and $\Delta\lambda = -0.18$ nm.

We see in Fig. 6–12 that there is no power penalty in terms of P_{OLT_Tx} as a result of downlink modulation and only a $1.5 - 2\times$ increase in BER. This is important in two ways: 1) here the downlink ER is *maximized* to facilitate transmitting 16-QAM signals; and 2) the residual downlink noise is still strongly present in the downlink channel band due to the high pass filtering effect

of the gain saturated RSOA as per Fig. 6–12(c). These results confirm that strong erasure of the downlink is *not* required for wavelength reuse in this M-QAM SCM system because the RF channels are spectrally separated and the out-of-band noise is efficiently removed in DSP at the OLT receiver.

The impact of RB on the performance of bidirectional PONs has been well studied [46]. In Fig. 6–13 we demonstrate its effect on the uplink OSRBR from Eq. (A.4), as measured at the port 3 output of the OLT circulator [79].

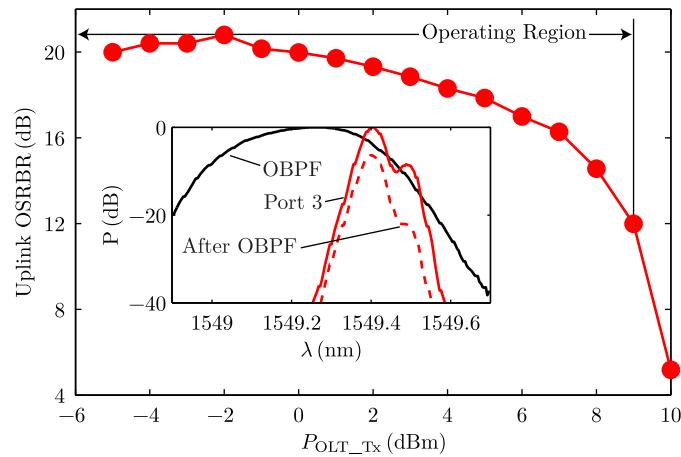


FIGURE 6–13: Influence of backscattering on the uplink channel performance. The inset shows the optical spectra of the received uplink signal before and after the OBPF at $P_{\text{OLT_Tx}} = 9$ dBm. The OBPF profile is included for reference.

The behaviour of the OSRBR measurement corresponds well to the BER curves in Figs. 6–10 and 6–12. At launch powers ≤ 0 dBm the OSRBR remains constant ~ 20 dB where the BER steadily decreases with $P_{\text{OLT_Tx}}$ indicating a power limited system. As the launch power increases further, the OSRBR slowly decreases as the RSOA’s gain saturates, causing the BER curves to reach an error floor as the system becomes RB noise limited. As previously demonstrated in Section 5.2.4, SBS becomes the dominant noise source on the upstream signal when $P_{\text{OLT_Tx}}$ is above 6 dBm and deteriorates the uplink BER performance. However, in this case the system remains operational up to 9 dBm corresponding to just 12 dB of OSRBR. The inset of Fig. 6–13 illustrates that the system’s resilience to SBS is a direct result of the offset OBPF, as its characteristic 10 GHz frequency offset sets it further down the filter’s stop band.

6.2.5 Conclusion

In this section we presented a 10 Gbit/s SCM WDM PON architecture with 16-QAM downlink and QPSK uplink transmission channels. We demonstrated the system's full-duplex operation over a 20 km single feeder PON and achieved BERs below the FEC threshold. We verified the effectiveness of spectral pre-compensation to enable higher-order M-QAM channels to be transmitted with commodity IM/DD optoelectronic hardware. Additionally, we confirmed that moving the downlink to a more spectrally efficient modulation format eliminates the impact of inter-channel crosstalk during bidirectional transmission. Finally, we demonstrated the system's operation over a wide range of launch powers from 1 dBm to 9 dBm and established its resilience to upstream impairments.

6.3 10 Gbit/s 16-QAM SCM WDM PON

In this section we present the performance of a symmetric 10 Gbit/s per wavelength 16-QAM SCM WDM PON using a bandwidth-limited RSOA-based ONU and economical IM/DD optoelectronics. In contrast to previous demonstrations in Sections 6.1 and 6.2, here we use 16-QAM signals on both the uplink and downlink to increase the net spectral efficiency up to 2.8 bit/s/Hz per channel. This enables guard bands to separate the SCM channels from surrounding noise sources. The RSOA's 2.2 GHz modulation bandwidth is spectrally pre-compensated in DSP, while offset optical filtering further enhances the chirped upstream signal at the OLT [3,9]. A new receiver DSP block is implemented to correct for timing and sampling frequency offset (SFO). This improves both the uplink BER floor and receiver sensitivity, while reducing the timing sensitivities due to signal pulse shaping. We demonstrate operation over a 20 km single feeder WDM PON and characterize the system in terms of BER performance. Furthermore, we present scenarios with both remote CW seeding and wavelength reuse of the modulated downlink signal. We then demonstrate symmetric operation at 5 dBm of OLT launch power and achieve a -12.5 dBm uplink receiver sensitivity, assuming standard RS(255,223) FEC codes with 12.5% overhead.

At the time of original publication, this was the first experimental demonstration of a single carrier 10 Gbit/s SCM WDM PON using a commercial RSOA with wavelength reuse and IM/DD 16-QAM transmission for both the uplink and downlink directions [10], as well as the highest reported spectral efficiency for a 10 Gbit/s SCM WDM PON [4].

6.3.1 Physical PON Architecture

Figure 6–14 illustrates the single feeder architecture we used in this investigation. The OLT transmitter consists of a Micram VEGA II DAC with 6 bit precision driving an EML centred at 1549.41 nm. Following the EML, a booster EDFA and a VOA control the launch power P_{OLT_Tx} , as measured at the circulator's port 2 output. The downlink ER is set with a bias-tee to achieve a minimum BER. The ODN with 9.2 dB losses comprises a 20.35 km feeder of standard single mode fiber (SMF-28e+), a 100 GHz AWG and a 1.5 km DDF.

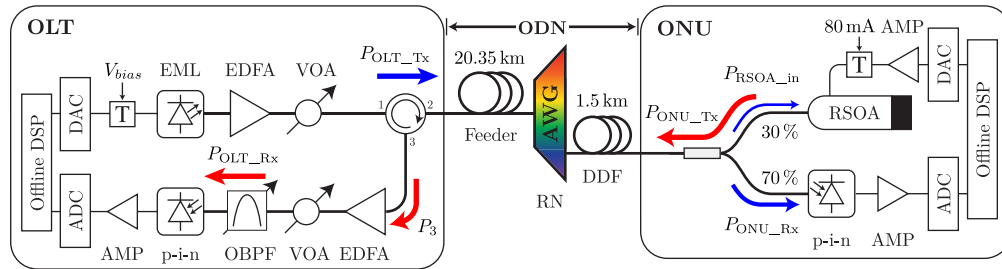


FIGURE 6–14: Physical architecture of the 16-QAM SCM WDM PON. ADC: Agilent Infiniium DSC-X 93204A, AMP: RF amplifier, AWG: arrayed waveguide grating (100 GHz channel spacing), EML: CyOptics E4560 (11 GHz bandwidth), OBPF: JDSU VCF050 (0.3 nm bandwidth), p-i-n: Discovery Semiconductors DSC-R402 (10 GHz bandwidth), RSOA: CIP SOA-RL-OEC-1550, T: RF bias-tee.

At the ONU, 70 % of the downstream signal is tapped off for detection by the receiver comprised of a p-i-n photoreceiver, a RF amplifier and a real-time oscilloscope performing 8 bit precision ADC. The remaining 30 % of the downstream signal seeds a RSOA with peak gain from 1530 nm to 1570 nm and 2.2 GHz modulation bandwidth. The RSOA uplink transmitter is directly modulated at $4 V_{p-p}$, biased at 80 mA, and is driven by a second DAC. At the OLT, an EDFA pre-amplifies the upstream signal prior to detection and a VOA sets the input power to the p-i-n, P_{OLT_Rx} . An OBPF is offset from the carrier wavelength by $\Delta\lambda = -0.18$ nm [3] to optically enhance the received signal while also emulating a second AWG for wavelength demultiplexing [60]. The OLT receiver is similar to that of the ONU consisting of a p-i-n photoreceiver, a RF amplifier and an ADC to capture the received signal.

Here we note two architectural changes compared to that in Fig. 6–1. Firstly, the ONU coupling ratio has been modified to provide 30 % of the downstream signal to the RSOA, allowing for greater gain saturation and a higher signal power to facilitate the SNR requirements for a 16-QAM uplink signal. Secondly, the OLT pre-amplifier stage is now placed before the offset

OBPF. This configuration better emulates a real-world deployment where the EDFA cost is shared among the PON's user base by simultaneously amplifying all of the upstream WDM channels prior to demultiplexing.

6.3.2 Offline DSP Framework

The transmitter DSP used in this experiment is the same as described in Section 5.2.2. A block diagram of the upgraded receiver stack is illustrated in Fig. 6–15. The data stream captured at 40 GSa/s by the ADC receiver is downsampled, RF down-converted and a matched SRRC filter removes ISI and out-of-band noise. A new block based on 2 Sa/Symbol blind feedforward symbol timing estimation [114] then corrects for timing and SFO. After the QAM decision blocks, the preamble symbols are used to remove the phase ambiguity of the PLL output. At the OLT receiver, post-compensation is optionally performed using a DFE with 12 feedforward and 1 feedback symbol-spaced taps. The DFE taps are initially trained using the preamble symbols and then dynamically adjusted using the LMS algorithm. The signal is then demodulated for BER calculation.

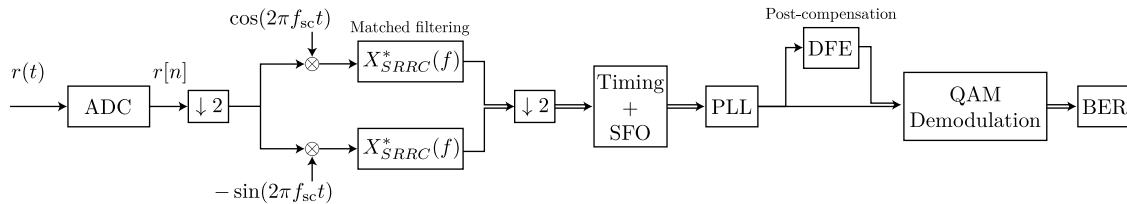


FIGURE 6–15: Block diagram of the receiver DSP stack used for offline processing the downlink and uplink 16-QAM signals. Note that DFE post-compensation is optionally performed at the OLT receiver, but is not used at the ONU to reduce complexity.

6.3.3 Downlink Performance

The downlink channel is a 2.5 Gbaud 16-QAM signal on a 7.97 GHz RF subcarrier. A 16th order FIR filter pre-compensates for the bandwidth roll-off of both the EML transmitter and the 10 GHz ONU p-i-n photoreceiver. In Fig. 6–16 we confirm the downlink channel operation by characterizing its BER performance as a function of P_{OLT_Tx} . A BER threshold of 1.1×10^{-3} is assumed for RS(255,223) FEC. Additionally, different SRRC roll-off factors α_{DL} are tested to vary the channel's bandwidth and spectral efficiency.

As the OLT launch power increases, the downlink BER quickly reaches below the FEC threshold for powers greater than 1 dBm, corresponding to a receiver sensitivity of -11 dBm. Increasing

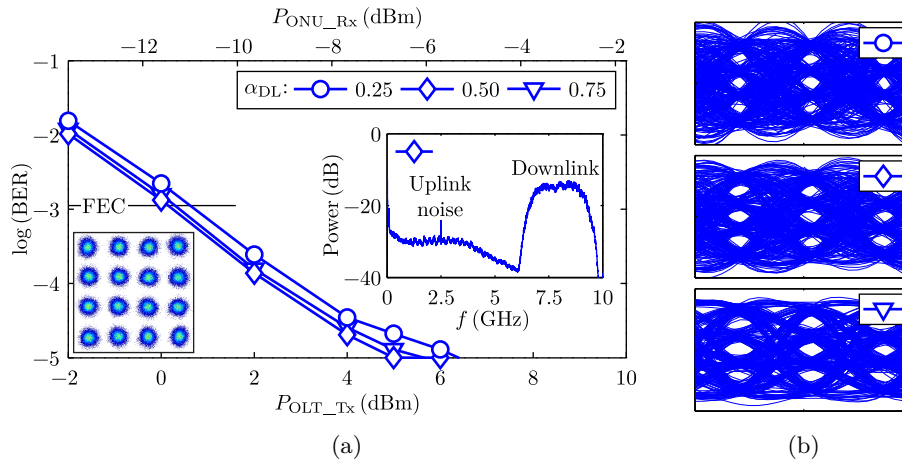


FIGURE 6–16: Performance of the 2.5 Gbaud 16-QAM downlink channel after transmission over a 20 km PON. (a) Measured BER curves for different roll-off factors. A normalized electrical power spectrum and example constellation at $P_{OLT_Tx} = 5$ dBm are inset. We note the presence of uplink channel noise from simultaneous upstream transmission. (b) Eye diagrams of the in-phase 16-QAM signal component for different α_{DL} .

the launch power beyond 5 dBm results in BERs below the 10^{-5} calculation floor. This behaviour corresponds with previous demonstrations in Section 6.2. All of the roll-off factors tested perform similarly in terms of BER and sensitivity. The highest gross spectral efficiency tested is 3.2 bit/s/Hz when $\alpha_{DL} = 0.25$, resulting in a channel bandwidth of 3.125 GHz. After accounting for the RS(255,223) FEC overhead, the information spectral efficiency decreases to 2.8 bit/s/Hz.

The eye diagrams in Fig. 6–16(b) demonstrate the effect of α_{DL} on the signal in the time domain. A larger roll-off factor broadens the pulse width in time and, in turn, increases the eye opening of the multilevel signal. A smaller α_{DL} value decreases the pulse width and the channel’s bandwidth, but leads to increased timing sensitivity at the receiver [68]. In this case, the impact of α_{DL} is minimized by adding the new timing and SFO correction block in the DSP stack.

6.3.4 Uplink Performance

The uplink channel is a 2.5 Gbaud 16-QAM signal on a 2.97 GHz RF subcarrier. A 64th order FIR filter pre-compensates for the RSOA bandwidth roll-off prior to quantization. The OLT launch power P_{OLT_Tx} was fixed at 5 dBm while characterizing the performance of the upstream transmission. As shown above in Fig. 6–16, this launch power provides an excellent downlink performance while staying below the threshold power for SBS [79]. 5 dBm is also within the range of power levels for NG-PON2 [25, 26]. This launch power corresponds to a RSOA input power

$P_{\text{RSOA_in}} = -10.7$ dBm, which is greater than the RSOA's saturation power of -17 dBm. The resulting ONU gain is ~ 12.9 dB, providing an upstream $P_{\text{ONU_Tx}} = 2.2$ dBm. After transmission through the ODN, the received power at port 3 of the circulator is measured to be $P_3 = -7.6$ dBm.

In Fig. 6–17 we present the BER performance of the 10 Gbit/s upstream transmission with both remote CW seeding and symmetric transmission with wavelength reuse from a portion of the modulated downlink signal. The impact of the uplink SRRC roll-off factor is verified for α_{UL} from 0.25 to 1.00, with resulting channel bandwidths ranging from 3.125 GHz to 5 GHz, respectively. The downlink α_{DL} was fixed at 0.50 for symmetric operation.

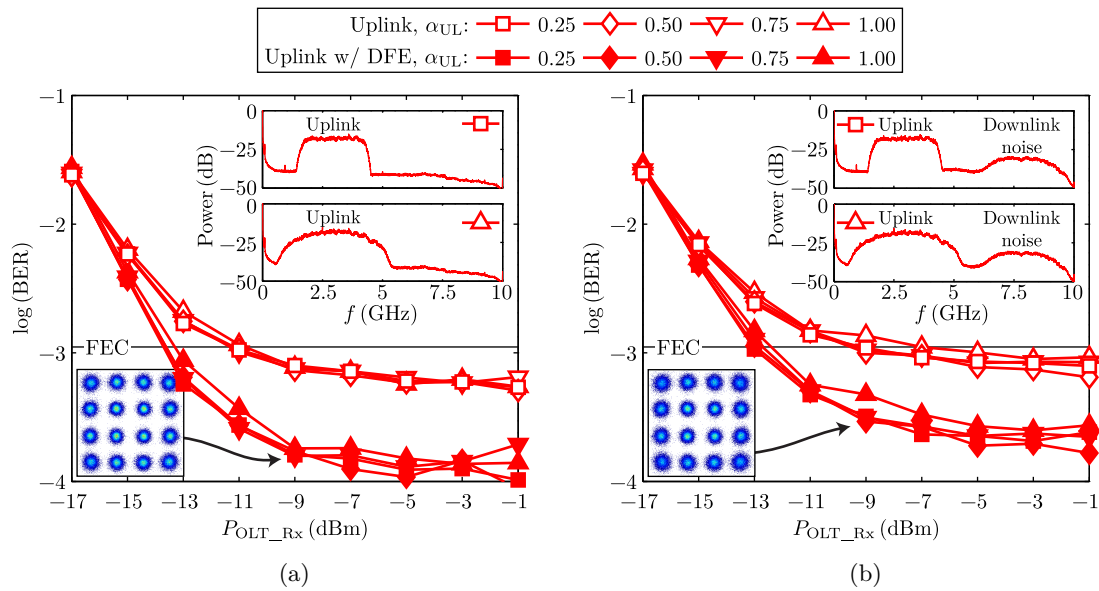


FIGURE 6–17: 16-QAM uplink channel after transmission over a 20 km PON. BER performance with (a) CW seeding and (b) full-duplex transmission. Normalized electrical power spectra and equalized constellations for $\alpha_{\text{UL}} = 0.25$ are inset.

In Fig. 6–17(a), the uplink with remote CW seeding achieves a BER below the FEC threshold at -11 dBm of received power. This represents a 2 dB improvement over our initial demonstration [10] due to the new timing and SFO correction block. The addition of a DFE stage eliminates any residual ISI and further reduces the receiver sensitivity to -13.5 dBm. In both cases the BER performance reaches a floor for received powers greater than -9 dBm due to noise limitations.

Figure 6–17(b) demonstrates the uplink performance during full-duplex transmission. As a result of reusing the modulated downlink signal, the penalty is only a $\sim 1.5\times$ increase in BER. On the other hand, the uplink receiver sensitivity degrades to -7 dBm without post-compensation, a

4 dB power penalty compared to the CW seeding case. Adding a post-compensation DFE block at the OLT receiver removes the residual ISI in the uplink signal and significantly improves the receiver sensitivity, requiring just -12.5 dBm of power to operate below the FEC threshold. In terms of power penalty, the difference between CW seeding and symmetric transmission is reduced to only 1 dB when a DFE is used at the OLT receiver. Similar to the downlink channel, the uplink performance is quite insensitive to roll-off for $\alpha_{UL} \geq 0.25$. For the remaining analysis, we will assume the use of a DFE at the OLT receiver in order to maintain BERs well below the FEC threshold.

6.3.5 Comparison With the Shannon Limit

Figure 6–18(a) is an example of the BER performance of both the downlink and uplink channels with respect to E_b/N_0 , the SNR per bit of information after the FEC overhead has been removed [50]. To calculate E_b/N_0 for each data set, the frequency domain spectrum is first calculated from the captured time domain signals. Integrating over the channel bandwidth and subtracting the average noise power from the signal results in the gross SNR per symbol, E_s/N_0 . The SNR per bit of information is then given by

$$\frac{E_b}{N_0} = \frac{E_s}{N_0} \frac{1}{\log_2(M)} \frac{n}{k}, \quad (6.1)$$

where $M = 16$ is the QAM order and $(n, k) = (255, 223)$ are the block lengths for the RS FEC coding.

The E_b/N_0 of the downlink channel increases with launch power and the BER steadily drops below the FEC threshold at $E_b/N_0 = 12.7$ dB. The uplink BER reaches below the FEC threshold at $E_b/N_0 = 12.5$ dB, but does not increase beyond 15 dB because the uplink signal power is limited by the gain saturated RSOA.

Furthermore, in Fig. 6–18(b) we can use these E_b/N_0 values to compare the performance of this 16-QAM SCM WDM PON with Shannon’s channel capacity limit [50],

$$E_b/N_0 > \frac{2^r - 1}{r} \quad (6.2)$$

where r is the channel’s spectral efficiency. Here the design trade-off between bandwidth and energy is evident, as the highest spectral efficiency requires ~ 2.2 dB greater E_b/N_0 than the lowest one.

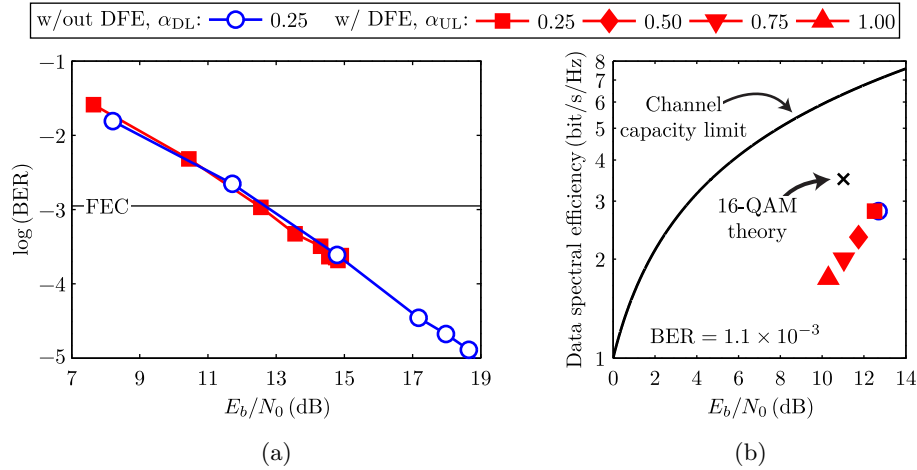


FIGURE 6–18: (a) BER vs. E_b/N_0 for the downlink and uplink channels. (b) Comparison of the 16-QAM SCM WDM PON performance with different SRRC roll-off factors to Shannon’s channel capacity limit. We also include the best theoretical 16-QAM RS(255,223) FEC coded signal to achieve the BER threshold [50]. Note that the added overhead for the RS(255,223) FEC has been taken into account for both the spectral efficiency and E_b/N_0 .

6.3.6 Discussion

This 16-QAM SCM WDM PON solution improves on previous demonstrations in Sections 6.1 and 6.2 by increasing the channels’ net spectral efficiency up to 2.8 bit/s/Hz, while still maintaining a simple wavelength reuse scheme and commodity IM/DD transceivers at both the OLT and ONU. Guard bands of up to 1 GHz ($\alpha_{UL} = 0.25$) isolate the uplink channel from surrounding noise sources, including low frequency RB beat noise [94] and inter-channel crosstalk from the downlink signal [46]. The noise can then be efficiently filtered out in DSP during the down-conversion and SRRC matched filtering stages. Notably, these improvements are achieved without any additional optical components or significant impact to the channel’s BER.

Although 2.8 bit/s/Hz is the highest net spectral efficiency achieved in this investigation, it is not necessarily the highest possible. As evident in Fig. 6–18(b), increasing the uplink channel’s spectral efficiency further would require larger E_b/N_0 . This, however, could prove difficult given that the maximum value obtained in this investigation is ~ 15 dB. Achieving a larger E_b/N_0 by increasing P_{OLT_TX} beyond 5 dBm would limit any gains because of additional RB and SBS [3]. Further reducing α also narrows the eye opening and increases the receiver’s sensitivity to timing jitter. At 10 Gbit/s data rates, $\alpha = 0.25$ provides adequate guard bands to separate the data channels from noise and crosstalk without impacting performance.

6.3.7 Conclusion

In this section we presented a 10 Gbit/s 16-QAM SCM WDM PON architecture using DSP to maximize the performance of economical IM/DD transceivers, achieving net spectral efficiencies up to 2.8 bit/s/Hz per channel. We characterized the system's performance over a 20 km single feeder PON with both remote CW seeding and full-duplex transmission scenarios and achieved BERs below the RS(255,223) FEC threshold. The pulse shaped 16-QAM channels facilitate large guard bands, providing robust resistance to upstream impairments and leading to a small 1 dB power penalty for reusing the downlink modulated signal as a seed source.

6.4 Designing a Flexible 11.25 Gbit/s SCM WDM PON

In Sections 6.1 to 6.3 we presented experimental results for three possible channel configurations of the M-QAM SCM WDM PON architecture. Comparing each of the configuration's design trade-offs from these results is difficult due to the evolution of the analysis code and variations in the ONU and OLT designs at each stage of development. In this section we use a fixed and fully optimized optical test bed and offline processing code to directly compare the performance and design trade-offs of the proposed M-QAM SCM WDM PON architecture for all permutations of QPSK and 16-QAM channel formats. The line rate of each channel is increased to 11.25 Gbit/s to account for the 12.5% overhead of the RS(255,223) FEC encoding and provide a truly symmetric 10 Gbit/s payload. The architecture's flexibility allows the signal bandwidths to be engineered to achieve certain network quality of service requirements.

6.4.1 Physical PON Architecture

Figure 6–19 illustrates the single feeder architecture used in these experiments, which is based on that in Section 6.3. The OLT transmitter consists of a Micram VEGA II DAC with 6 bit precision driving an EML centred at 1549.41 nm. Following the EML, a booster EDFA and a VOA control the launch power $P_{\text{OLT_TX}}$, as measured at the circulator's port 2 output. The downlink ER is set with a bias-tee at -1.4 V. The ODN comprises a 20.35 km feeder of standard single mode fiber (SMF-28e+), a 100 GHz AWG and a 1.5 km DDF.

Based on the results in Section 6.3, we select a 70/30 coupling ratio for the ONU to facilitate sending 16-QAM uplink channels. The coupler taps off 70% of the downstream signal for detection by the receiver comprised of a p-i-n photoreceiver, a RF amplifier and a real-time oscilloscope performing 8 bit precision ADC. The remaining 30% of the downstream signal seeds a RSOA uplink

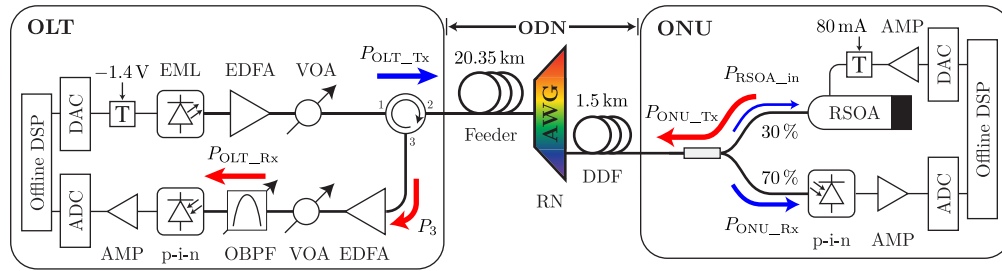


FIGURE 6–19: Physical architecture of the optimized M-QAM SCM WDM PON. ADC: Agilent Infiniium DSC-X 93204A, AMP: RF amplifier, AWG: arrayed waveguide grating (100 GHz channel spacing), EML: CyOptics E4560 (11 GHz bandwidth), OBPF: JDSU VCF050 (0.3 nm bandwidth, $\Delta\lambda = -0.27$ nm), p-i-n: Discovery Semiconductors DSC-R402 (10 GHz bandwidth), RSOA: CIP SOA-RL-OEC-1550, T: RF bias-tee.

transmitter which is directly modulated at $4V_{p-p}$, biased at 80 mA and driven by a second DAC. At the OLT, an EDFA pre-amplifies the upstream signal prior to detection and a VOA sets the input power to the p-i-n, P_{OLT_Rx} . An OBPF is offset from the carrier wavelength by -0.27 nm to optically enhance the received signal while also emulating a second AWG for wavelength demultiplexing. According to Fig. 6–11, this wavelength offset should provide an optimized enhancement for the uplink channel. The OLT receiver is similar to that of the ONU, consisting of a p-i-n photoreceiver, a RF amplifier and an ADC to capture the received signal.

6.4.2 Offline DSP Framework

To facilitate increasing the line rate to 11.25 Gbit/s, we modified the offline analysis software to support transmitting and receiving M-QAM signals at non-integer-per-symbol sampling rates. Figure 6–20 details the transmitter and receiver DSP blocks. In Fig. 6–20(a), the transmitters first generate PRBSs of length $2^{23} - 1$ and $2^{31} - 1$ for the downlink and uplink channels and add a short 1 kSymbol preamble to the beginning data frame. A SRRC pulse shaping filter is then applied to increase the spectral efficiency and reduce the ISI. Each phase component is then upsampled and mixed with an orthogonal subcarrier. The FIR pre-emphasis filters, shown in Fig. 6–20(c), compensate for the bandwidth limiting components and provide a flat modulation response over the band of interest. An amplitude clipping stage then reduces the signal’s peak-to-average power ratio (PAPR) by clipping the output above a certain threshold. The final signal is then quantized to 6 bit precision and transferred to the DAC for transmission. The DAC was operated at 24 GSa/s regardless of the baud rate and M-QAM order to ensure sampling beyond the Nyquist rate for all scenarios.

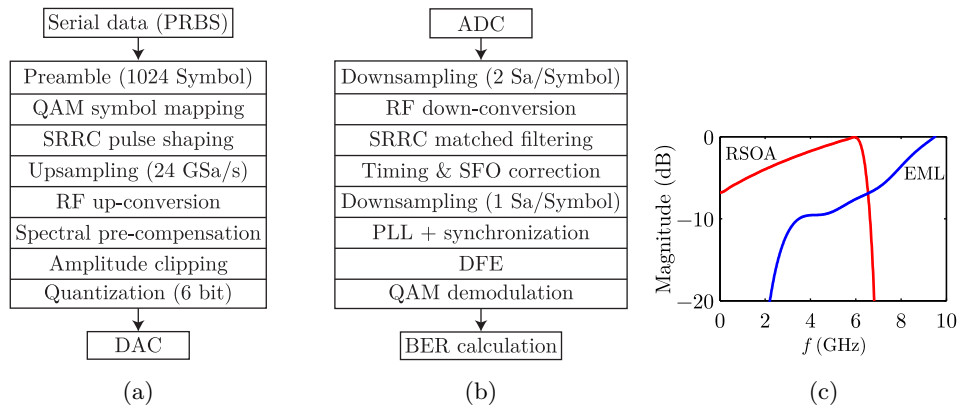


FIGURE 6–20: DSP stacks of the (a) transmitter and (b) receiver. (c) The magnitude response of the spectral pre-compensation filters applied at the OLT and ONU transmitters.

At the receiver, the data stream captured at 40 GSa/s by the ADC is downsampled, RF down-converted and matched filtered. A 2 Sa/Symbol blind feedforward symbol timing estimation block [114] then corrects for timing and SFO. After the QAM decision blocks, the preamble symbols are used to remove the phase ambiguity of the PLL output. To ensure the best BER performance of each configuration, a *mandatory* DFE with 12 forward and 1 backward symbol-spaced taps compensates for any residual ISI that remains after matched filtering. The DFE taps are trained with the 1kSymbol preamble and then dynamically adjusted using the LMS algorithm. After equalization the signal is then demodulated for BER calculation.

6.4.3 Optimizing the Operating Parameters

While the optical architecture of the PON remains fixed, we characterize the parameters in the driving electronics and DSP analysis software to find the optimal operating points. Due to the flexibility of the guard bands, we also optimize the DAC clipping ratio, SRRC roll-off factor and uplink subcarrier frequency for 16-QAM channels. When QPSK is used, the channels' operating parameters are primarily selected to minimize the channel bandwidth and spectral overlap.

DAC Clipping Ratio

The PAPR at the transmitter is determined by a combination of the QAM order, shape of the constellation signal space and the pulse shaping filter. In systems using SRRC pulse shaping, the PAPR increases with reduced excess bandwidth (smaller α) and increased filter length [115]. This becomes increasingly important because the DACs that drive the optical transmitters have a

6 bit resolution, and so if the generated signal has a high PAPR the resolution of the information carrying transitions will become distorted.

In this optimized architecture we introduce a simple function to clip the output of high level pulses beyond a certain threshold prior to quantization. This is a technique commonly used in multicarrier systems, such as orthogonal frequency-division multiplexing, to reduce PAPR [116,117]. The clipped M-QAM SCM signal is represented as

$$x_n = \begin{cases} A_{\max} & \text{if } x > A_{\max} \\ -A_{\max} & \text{if } x < -A_{\max} \\ x & \text{otherwise,} \end{cases} \quad (6.3)$$

where A_{\max} is the maximum amplitude of the signal. The severity of clipping is measured by the clipping ratio, defined as [116]

$$\gamma = \frac{A_{\max}}{\sqrt{\mathcal{P}_x}}, \quad (6.4)$$

where the average power of the discrete time signal after pre-compensation is

$$\mathcal{P}_x = \frac{1}{N} \sum_{n=0}^{N-1} |x_n|^2. \quad (6.5)$$

In Fig. 6–21 we characterize the effect of clipping ratio on the full-duplex BER performance of each transmission channel. In this example both channels are 16-QAM with a 0.05 roll-off to emphasize the effects of PAPR. The launch power $P_{\text{OLT_Tx}} = 5$ dBm ensures a balanced operating point for both channels and the received uplink power $P_{\text{OLT_Rx}}$ is fixed at -5 dBm to negate the receiver sensitivity. The RF subcarriers $f_{\text{DL}} = 7.5$ GHz and $f_{\text{UL}} = 3.0$ GHz separate the channels to suppress inter-channel crosstalk effects.

For the downlink channel, a small BER improvement is found for $\gamma_{\text{DL}} \sim 9.5$ dB. At higher γ_{DL} the peaks fall below the threshold level and little clipping occurs, and at lower levels the performance degrades due to excess signal distortion. The improvement for the uplink is more pronounced at $\gamma_{\text{UL}} = 8$ dB where the BER is reduced by a factor of $\sim 2.5\times$. Repeating these measurements for roll-off factors from 0.05 to 0.75 consistently results in $\gamma_{\text{DL}} = 9$ dB and $\gamma_{\text{UL}} = 8$ dB as the optimized values.

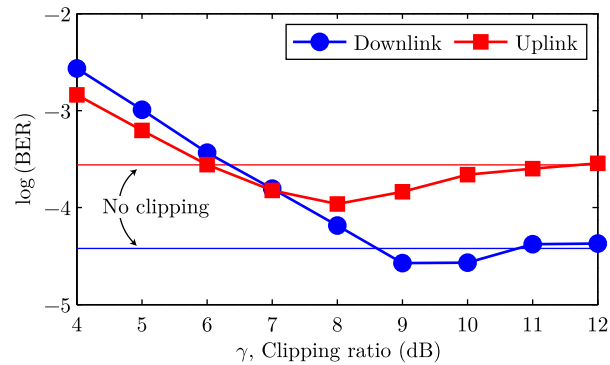


FIGURE 6–21: Optimizing the clipping ratio for 16-QAM downlink and uplink transmissions. The solid lines indicate the channel’s performance without any signal clipping.

Pulse Shaping Roll-Off Factor

Increasing the line rate to 11.25 Gbit/s makes it necessary to further investigate the effect of α on the system’s performance. In Section 6.3 we noted that decreasing the SRRC roll-off reduces the excess channel bandwidth but increases the receiver sensitivity due to shorter pulse duration in the time domain. In Fig. 6–22 we characterize the effect of α on the downlink and uplink channels’ receiver sensitivity with both CW seeding and full-duplex operation. As above, $P_{OLT_Tx} = 5$ dBm and $P_{OLT_Rx} = -5$ dBm are fixed to ensure balanced operation of both channels, and the subcarriers $f_{DL} = 7.5$ GHz and $f_{UL} = 3.0$ GHz minimize the impact of inter-channel crosstalk effects.

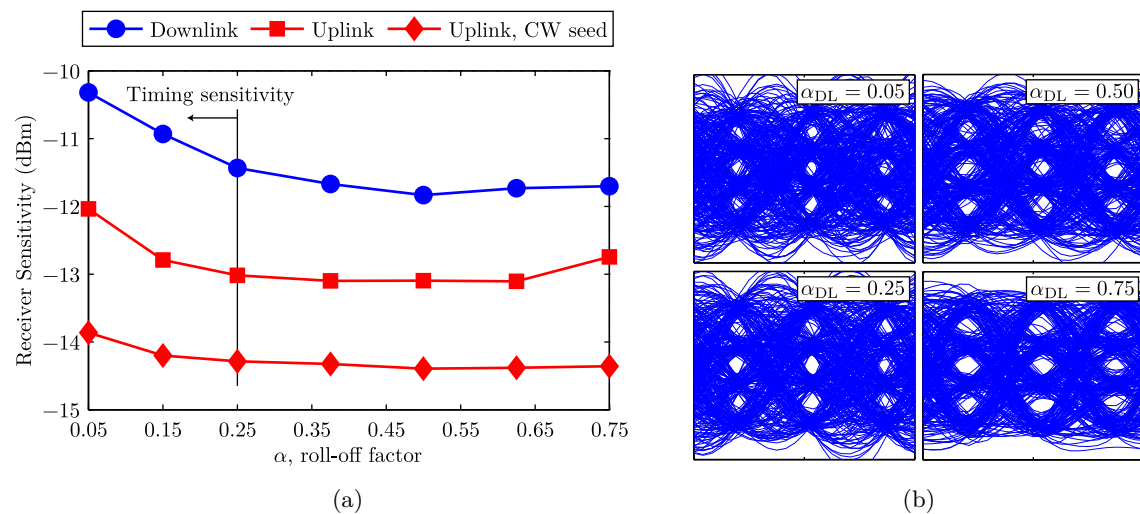


FIGURE 6–22: Optimizing the SRRC roll-off factor for 16-QAM transmission channels. (a) Receiver sensitivity during symmetric transmission and CW seeding. A BER threshold of 1.1×10^{-3} is assumed for RS(255,223) FEC. (b) Example eye diagrams of the downlink channel’s in-phase components.

In Fig. 6–22(a) we see that the behaviour for both channels is similar in terms of the receiver sensitivity, which remains constant at $\alpha \geq 0.25$. When $\alpha < 0.25$ the performance begins to degrade as the added timing sensitivity from the short pulse duration closes the eye, as clearly demonstrated in Fig. 6–22(b). The uplink channel’s sensitivity suffers a 1.5 dB to 2 dB penalty due to added noise from symmetric transmission. These results are consistent with those presented in Section 6.3.

Uplink Subcarrier Frequency

The bandwidth allocated to the uplink channel is determined by three main factors: 1) the RSOA modulation bandwidth; 2) the low frequency OBI due to RB; and 3) the inter-channel crosstalk from the downlink channel. We demonstrated previously that combining spectral pre-compensation at the transmitter and offset optical filtering at the receiver flattens the uplink channel’s frequency response over a span from 0 GHz to 6 GHz. This effectively removes the impact of the RSOA’s bandwidth over this range. In Fig. 6–23 we characterize the f_{UL} operating range of a 16-QAM uplink channel within this span as governed by the OBI and inter-channel crosstalk. The downlink 16-QAM channel is transmitted at 5 dBm on a 7.5 GHz subcarrier and both channels’ roll-off factors are 0.25.

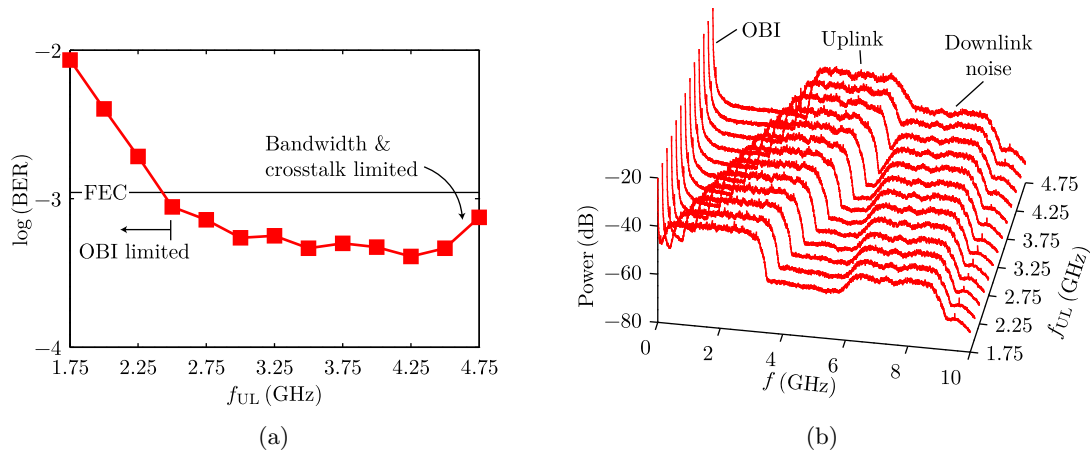


FIGURE 6–23: Characterizing the effect of uplink subcarrier frequency. (a) Uplink channel BER as a function of the RF subcarrier frequency. (b) Evolution of the upstream electrical power spectrum while sweeping f_{UL} .

Figure 6–23(a) shows the BER of the uplink channel as a function of f_{UL} during full-duplex operation. At $f_{UL} = 1.75$ GHz, the left boundary of the channel is adjacent to 0 GHz and the BER is limited to 10^{-2} by the OBI. As f_{UL} increases, the BER steadily improves and falls below

the FEC threshold at 2.5 GHz. Figure 6–23(b) illustrates the progression of the uplink channel’s power spectrum for the corresponding f_{UL} frequencies. It is evident from the spectrum that at this frequency the lower edge of the uplink channel is no longer overlapping with the low frequency RB beat noise. The uplink BER remains constant up to $f_{UL} = 4.25$ GHz where the upper edge of the channel approaches the 6 GHz boundary. Beyond this, the channel BER becomes limited by both the pre-compensation filter and crosstalk from the downlink channel.

6.4.4 Comparing M-QAM Channel Configurations

In this section we will use the optimized physical PON architecture and DSP framework described above in Sections 6.4.1 and 6.4.2 to compare the BER performance of the four possible channel combinations of QPSK and 16-QAM. The operating parameters for each scenario are listed in Table 6–1. Measured electrical spectra of each scenario can also be found in Appendix A.4.

Figure 6–24 presents the full-duplex performance of the downlink and uplink channels for each configuration over a 20 km single feeder PON. In Fig. 6–24(a) we characterize the downlink BER as a function of P_{OLT_Tx} and P_{ONU_Rx} . In all four cases the BER steadily improves with added launch power, dropping below the RS(255,223) FEC threshold at $P_{OLT_Tx} \geq 2$ dBm which is well below our target 5 dBm launch power. This behaviour is consistent with previous results where the downlink is primarily power limited rather than noise limited. These launch powers correspond to ONU receiver sensitivities between -13 dBm to -11 dBm. It is important to note that we reduce the DAC swing voltage from 900 mV_{p-p} to 400 mV_{p-p} when the downlink uses QPSK (Scenarios I and IV). This has two effects: 1) it minimizes the inter-channel crosstalk on the upstream channel due to spectral overlap; and 2) it effectively reduces the QPSK signal’s E_b/N_0 to achieve a similar downlink BER performance when compared to the 16-QAM configurations.

In Fig. 6–24(b) we present the BER performance of the uplink channel as a function of P_{OLT_Rx} . The OLT launch power is fixed at 5 dBm and a VOA adjusts the upstream received power after optical pre-amplification. Here we see that although all cases achieve BERs below the FEC threshold, the performance of the uplink channel depends on the modulation format. When the uplink is transmitted in QPSK (Scenarios I and II) the BER quickly drops below the 10^{-5} calculation threshold. However when the uplink is 16-QAM (Scenarios III and IV), the BER reaches an error floor at 10^{-4} as the SNR reaches a plateau.

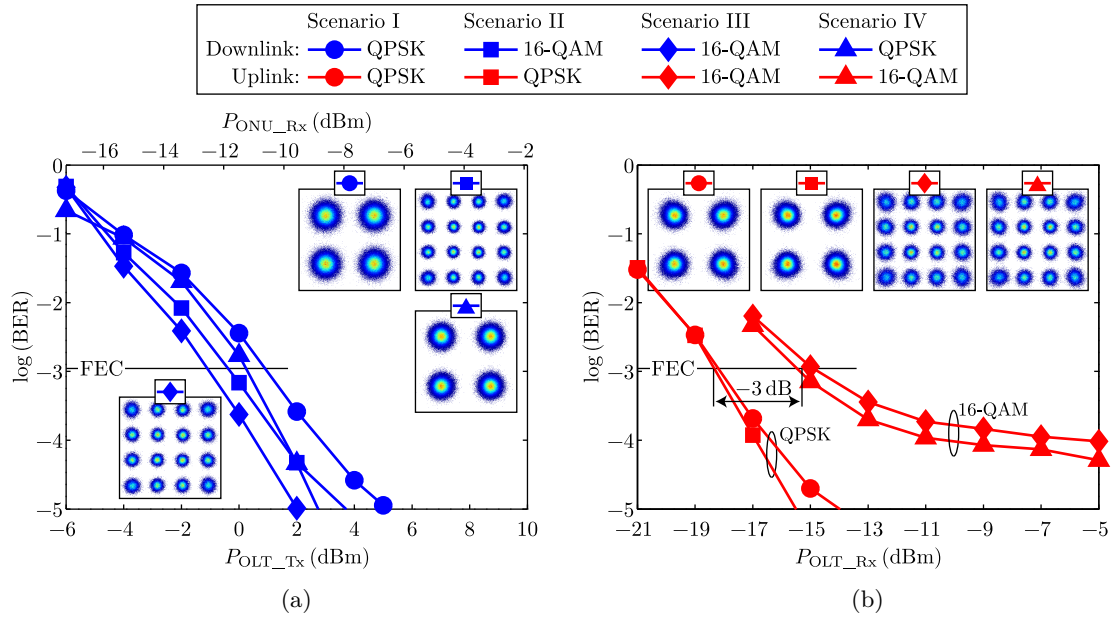


FIGURE 6-24: BER performance of the (a) downlink and (b) uplink channels for scenarios with different modulation formats. Example constellations are inset at $P_{OLT_Tx} = 5$ dBm and $P_{OLT_Rx} = -11$ dBm.

6.4.5 Discussion

The performance results in Fig. 6-24 demonstrate the 10 Gbit/s M-QAM SCM WDM PON as a truly flexible solution that meets the bandwidth demands of next-generation optical access networks. Using standard DSP techniques and DACs to generate the waveforms, we can produce four different transmission scenarios without any changes to the optoelectronics or ODN. This flexibility to select the modulation format, pulse shaping and spectral efficiency enables the network operator to implement a solution to best meet their service requirements.

The two QPSK channels in Scenario I provide the lowest receiver requirements for both the OLT and ONU, but is the least flexible solution in terms of channel allocation because even with very aggressive pulse shaping ($\alpha = 0.05$) the two channels still overlap by more than 2 GHz. With such a large overlap the uplink channel becomes susceptible to inter-channel crosstalk effects and its performance will be dependent on the downlink transmission parameters.

In Scenario II, transitioning the downlink channel to 16-QAM separates the channels with a small 0.19 GHz guard band to eliminate the inter-channel crosstalk. This configuration provides the best balance of performance and tolerance to upstream impairments by effectively making the

uplink performance independent of the downlink ER, while maintaining a QPSK uplink ensures that both channels can operate with BERs below 10^{-5} at $P_{\text{OLT_Tx}} = 5$ dBm.

With two SRRC pulse shaped 16-QAM channels, Scenario III provides the highest net spectral efficiency of the four configurations. The large 1 GHz guard bands isolate the channels from the surrounding noise sources, while also providing ample bandwidth for RF overlays. The main drawback is a 3 dB penalty in OLT receiver sensitivity as compared to QPSK.

Scenario IV simplifies the ONU receiver requirements by using a downlink QPSK channel while the uplink 16-QAM minimizes the spectral overlap. This scenario is likely the least practical for deployment. From the previous results in Chapters 3 and 4 we know that the downlink does not suffer from the same severity of crosstalk and bidirectional impairments as the uplink channel. In this sense it is counterintuitive to favour the downlink performance over that of the uplink.

6.5 Summary

This chapter experimentally demonstrated the M-QAM SCM WDM PON architecture's performance characteristics at data rates of 10 Gbit/s and beyond. Sections 6.1 to 6.3 show the evolution of the architecture's development with three proposed uplink/downlink channel configurations at 10 Gbit/s line rates: 1) QPSK/QPSK; 2) QPSK/16-QAM; and 3) 16-QAM/16-QAM. DSP spectral pre-compensation was verified to enable the transmission of higher-order modulation signals with commodity IM/DD optoelectronics. Furthermore, we demonstrated the uplink channel's resilience to upstream impairments such as RB, reflections and SBS. In each case we experimentally characterized the system's full-duplex operation over a 20 km single feeder WDM PON. In Section 6.4 we demonstrated the architecture's flexibility to meet network operators' quality of service requirements by directly comparing the performance and design trade-offs all permutations of QPSK and 16-QAM channel formats using a fixed optical test bed and optimized offline processing code. The channels' line rate was increased to 11.25 Gbit/s to account for the 12.5% overhead of the RS(255,223) FEC encoding, providing a truly symmetric 10 Gbit/s payload.

Acknowledgements

The author would also like to acknowledge Mr. Mohamed H. Morsy-Osman for suggesting and providing the base code to implement the timing and SFO correction algorithm in Section 6.3.

CHAPTER 7

Conclusions

OPTICAL ACCESS NETWORKS show great potential to meet the growing bandwidth demands of consumers, by migrating existing legacy networks to fiber optics. The high bandwidth capacity and low loss of optical fiber make it a near future-proof technology. That said, current FTTH technologies based on TDM will be difficult to scale beyond 10 Gbit/s of aggregate bandwidth. WDM PONs that leverage technologies developed for transport level networks are a leading candidate for next-generation access networks, but solutions must be engineered within the economic constraints of the industry. The research presented in this thesis aims to show the viability of WDM PONs using a single feeder architecture with colourless RSOA-based ONUs as a potential solution. We demonstrated that SCM can be an effective technique to overcome the impairments due to bidirectional transmission, and that 10 Gbit/s per wavelength symmetric transmission rates can be achieved using spectrally efficient QAM channels and commercial IM/DD transceivers.

7.1 Overview

In Chapter 1, we introduced optical access networks as a leading candidate technology to meet consumers' future bandwidth demands. We thoroughly reviewed the state of the art from the literature and presented WDM PONs as a possible solution for next-generation access networks. We then further detailed the key technical challenges that must be addressed for its commercial viability.

Chapter 2 outlined a collaborative project with industry partner Bell Canada to develop a bandwidth provisioning tool for their deployed GPON network. We implemented a Gaussian bandwidth distribution model from the literature and built a numerical software tool to estimate the capacity of the TDM PON's aggregate uplink connection using simple empirical inputs.

In Chapter 3 we proposed a novel O-SCM WDM PON architecture to increase the symmetric data rates in WDM PONs with bidirectional transmission and RSOA-based ONUs. We demonstrated that allowing some spectral overlap between the RF channels improves the bandwidth utilization efficiency at the expense of an acceptable increase in noise and inter-channel crosstalk. We experimentally demonstrated 1.5 Gbit/s full-duplex transmission over a 20 km bidirectional WDM PON and achieved BERs below 10^{-10} . We then analytically derived the system's optical power budget and looked at operating constraints due to the RSOA modulation bandwidth and the RF mixers. We further refined the O-SCM architecture and replaced the OLT's external modulator with a more economical integrated transmitter. We experimentally optimized the system's optical power budget and experimentally demonstrated 2.5 Gbit/s full-duplex transmission with BERs below 10^{-10} . Furthermore, we built a proof-of-concept O-SCM WDM PON with a stand-alone BM receiver at the OLT to perform clock and data recovery, instantaneous phase acquisition and RF down-conversion of the 2.5 Gbit/s uplink channel.

Chapter 4 presented a 5 Gbit/s O-SCM WDM PON architecture with an improved RF channel allocation scheme. We developed a DSP-based offline analysis framework to electronically equalize the upstream signal and remove the ISI that results from the bandwidth-limited RSOA transmitter. Full-duplex operation was achieved over a 20 km single feeder PON and we characterized the system's BER performance.

Chapter 5 provided an introduction to higher-order QAM and pulse shaping with IM/DD optoelectronics. We proceeded to outline the key building blocks of the 10 Gbit/s M-QAM SCM WDM PON architecture including the development of new offline transmitter and receiver DSP stacks, spectral pre-compensation, offset optical filtering and a characterization of the upstream impairments.

Chapter 6 described a series of transmission experiments with the M-QAM SCM WDM PON architecture developed in Chapter 5 at data rates of 10 Gbit/s and beyond. We initially proposed three uplink/downlink channel configurations: 1) QPSK/QPSK; 2) QPSK/16-QAM; and 3) 16-QAM/16-QAM. In each case we experimentally characterized the system's full-duplex operation over a 20 km single feeder WDM PON. The efficacy of DSP spectral pre-compensation was verified and we demonstrated the uplink channel's resilience to upstream impairments such as RB, reflections and SBS. We then further optimized the ODN and operating parameters to increase the channel line rates to 11.25 Gbit/s, accounting for the 12.5% RS(255,223) FEC coding overhead.

We then established the architecture's flexibility by directly comparing the BER performance of all permutations of QPSK and 16-QAM channels on a fixed optical test bed while providing a truly symmetric 10 Gbit/s payload.

7.2 Summary of Contributions

In this section we summarize the original contributions to the optical access network research field. The contributions listed here are all novel and have not been demonstrated previously in the literature. As evidence of our original contributions, the investigations presented in this thesis have resulted in ten peer-reviewed publications, including four journal articles [1–4] and six conference proceedings [5–10], including one invited conference paper [6].

7.2.1 Overlapped-Subcarrier Multiplexed WDM PONs

We proposed the concept of an O-SCM WDM PON to relax the channel separation requirements in a bidirectional system and improve the bandwidth efficiency of the RSOA-based ONU [5]. We experimentally demonstrated 1.5 Gbit/s full-duplex transmission with BERs below 10^{-10} without the aid of electronic equalization or FEC coding. At the time of publication we reported the highest symmetric bit rate for a bidirectional SCM WDM PON with NRZ line coding, downstream remodulation and a RSOA-based ONU.

We then further refined and optimized the O-SCM WDM PON's design and experimentally demonstrated 2.5 Gbit/s full-duplex transmission with BERs below 10^{-10} using an integrated commercial EML transmitter at the OLT [1]. We also demonstrated operation with a stand-alone BM receiver at the OLT to perform clock and data recovery, instantaneous phase acquisition and RF down-conversion of the 2.5 Gbit/s uplink channel [8].

7.2.2 Electronically Equalized Overlapped-Subcarrier Multiplexed WDM PONs

We proposed a second generation O-SCM architecture to minimize the impact of the RSOA modulation bandwidth by modifying the RF channel allocation. We then designed and implemented an offline analysis and DSP framework to electronically equalize the uplink signal with a DFE to increase symmetric bit rates [7]. Combining electronic equalization and FEC further reduced the minimum optical launch power required to achieve full-duplex operation. We built an optical test bed to achieve full-duplex 5 Gbit/s operation with BERs below the desired FEC coding threshold [2].

At the time of publication we established the lowest reported minimum launch power for a SCM WDM PON operating at 5 Gbit/s.

7.2.3 Pulse Shaped M-QAM Subcarrier Multiplexed WDM PONs

We proposed a third generation SCM WDM PON architecture implementing higher-order QAM signals and DSP to achieve symmetric 10 Gbit/s transmission over a 20 km bidirectional PON. We developed an offline DSP analysis framework, featuring spectral pre-compensation to linearize the modulation response of the IM/DD optoelectronic transceivers, and SRRC pulse shaping to increase the spectral efficiency of the RF channels. Combined with optical offset filtering of the upstream signal, these facilitated 10 Gbit/s full-duplex transmission in 10 GHz of electrical bandwidth. We built optical test beds to experimentally verify the system's operation and characterized its BER performance for different modulation formats. We further demonstrated a resilience to upstream impairments and characterized the impact of system parameters such as pulse shaping roll-off factor, subcarrier frequency and QAM order. We reported: 1) the first demonstration of a single carrier 10 Gbit/s SCM WDM PON with wavelength reuse, a commercial RSOA and 10 GHz IM/DD transceivers [3]; 2) the highest symmetric bit rate for a WDM PON with wavelength reuse and IM/DD QPSK transmission for both the uplink and downlink directions [9]; 3) the first demonstration of a single carrier 10 Gbit/s 16-QAM SCM WDM PON using a commercial RSOA with wavelength reuse and IM/DD [10]; and 4) the highest net spectral efficiency for a 10 Gbit/s SCM WDM PON [4].

7.3 Future Research

Although the research objectives of this thesis have been realized, a number of interesting avenues are still to be explored. In this section we briefly highlight two research directions that will be important for the future of WDM PONs.

7.3.1 DSP-Enabled PONs

Advancements in high-speed DACs, ADCs and DSP techniques have revolutionized transport level networks [67,68] and much of recent FTTH and WDM PON research has focused on adapting these technologies to the access network space. Techniques such as pulse shaping, higher-order modulation and electronic equalization can improve spectral efficiency, extend reach, mitigate impairments and provide flexible resource allocation to customers [118]. DSP can similarly reduce

hardware costs by extending the performance of low cost commercial optoelectronics. In this thesis we demonstrated the viability of these techniques with RSOA and EML transmitters, but the potential applications for future architectures and devices are vast.

7.3.2 Low-Cost Tunable Lasers for WDM PON

The development and commercialization of low-cost and widely tunable laser sources for access networks would eliminate the noise and reach restrictions of RSOA-based approaches and revolutionize WDM PONs. Tunable sources have already been selected as the transmitter for NG-PON2, but their required wavelength range is limited to only a few channels. This makes the current generation of devices inappropriate for next-generation WDM PONs which would likely require broad tunability over the optical C-band. Research in this area is ongoing and offers great opportunities for advancements in WDM PONs.

7.4 Final Thoughts

Although WDM PONs are an attractive technology for future optical access networks, their adoption primarily hinges on the availability of economical and colourless transceivers. This thesis successfully demonstrated that SCM WDM PONs with colourless RSOA-based ONUs are a viable solution to achieve the projected 10 Gbit/s per wavelength data rates of next-generation optical access networks. Additionally, we showed that combining DSP techniques and spectrally efficient QAM data channels can enhance the performance of low cost IM/DD transceivers while simultaneously mitigating the bidirectional impairments of the single feeder PON architecture. In all, these provide network operators with a flexible solution to meet the future demands of their customers.

APPENDIX A

Further Details

A.1 Optical Signal to Rayleigh Backscattering Ratio

The two major RB contributors in the received uplink signal have optical power,

$$\begin{aligned} P_{\text{DLRB}} &= P_{\text{OLT_Tx}} \cdot \frac{\alpha_s \mathcal{S}}{2\alpha} (1 - e^{-2\alpha L}) \\ &= P_{\text{OLT_Tx}} \cdot \zeta_{\text{DL}} \end{aligned} \quad (\text{A.1})$$

$$\begin{aligned} P_{\text{ULRB}} &= P_{\text{ONU_Tx}} \cdot \frac{\alpha_s \mathcal{S}}{2\alpha} (1 - e^{-2\alpha L}) \cdot g_{\text{ONU}} \cdot e^{-\alpha L} \\ &= P_{\text{ONU_Tx}} \cdot \zeta_{\text{UL}} \cdot g_{\text{ONU}} \cdot l, \end{aligned} \quad (\text{A.2})$$

where α_s is the fiber scattering coefficient, \mathcal{S} is the fiber scattering recapture factor [83], g_{ONU} is the gain of the ONU transmitter (including coupling losses) and $l = e^{-\alpha L}$ is the total loss for a single trip through a fiber of length L with attenuation constant α . We can now define the OSRBR for the received uplink signal [79, 84] as

$$\begin{aligned} \text{OSRBR}_{\text{UL}} &= \frac{P_{\text{ONU_Tx}} \cdot l}{P_{\text{DLRB}} + P_{\text{ULRB}}} \\ &= \frac{P_{\text{ONU_Tx}} \cdot l}{P_{\text{OLT_Tx}} \cdot \zeta_{\text{DL}} + P_{\text{ONU_Tx}} \cdot \zeta_{\text{UL}} \cdot g_{\text{ONU}} \cdot l}. \end{aligned} \quad (\text{A.3})$$

Assuming that the ODN losses and ONU gain profile are well characterized, the uplink launch power is $P_{\text{ONU_Tx}} = P_{\text{OLT_Tx}} \cdot l \cdot g_{\text{ONU}}$, simplifying Eq. (A.3) as

$$\text{OSRBR}_{\text{UL}} = \frac{g_{\text{ONU}} \cdot l^2}{(\zeta_{\text{DL}} + \zeta_{\text{UL}} \cdot g_{\text{ONU}}^2 \cdot l^2)}. \quad (\text{A.4})$$

A similar treatment for the impact of RB on the downlink signal gives

$$\text{OSRBR}_{\text{DL}} = \frac{P_{\text{OLT_Tx}} \cdot l}{\zeta_{\text{UL}} \cdot P_{\text{ONU_Tx}}} \quad (\text{A.5})$$

$$= \frac{P_{\text{OLT_Tx}} \cdot l}{\zeta_{\text{UL}} \cdot (P_{\text{OLT_Tx}} \cdot l \cdot g_{\text{ONU}})}. \quad (\text{A.6})$$

Furthermore, for fiber lengths greater than approximately 20 km, ζ_{UL} and ζ_{DL} converge to a nearly constant value for launch powers below 7 dBm [79, 80, 84]. Therefore given $\zeta \simeq \zeta_{\text{UL}} = \zeta_{\text{DL}}$, Eqs. (A.4) and (A.6) further simplify to

$$\text{OSRBR}_{\text{UL}} \simeq \frac{g_{\text{ONU}} \cdot l^2}{\zeta (1 + g_{\text{ONU}}^2 \cdot l^2)} \quad (\text{A.7})$$

$$\text{OSRBR}_{\text{DL}} \simeq \frac{1}{\zeta \cdot g_{\text{ONU}}}, \quad (\text{A.8})$$

which are valid when $P_{\text{OLT_Tx}} < 7$ dBm and solely dependent on g_{ONU} and l [79, 84].

A.2 Principle of Subcarrier Multiplexing

Mathematically, a passband signal is produced by multiplying a baseband modulated signal $A(t)$ with a sinusoidal subcarrier frequency f_{sc} , resulting in

$$x(t) = A(t) \cos(2\pi f_{sc} t). \quad (\text{A.9})$$

Assuming an ideal transmission medium, the channel of interest is recovered from the received signal by multiplication with a sinusoidal signal of the same frequency f_{sc}

$$y(t) = x(t) \cos(2\pi f_{sc} t + \phi), \quad (\text{A.10})$$

where ϕ is a phase offset. After expanding Eq. (A.10) and simplifying, we obtain

$$y(t) = [A(t) \cos(2\pi f_{sc} t)] \cos(2\pi f_{sc} t + \phi) \quad (\text{A.11})$$

$$\begin{aligned} &= \frac{A(t)}{2} [\cos(2\pi f_{sc} t - (2\pi f_{sc} t + \phi)) + \cos(2\pi f_{sc} t + (2\pi f_{sc} t + \phi))] \\ &= \frac{A(t)}{2} \cos(-\phi) + \frac{A(t)}{2} \cos(4\pi f_{sc} t + \phi). \end{aligned} \quad (\text{A.12})$$

If the phase of the receiver's clock signal is properly tuned ($\phi = 0$), then

$$y(t) = \frac{A(t)}{2} + \frac{A(t)}{2} \cos(4\pi f_{sc} t + 0), \quad (\text{A.13})$$

where $\frac{A(t)}{2}$ is the recovered baseband signal, and the second term can be eliminated with a simple LPF.

A.3 Solving the Gaussian Bandwidth Approximation Model

We use the Newton-Raphson root finding method [119] to solve the Gaussian capacity model given in Eq. (2.7). This method is well suited for functions with a first derivative that can be determined analytically. We define a function

$$f(m) = \frac{\sigma_R}{\mu_R} \cdot (\phi(m) - m \cdot \Phi(m)) - p_{loss}, \quad (\text{A.14})$$

which has first derivative

$$f'(m) = \frac{-1}{\mu_R} \Phi(m). \quad (\text{A.15})$$

To solve for the root $f(m) = 0$, we use an initial estimate m_0 of the root. The first approximate solution is given by

$$m_1 = m_0 - \frac{f(m_0)}{f'(m_0)}.$$

We then repeat this process to find

$$m_{k+1} = m_k - \frac{f(m_k)}{f'(m_k)}.$$

until the error $\xi = |m_{k+1} - m_k|$ is sufficiently small.

A.4 Electrical Spectra for the M-QAM SCM WDM PON Scenarios

Figures A-1 to A-4 show electrical power spectra for downstream and upstream signals, as measured at the OLT and ONU receivers, respectively. These correspond to the four scenarios discussed in Section 6.4.4. The top plots demonstrate the spectral contribution of each channel by alternating single channel modulation and then decoupling their effects, and the bottom plots show the combined power spectra measured during full-duplex transmission. All measurements were performed using an electrical spectrum analyzer with 0 dBm reference level, 30 kHz resolution bandwidth and 30 kHz video bandwidth.

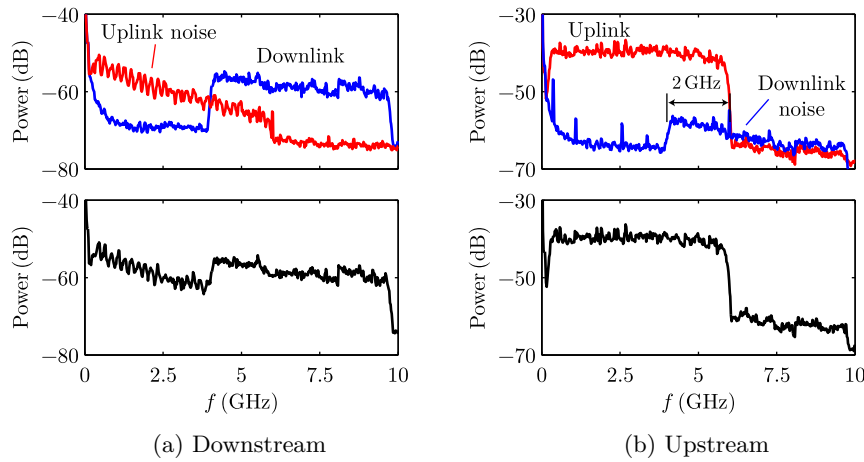


FIGURE A-1: Power spectra for Scenario #1 with QPSK downlink and uplink channels.

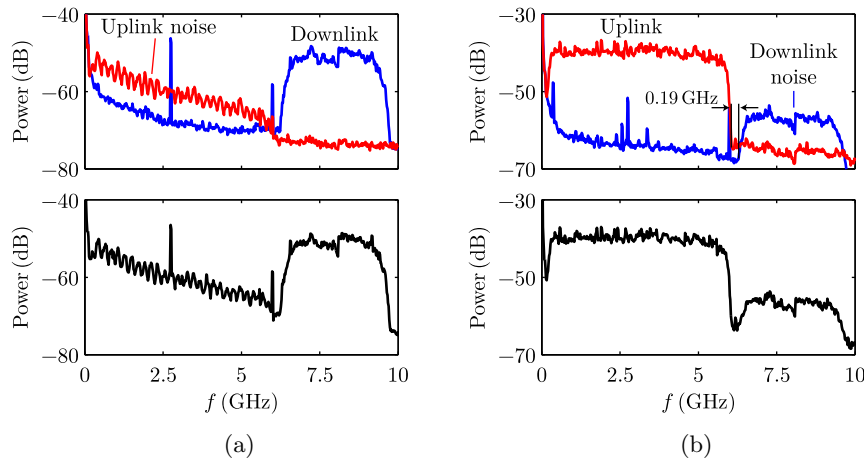


FIGURE A-2: Power spectra for Scenario #2 with 16-QAM downlink and QPSK uplink channels.

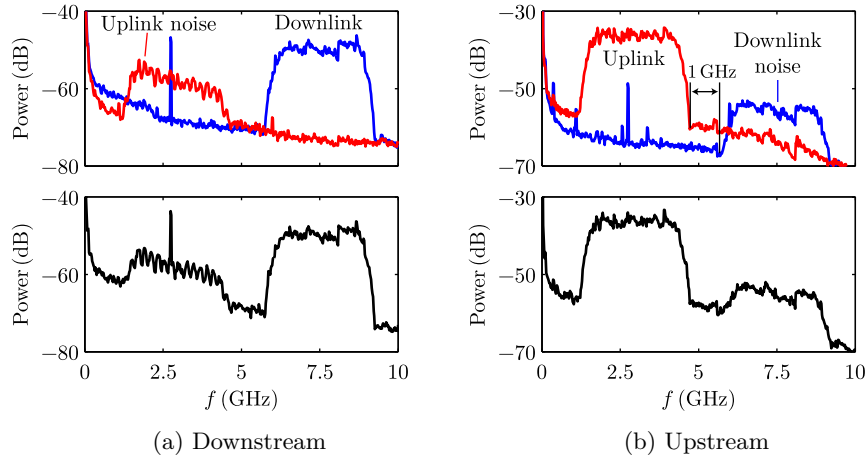


FIGURE A-3: Power spectra for Scenario #3 with 16-QAM downlink and uplink channels.

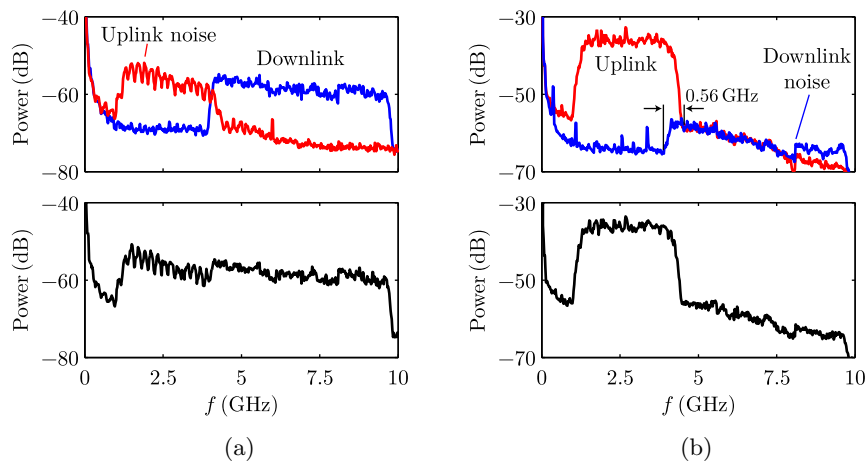


FIGURE A-4: Power spectra for Scenario #4 with QPSK downlink and 16-QAM uplink channels.

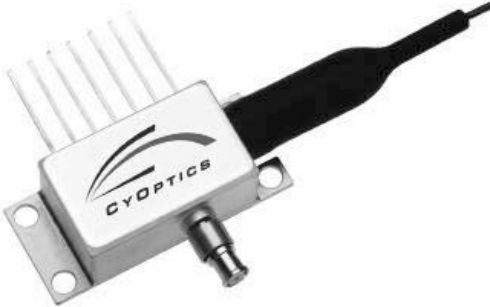
A.5 Additional Hardware Specifications

EML



Data Sheet
October 2007

E4560-Type 10 Gb/s High-Power EML Modules up to 40 km (800ps/nm) Transmission



The image shows a rectangular metal module with a GPO connector on the front and a fiber optic cable attached to the back. The CyOptics logo is visible on the front panel.

Description

The E4560-series EML is designed for 10 Gb/s DWDM or TDM transmission applications. The EML integrates a CW laser with an electroabsorptive modulator in the same semiconductor chip and are an extension of CyOptics' existing E2500-series of devices. These devices can replace external modulators that are often bulkier, more expensive, and require more drive electronics than the EML. The E4560 series use a small-profile GPO™ (SMP) connector to handle the RF signal. The package also contains a thermoelectric cooler, thermistor, rear-facet monitor photodiode, and an optical isolator.

The nominal input impedance of the E4560 version is 50 Ω. The package is qualified to the *Telcordia Technologies™* TA-TSY-000468 standard.

E4560 is available in a range of ITU-T C-band wavelengths for use in DWDM systems operating at 10 Gb/s per channel. Also, E4560-series is offered as a single-channel device operating within a wavelength range of 1530 nm—1563 nm

The devices exhibit excellent wavelength stability, supporting operation at 100 GHz channel spacing over 20 years (assuming an end-of-life aging condition of $\leq \pm 100$ pm). Typically, no external wavelength stabilization is required in systems of this type, using the CyOptics E4560 EMLs. The package also offers excellent stability of wavelength vs. case temperature, with a maximum coefficient of ± 0.5 pm/°C.

Features

- » Integrated electroabsorptive modulator
- » 1.5 μm wavelength
- » High Output Power
- » Specified for 9.95 Gb/s operation
- » For use up to 40 km (800ps/nm)
- » Low modulation voltage
- » Temperature stabilized
- » Wavelength selectable to ITU-T standards
- » Ultrastable wavelength aging for DWDM

Applications

- » SONET/SDH applications
- » Ultrahigh capacity WDM system application
- » High-speed data communication
- » Digitized video

Data Sheet
October 2007

E4560-Type 10 Gb/s EML Modules
up to 40 km (800ps/nm) Transmission

Target Specifications(continued)

Characteristics

Minimum and maximum values specified over operating case temperature range. Typical values are measured at room temperature (25°C) unless otherwise noted.

Table 4. Optical and Electrical Specifications
(Chip operating temp. = 20 °C to 35 °C, except where noted.)

Parameter	Symbol	Conditions	Min	Max	Unit
Threshold Current (BOL)	I_{TH}	—	5	35	mA
Forward Voltage	V_F	$I_F = I_{OP} @ T_{OP}$	—	2.2	V
Operating Current	I_{OP}	—	50	100	mA
Threshold Power	P_{TH}	$I_F = I_{TH}, V_M^* = 0V$	—	80	μW
Fiber Output Power (Average) , BOL	P_{AVG}	Note 1	0.5	+3.0	dBm
Fiber Output Power (Average) , EOL	P_{AVG}	Note 1	0	2.5	dBm
Peak Wavelength (Wavelength can be specified to the ITU wavelength channels. See Table 5.)	λ_{PK}	Note 1	1528	1564	nm
Side-mode Suppression Ratio	SMSR	$V_M = 0, I_F = I_{OP}, T_{OP}$	35	—	dB
Peak to Peak Modulator Voltage	V_{PP}		1.5	2.5	V
On-State Modulator Voltage	V_{ON}		-1.0	0	V
Dispersion Penalty, BER = 10^{-12} D = 800 ps/nm	DP	Notes 1,2	—	2.0	dB
Modulator					
RF Extinction Ratio	ER_{RF}	Notes 1,4	10	—	dB
RF Return Loss (0 GHz to 8 GHz)	S_{11}	$V_M = -0.8V, I_F = I_{OP}$	10	—	dB
RF Return Loss (8 GHz to 10 GHz)	S_{11}	$V_M = -0.8V, I_F = I_{OP}$	8.5	—	dB
-3 dB Bandwidth	BW	$V_M = -0.8V, I_F = I_{OP}$	11	—	GHz
Rise/Fall Time (20%—80%)	t_R/t_F	Note 4	—	40	ps
Monitor Diode					
Monitor Current	I_{BD}	$V_{BD} = 5V, I_F = I_{OP}$	40	1100	μA
Dark Current	I_D	$V_{BD} = 5V$	—	0.1	μA
Capacitance	C	$V_{BD} = 5V, F = 1MHz$	—	25	pF
Thermistor					
Resistance	R_{THERM}	$T = 25^\circ C$	9.5	10.5	k Ω
Thermistor Current	I_{TC}	—	10	100	μA
Thermistor B Constant	B	—	3700	4100	—
Thermoelectric Cooler (TEC)					
TEC Cooling Current**	I_{TEC}	Note 3	—	1.3	A
TEC Voltage	V_{TEC}	Note 3	—	2.6	V
TEC Power	P_{TEC}	Note 3	—	3.4	W
TEC Cooling Capacity	ΔT	Note 3	—	55	C
Optical Isolation					
Optical Isolation	—		30	—	dB

Mixers

Coaxial Frequency Mixer

ZX05-C42MH+

Level 13 (LO Power +13 dBm) 1000 to 4200 MHz



CASE STYLE: FL905

Maximum Ratings

Operating Temperature	-40°C to 85°C
Storage Temperature	-55°C to 100°C
RF Power	200mW
IF Current	40mA
Permanent damage may occur if any of these limits are exceeded.	

Coaxial Connections

LO	1
RF	2
IF	3

Features

- rugged construction
- small size
- low conversion loss
- high L-R isolation
- protected by US Patents 6,790,049 & 7,027,795

Applications

- cellular
- PCS
- instrumentation
- satellite communication

Connectors	Model	Price	Qty.
SMA	ZX05-C42MH-S+	\$39.95 ea.	(1-24)

+ RoHS compliant in accordance with EU Directive (2002/95/EC)

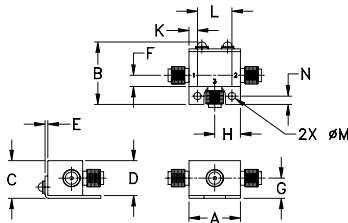
The +Suffix has been added in order to identify RoHS Compliance. See our web site for RoHS Compliance methodologies and qualifications.

Electrical Specifications (T_{AMB}=25°C)

FREQUENCY (MHz)	CONVERSION LOSS (dB)	LO-RF ISOLATION (dB)		LO-IF ISOLATION (dB)		IP3 at center band (dBm)			
		Typ.	Min.	Typ.	Min.				
1000-4200	DC-1500	6.2	0.1	8.9	35	15	20	10	16

1 dB COMP: +9 dBm typ.

Outline Drawing



Outline Dimensions (Inch/mm)

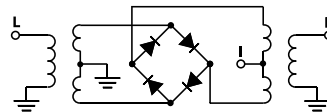
A	B	C	D	E	F	G
.74	.90	.54	.50	.04	.16	.29
18.80	22.86	13.72	12.70	1.02	4.06	7.37

H	J	K	L	M	N	wt
.37	--	.122	.496	.106	.122	grams
9.40	--	3.10	12.60	2.69	3.10	20.0

Typical Performance Data

Frequency (MHz)		Conversion Loss (dB)	Isolation L-R (dB)	Isolation L-I (dB)	VSWR RF Port (:1)	VSWR LO Port (:1)
RF	LO	LO +13dBm	LO +13dBm	LO +13dBm	LO +13dBm	LO +13dBm
1000.10	1030.11	5.54	34.65	22.99	2.57	4.54
1164.20	1194.21	5.75	42.95	25.97	3.33	3.62
1328.31	1358.32	5.65	45.06	24.23	3.36	2.88
1492.41	1522.42	5.52	41.94	21.25	3.20	2.69
1656.51	1686.52	5.86	37.88	21.97	2.96	2.79
1820.61	1850.62	5.56	39.58	20.83	2.49	2.93
1984.72	2014.73	5.74	36.47	22.17	2.29	3.21
2148.82	2178.83	5.69	35.35	22.92	2.29	3.47
2312.92	2342.93	6.00	34.88	19.04	2.64	4.03
2559.07	2589.08	6.38	40.91	18.95	2.91	6.03
2723.18	2753.19	6.54	41.04	19.81	3.33	8.33
2887.28	2917.29	6.61	43.02	19.85	3.18	6.06
3051.38	3081.39	6.05	39.81	21.17	2.88	5.33
3215.49	3245.50	6.05	36.34	21.37	3.14	5.53
3379.59	3409.60	6.11	32.23	22.06	3.12	4.32
3543.69	3573.70	6.37	29.28	22.17	3.22	3.15
3707.79	3737.80	6.65	26.88	23.67	3.50	2.83
3871.90	3901.91	7.05	24.86	25.01	3.97	3.22
4036.00	4066.01	7.51	24.53	21.27	3.87	4.02
4200.10	4170.09	7.37	24.55	18.50	3.78	5.45

Electrical Schematic



ISO 9001 ISO 14001 AS 9100 CERTIFIED

P.O. Box 350166, Brooklyn, New York 11235-0003 (718) 934-4500 Fax (718) 332-4661 The Design Engineers Search Engine Provides ACTUAL Data Instantly at minicircuits.com

RF/MICROWAVE COMPONENTS

For detailed performance specs & shopping online see web site

Notes: 1. Performance and quality attributes and conditions not expressly stated in this specification sheet are intended to be excluded and do not form a part of this specification sheet. 2. Electrical specifications and performance data contained herein are based on Mini-Circuit's applicable established test performance criteria and measurement instructions. 3. The parts covered by this specification sheet are subject to Mini-Circuit's standard limited warranty and terms and conditions (collectively, "Standard Terms"). Purchasers of this part are entitled to the rights and benefits contained therein. For a full statement of the Standard Terms and the exclusive rights and remedies thereunder, please visit Mini-Circuit's website at www.minicircuits.com/MCStore/terms.jsp.

REV. D
M108294
ZX05-C42MH
RVN1TD/CP/AM
091007
Page 1 of 2



DOUBLE-BALANCED MIXERS

M1-0208



Features

- LO/RF 2.0 to 8.0 GHz
- IF DC to 2.0 GHz
- 6.0 dB Typical Conversion Loss
- 38 dB Typical LO to RF Isolation
- Multi-Octave RF and LO

Electrical Specifications - Specifications guaranteed from -55 to +100°C, measured in a 50-Ohm system.

Parameter	LO (GHz)	RF (GHz)	IF (GHz)	Min	Typ	Max	Diode Option LO drive level (dBm)
Conversion Loss (dB)	2.0-8.0 2.0-8.0	2.0-8.0 2.0-8.0	DC-1.0 1.0-2.0		6.0 6.5	7.0 8.5	
Isolation (dB)				25			
LO-RF	2.0-8.0	2.0-8.0			38		
LO-IF	2.0-8.0	2.0-8.0			20		
RF-IF	2.0-8.0	2.0-8.0			25		
Input 1 dB Compression (dBm)	2.0-8.0	2.0-8.0			+2 +5 +8 +11 +14		L (+7 to +10) M (+10 to +13) N (+13 to +16) H (+16 to +19) S (+19 to +22)
Input Two-Tone Third Order Intercept Point (dBm)	2.0-8.0	2.0-8.0			+12 +15 +18 +21 +24		L (+7 to +10) M (+10 to +13) N (+13 to +16) H (+16 to +19) S (+19 to +22)

Part Number Options

<i>Please specify diode level and package style by adding to model number.</i>	
Package Style(s) ^{1,2}	Example
A, B, C, E, EZ, P	M1-0208 L A

¹Connectorized test fixtures available for most carrier and surface mount packages. Consult factory.

²For non-connectorized packages, specify l-port configuration by adding -1 or -2 suffix to model number. Default is -2 configuration when not specified.

Marki Microwave reserves the right to make changes to the product(s) or information contained herein without notice. Marki Microwave makes no warranty, representation or guarantee regarding the suitability of its products for any particular purpose, nor does Marki Microwave assume any liability whatsoever arising out of the use of or application of any product.

215 Vineyard Court, Morgan Hill, CA 95037 | Ph: 408.778.4200 | Fax 408.778.4300 | info@markimicrowave.com



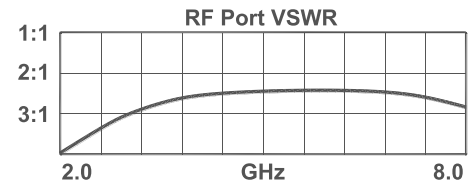
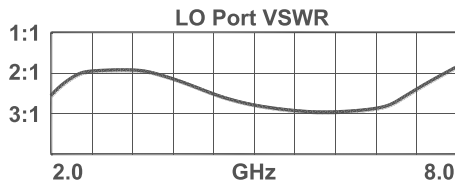
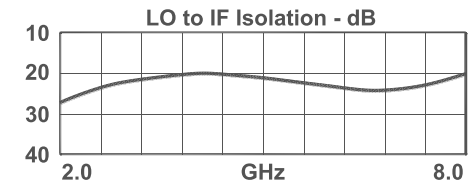
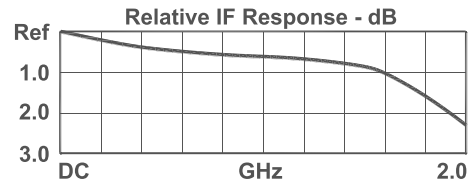
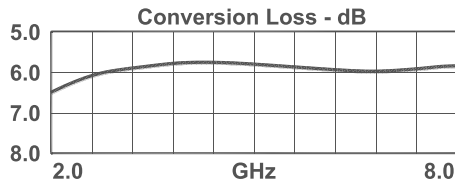
DOUBLE-BALANCED MIXERS

Page 2

M1-0208

**LO/RF 2.0 to 8.0 GHz
IF DC to 2.0 GHz**

Typical Performance



DATA SHEET NOTES:

1. Mixer Conversion Loss Plot IF frequency is 100 MHz.
2. Mixer Noise Figure typically measures within +0.5 dB of conversion loss for IF frequencies greater than 5 MHz.
3. Conversion Loss typically degrades less than 0.5 dB for LO drives 2 dB below the lowest and 3 dB above highest nominal LO drive levels.
4. Conversion Loss typically degrades less than 0.5 dB at +100°C and improves less than 0.5 dB at -55°C.
5. Maximum input power is +23 dBm at +25°C, derated linearly to +20 dBm at +100°C.
6. Specifications are subject to change without notice. Contact Marki Microwave for the most recent specifications and data sheets.
7. Standard configuration for A, B, and C outlines are with connectors and bottom spacer.
8. Catalog mixer circuits are continually improved. Configuration control requires custom mixer model numbers and specifications.

Marki Microwave reserves the right to make changes to the product(s) or information contained herein without notice. Marki Microwave makes no warranty, representation, or guarantee regarding the suitability of its products for any particular purpose, nor does Marki Microwave assume any liability whatsoever arising out of the use or application of any product.

© Marki Microwave, Inc.



215 Vineyard Court, Morgan Hill, CA 95037 | Ph: 408.778.4200 | Fax: 408.778.4300 | info@markimicrowave.com

www.markimicrowave.com



DOUBLE-BALANCED MIXERS

M1-0412



Features

- LO/RF 4.0 to 12.0 GHz
- IF DC to 4.0 GHz
- 5.0 dB Typical Conversion Loss
- 40 dB Typical LO to RF Isolation
- Very-Broadband LO and RF

Electrical Specifications - Specifications guaranteed from -55 to +100°C, measured in a 50-Ohm system.

Parameter	LO (GHz)	RF (GHz)	IF (GHz)	Min	Typ	Max	Diode Option LO drive level (dBm)
Conversion Loss (dB)	4.0-12.0	4.0-12.0	DC-1.0		5.0	7.0	
	4.0-12.0	4.0-12.0	1.0-4.0		6.0	8.0	
Isolation (dB)	4.0-12.0	4.0-12.0		25	40		
	4.0-12.0	4.0-12.0			30		
	4.0-12.0	4.0-12.0			25		
Input 1 dB Compression (dBm)	4.0-12.0	4.0-12.0			+2		L (+7 to +10)
					+5		M (+10 to +13)
					+8		N (+13 to +16)
					+11		H (+16 to +19)
					+14		S (+19 to +22)
Input Two-Tone Third Order Intercept Point (dBm)	4.0-12.0	4.0-12.0			+12		L (+7 to +10)
					+15		M (+10 to +13)
					+18		N (+13 to +16)
					+21		H (+16 to +19)
					+24		S (+19 to +22)

Part Number Options

<i>Please specify diode level and package style by adding to model number.</i>	
Package Style(s) ^{1,2}	Example
A, B, C, E, EZ, P	M1-0412 L A

¹Connectorized test fixtures available for most carrier and surface mount packages. Consult factory.

²For non-connectorized packages, specify I-port configuration by adding -1 or -2 suffix to model number. Default is -2 configuration when not specified.

Marki Microwave reserves the right to make changes to the product(s) or information contained herein without notice. Marki Microwave makes no warranty, representation or guarantee regarding the suitability of its products for any particular purpose, nor does Marki Microwave assume any liability whatsoever arising out of the use of or application of any product.

215 Vineyard Court, Morgan Hill, CA 95037 | Ph: 408.778.4200 | Fax 408.778.4300 | info@markimicrowave.com



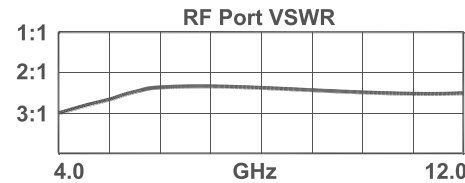
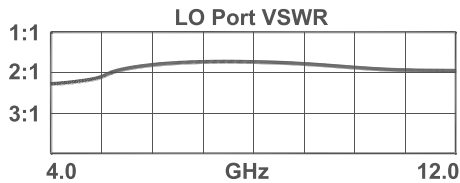
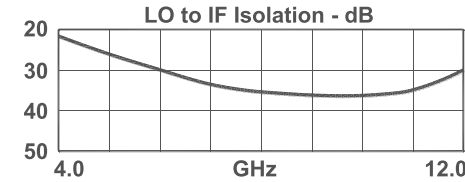
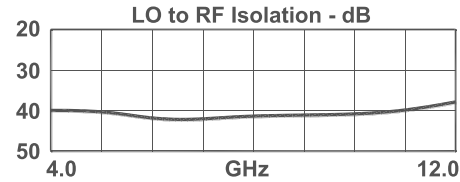
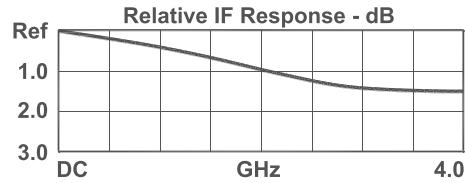
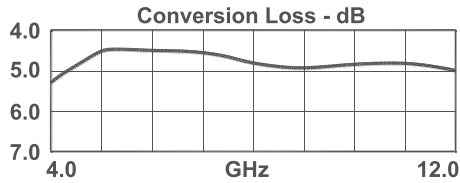
DOUBLE-BALANCED MIXERS

Page 2

M1-0412

**LO/RF 4.0 to 12.0 GHz
IF DC to 4.0 GHz**

Typical Performance



DATA SHEET NOTES:

1. Mixer Conversion Loss Plot IF frequency is 100 MHz.
2. Mixer Noise Figure typically measures within +0.5 dB of conversion loss for IF frequencies greater than 5 MHz.
3. Conversion Loss typically degrades less than 0.5 dB for LO drives 2 dB below the lowest and 3 dB above highest nominal LO drive levels.
4. Conversion Loss typically degrades less than 0.5 dB at +100°C and improves less than 0.5 dB at -55°C.
5. Maximum input power is +23 dBm at +25°C, derated linearly to +20 dBm at +100°C.
6. Specifications are subject to change without notice. Contact Marki Microwave for the most recent specifications and data sheets.
7. Standard configuration for A, B, and C outlines are with connectors and bottom spacer.
8. Catalog mixer circuits are continually improved. Configuration control requires custom mixer model numbers and specifications.

Marki Microwave reserves the right to make changes to the product(s) or information contained herein without notice. Marki Microwave makes no warranty, representation, or guarantee regarding the suitability of its products for any particular purpose, nor does Marki Microwave assume any liability whatsoever arising out of the use or application of any product.

© Marki Microwave, Inc.



215 Vineyard Court, Morgan Hill, CA 95037 | Ph: 408.778.4200 | Fax: 408.778.4300 | info@markimicrowave.com

www.markimicrowave.com

Optical Band Pass Filter



OPTICAL COMMUNICATIONS

Voltage-Controlled Optical Filters VCF Series



Key Features



- 50 and 100 GHz tunable filters for C or L band
- High adjacent and non-adjacent channel rejection
- Good wavelength setting accuracy
- Low insertion loss
- Low chromatic dispersion
- Wide tuning range
- Low tuning voltage
- Pins extruding from side of the package
- Mountable on PCB with small footprint

Applications

- ASE suppression for optical fiber amplifiers (OFAs) and tunable lasers or receivers
- Signal demultiplexers for wavelength division multiplexers (WDMs) or 1xN splitters
- Dynamic wavelength selection associated with WDM systems using optical add/drops and flexible wavelength conversion

The JDSU Agile Optical Components family includes modulators, switches, attenuators and tunable filters. These products provide the basis for spectrally efficient DWDM transmission utilizing dispersion tolerant modulation, channel monitoring, wavelength switching, remote power control and dynamic channel selection. They support a wide range of flexible functionalities at lower operational expenses for the Agile Optical Network. In addition, we have a complete line of tunable lasers assemblies and sub-assemblies in our Agile Transmission Module family.

The JDSU VCF series is a voltage-controlled tunable band pass filters that can be used for amplified spontaneous emission (ASE) suppression of optical signals and for single-channel demultiplexing from a multichannel dense wavelength division multiplexing (DWDM) optical signal stream. The VCF can also be used in flexible and dynamic wavelength optical add/drop applications. The VCF uses hermetic sealing for increased resistance to environmental extremes. The VCF series offers excellent optical performance in either C or L band.

The center wavelength selection is precisely tuned using a stepper motor driven by an external integrated circuit controller. The driver moves the filter up and down in uniform steps in the center wavelength, to provide high resolution. The VCF is compact in size and can easily be mounted on a printed circuit board (PCB).

The transmission spectrum of the VCF is optimized for low insertion loss, high rejection, and low chromatic dispersion.

NORTH AMERICA: 800 498-JDSU (5378)

WORLDWIDE: +800 5378-JDSU

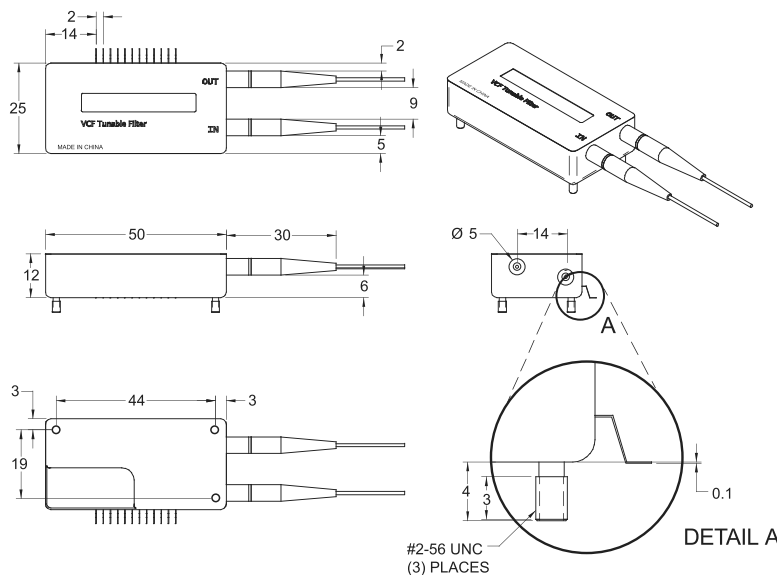
WEBSITE: www.jdsu.com

VCF SERIES

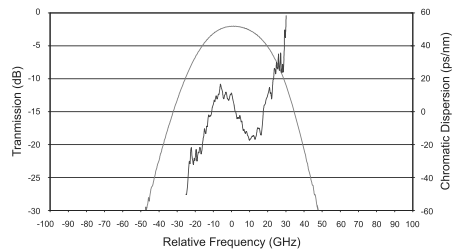
2

Dimensions Diagram

(Specifications in mm unless otherwise noted.)



Filter Performance: VCF050



VCF SERIES

3

Filter Performance: VCF100

Specifications¹

Parameter	VCF050	VCF100
Optimized tuning range	1525 to 1565 nm (C band) or 1565 to 1610 nm (L band)	
Bandwidth (BW at -0.5 dB)	Typical 15 GHz	25 GHz
Bandwidth (BW at -1 dB)	Minimum 18 GHz	30 GHz
Bandwidth (BW at -3 dB)	Typical 35 GHz	70 GHz
Bandwidth (BW at -20 dB)	Maximum 85 GHz	160 GHz
Non-adjacent rejection	Minimum -40 dB	-40 dB
-1 dB bandwidth variation over tuning range	Typical ±5%	±5%
Insertion loss	Maximum 4.5 dB	3.0 dB
Insertion loss variation over tuning range	Typical 1.0 dB	0.5 dB
Frequency setting accuracy ²	Typical ±3 GHz Maximum ±4 GHz	±3 GHz ±5 GHz
Potentiometer frequency backlash	Typical 2 GHz Maximum 8 GHz	2 GHz 8 GHz
Stepper motor frequency backlash	Typical 3 GHz Maximum 9.5 GHz	3 GHz 9.5 GHz
Stepper motor frequency repeatability (unidirectional)	Typical ±0.5 GHz	±0.5 GHz
Polarization dependent loss ³	Maximum 0.50 dB	0.20 dB
Polarization mode dispersion ⁴	0.2 ps	0.2 ps
Group delay dispersion ¹	±50 ps/nm	±20 ps/nm
Return loss	Minimum 35 dB	30 dB
Settling time	Maximum 30 ms	5000 ms
Tuning speed	Maximum 5000 ms	1.2 x 10 ⁶ nm
Wear	Maximum 1.2 x 10 ⁶ nm	SMF-28 with 900 μm buffered jacket
Fiber type	SMF-28 with 900 μm buffered jacket	
Maximum optical power (single-channel)	Maximum 10 dBm	23 dBm
Maximum optical power (all channels)	Maximum 23 dBm	25 x 12 x 50 mm
Dimensions (W x H x D) ⁴ side pinout	25 x 12 x 50 mm	
Operating temperature	-5 to 70°C	
Storage temperature	-40 to 85°C	

1. All specifications are excluding connectors, over operating temperature range -5 to 70°C, wavelength range 1525 to 1565 nm or 1565 to 1610 nm, and all polarization states.
 2. Using insertion loss feedback.
 3. Within specified bandwidth over ±12 GHz from filter center.
 4. Excluding strain relief and connector pins.

Photoreceiver



Discovery Semiconductors, Inc.

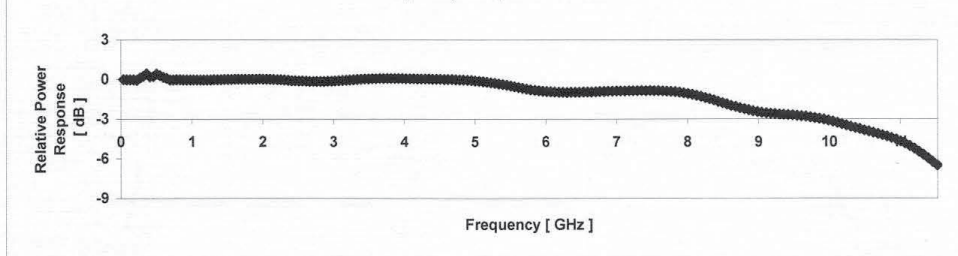
119 SILVIA STREET, EWING, NJ 08628, USA
 PHONE: (609) 434-1311 FAX: (609) 434-1317

Test Data Report

Customer: McGill University	Date: 8/5/2010
Part number: DSC-R402DC-39-FC/APC-K-2	PO : P0271937
Description: InGaAs Optical Receiver	WO : 3899
Tested by: Nilesh Soni	Serial number: 621355
	Witnessed by: <i>[Signature]</i>

Parameter	Specification	Measured Value	Units
-3dB Bandwidth @ Vbd=10V & Vdd=8V	Min: 9.5	9.9	GHz
Coupled DC Responsivity @ 1550 nm	Min: 0.7	0.74	A/W
Coupled conversion gain @ 1550 nm Average optical input -3dBm	Min: 280	343	V/W
Detector dark current @ + 10 V	Max: 100	4	nA
Optical Return Loss @ 1550 nm	Min: 27	50	dB

Frequency Response Curve



Remarks:

- (1) For specifications, please refer to the datasheet for the model of photodiode installed in the Lab Buddy.
- (2) Please clean optical and coaxial connectors before attaching.

➤ALWAYS switch on Lab Buddy first, then apply optical signal.
 ➤ALWAYS remove optical signal first, then switch off the Lab Buddy.

CAUTION:
 When connecting to the RF Output connector, finger tightening is enough for most applications.

Any modifications to this device will void the warranty.

RF Amplifier

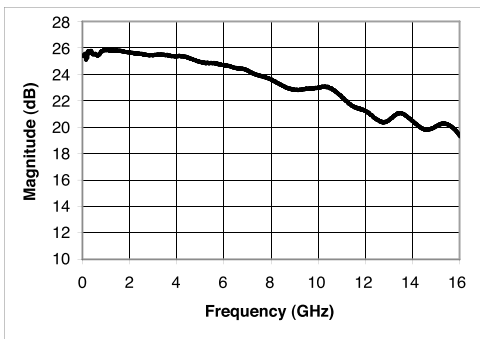


MODEL 5866
10 GHz LINEAR AMPLIFIER
PRODUCT SPECIFICATION

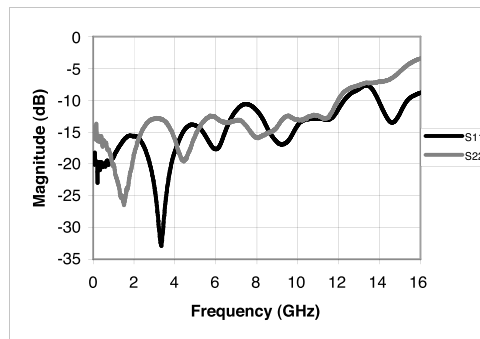
- Linear amplifier with 26 dB gain and 2.5 kHz - 10 GHz bandwidth
- High gain with low power dissipation (1.7 watts at +17 dBm)
- > 4 V p-p linear output
- Temperature compensated design for output stability



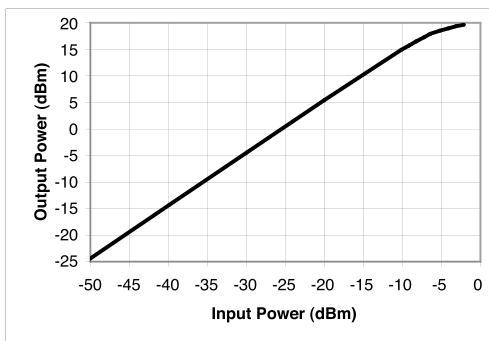
The Picosecond Pulse Labs Model 5866 amplifier has been designed to minimize the variations in gain and phase and to operate at very low frequencies. The 5866 includes internal temperature compensation for excellent output stability over temperature, and exhibits both high output and low power dissipation. It also incorporates internal sequencing circuitry, making it insensitive to power supply application sequence.



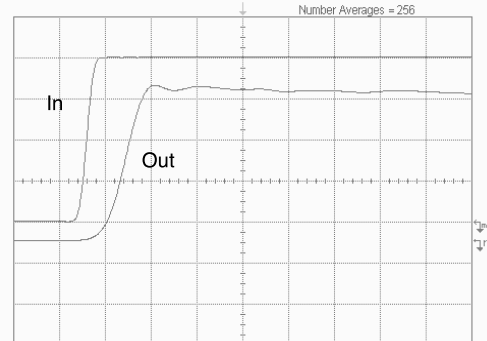
Typical S₂₁
(measured at -22dBm input power)



Typical S₁₁ and S₂₂
(measured at -22dBm input power)



Typical Linearity
(measured with 400 MHz CW)



Typical Response to 15ps Risetime Step
(measured using a PSPL 4022-TDR source and Agilent 40 GHz Oscilloscope)

PICOSECOND PULSE LABS, P.O. BOX 44, BOULDER, CO 80306, USA, TEL: 1.303.443.1249, FAX: 1.303.447.2236
WWW.PICOSECOND.COM



PRODUCT SPECIFICATION MODEL 5866 10 GHz LINEAR AMPLIFIER

5866 Electrical Specifications [2]

PARAMETER	SYMBOL	UNITS	MIN	TYPICAL	MAX	COMMENTS
Polarity						Non-inverting
Upper Frequency 3 dB Point	$f_{3dB,upper}$	GHz	8	10		Relative to gain at 1000 MHz
Lower Frequency 3 dB Point	$f_{3dB,lower}$	kHz		2.5	3	Relative to gain at 1000 MHz
Small Signal Gain	S_{21}	dB	25.0	25.5		Measured at 1000 MHz
Output Power at 1dB Gain Compression	P_{1dB}	dBm		17		Measured at 1000 MHz
Deconvolved Risetime [1]	$t_{r,f}$	ps		35		10% to 90%
Additive Jitter [1] RMS Peak-to-Peak		ps ps _{pp}		0.7 4	1.5 8	
Input / Output Return Loss	S_{11}, S_{22}	dB		12	8	
Noise Figure	NF	dB		5.75	6.5	$f = 1$ GHz

[1] Deconvolution is done by root sum of squares. Input risetime was 15 ps.

[2] Specifications are valid for operation at room temperature.

5866 Operating Specifications

PARAMETER	SYMBOL	UNITS	MIN	TYPICAL	MAX	COMMENTS
Maximum allowed Input		V_{amp}			1.5	Damage threshold for input
DC Supply Current (pos)	$+I_{DC}$	mA			220	Damage threshold
Bias Point Adjust	V_{CP}	V_{DC}	-5		+1	Damage threshold
DC Voltage Supply (pos)	$+V_{DC}$	V_{DC}	8	8	8.25	200 mA typical with $V_{OUT} = 4 V_{p-p}$
DC Voltage Supply (neg)	$-V_{DC}$	V_{DC}	-5.25	-5	-4.75	20 mA typical
Power Dissipation	P_{diss}	W		1.7	2.0	$V_{OUT} = 4 V_{p-p}$
Output Voltage Bias	V_{bias}	V_{DC}	0		16	2.5 k Ω resistor (DC current ≤ 3.5 Ma)
Operating Temperature	T_{CASE}	$^{\circ}C$	-5		75	Case Temperature
Storage Temperature	T_{CASE}	$^{\circ}C$	-40		125	Case Temperature

Static sensitive device, limited 30 day warranty.

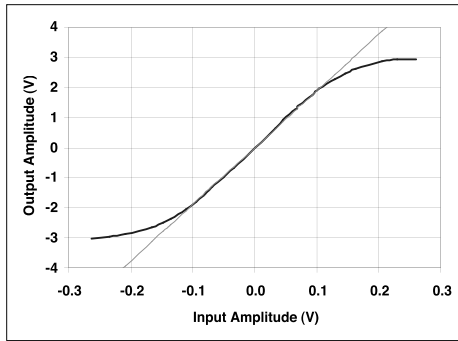
Note: PSPL recommends that the 5866 be driven with a negative polarity signal when the duty cycle is very low. The amplifier may be damaged by excessive heat that is produced with narrow positive pulses. Similarly, signals with a very high duty cycle should be positive. To ensure the amplifier will not be damaged by overheating under such operating conditions, PSPL recommends the positive supply voltage has its current limit set to 220 mA.



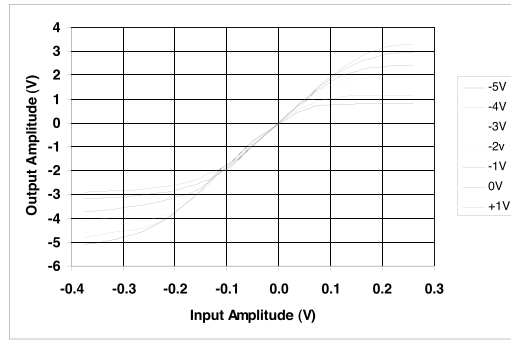
PRODUCT SPECIFICATION MODEL 5866 10 GHZ LINEAR AMPLIFIER

The 5866 is AC-coupled at the input and output. As a result, the average value of the output signal (the DC component) must be at 0 volts. Most data streams are conditioned to have 50% duty cycle when averaged over many microseconds. Those signals make full use of the positive and negative portions of the amplifier's operating range.

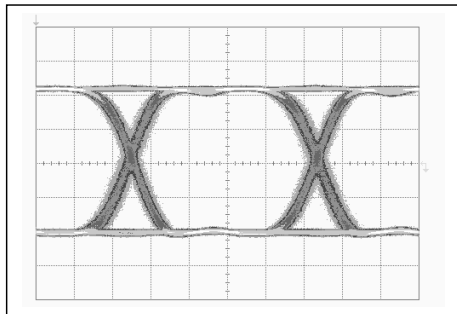
The average amplitude of a low duty cycle signal can be virtually at the baseline. These signals use only one half of the 5866's operating range, and the maximum linear output may be 2 volts peak-peak instead of 4 volts peak-peak. Offsetting V_{cp} will shift the amplifier's operating range so that the amplifier's 4-volt linear range is not centered on 0 V. The following graph shows these shifted operating ranges.



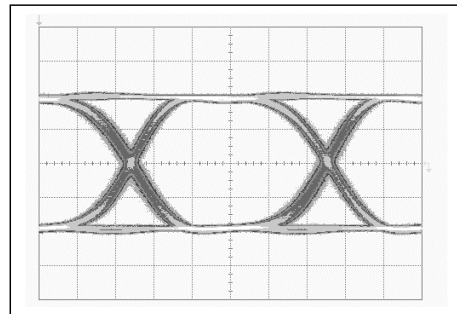
Input vs. Output for Model 5866 using a 3ns Input pulse with pulse repetition frequency of 100kHz and $V_{cp} = 0$ V. The duty cycle is 0.03%. The 5866 remains linear for inputs from <-0.1 V to $>+0.1$ V. The purple line shows 25.5 dB linear gain for comparison.



Input vs. Output as V_{cp} is varied (-5 V $< V_{cp} < +1$ V). For example, when -4 V is applied to V_{cp} , the output voltage range for linear operation will be approximately -4 V to 0 V.



Input Signal from Pattern Generator
10G-b/s, $2^{25}-1$ Pattern, 200mV Amplitude
Amplitude Scale = 50 mV/div, Time Scale = 20 ps/div



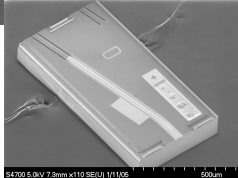
5866 Output Signal is 4 volts
Amplitude Scale = 1 V/div, Time Scale = 20 ps/div

RSOA

PRELIMINARY DATASHEET | SOA-RL-OEC-1550



SOA-RL-OEC-1550 - 1.55µm Reflective Semiconductor Optical Amplifier (SOA)

Features

- 1.55µm operation
- Low polarisation dependent gain (<1.5dB)
- High—small signal gain (>20dB)
- Low front facet reflectivity
- Low ASE ripple (<1.5dB)
- 1.2GHz electrical bandwidth
- InP Buried Heterostructure design
- TEC cooled
- SMA style or 14 pin package available
- Available as packaged or chip-on-carrier
- APC connector provided

Application Examples

- WDM-PON colourless reflective amplifying modulator
- External cavity laser gain block
- ASE Source

Description

The SOA-RL-OEC-1550 is a low polarisation dependent gain device. It has low front facet reflectivity and is ideal as a reflective colourless amplifying modulator in WDM-PON schemes and as a gain block for external cavity lasers. A high polarisation dependent gain device is also available (SOA-R-OEC-1550).

The SOA-RL-OEC-1550 utilises CIPs proprietary InP buried heterostructure design and is available in either a 7-pin butterfly/SMA package with a thermistor, thermo-electric cooler and single mode fibre pigtailed or as a custom chip-on-carrier product. It is generally intended for use with the Angled Polished Connectors (APC) provided. The device is supplied with a 50Ω input impedance to the SMA port and has a direct modulation bandwidth of ~1.2GHz.

Optical and electrical specification All measurements are at chip temperature of 20°C and 1550nm unless stated otherwise.

Item	Test condition	Min.	Typ.	Max.	Unit
Integrated ASE Power	I = 50mA		0.5		mW
Small Signal Gain	I = 50mA		20		dB
Gain Peak Wavelength	I = 50mA	1530		1570	nm
Polarisation Dependent Gain (PDG)	I = 50mA		1.5		dB
Noise Figure (NF)	I = 50mA		7	8.5	dB
ASE Ripple at Peak (R _G)	I = 50mA		0.5	1.5	dB
Saturated Output Power (P _{SAT})	I = 50mA		2		dBm
Electrical Bandwidth (B _w)	I = 80mA P _{IN} = 0dBm		1.2		GHz
Electrical Input impedance			50		Ω

www.ciphotonics.com
.....photonic solutions

CIP Technologies, Adastral Park, Martlesham Heath, Ipswich, IP5 3RE, UK Tel: +44 (0) 1473 663210 info@ciphotonics.com REV: K

PRELIMINARY DATASHEET | SOA-RL-OEC-1550



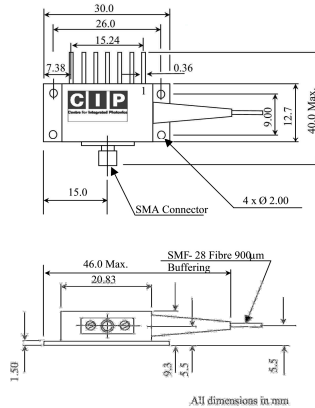
Absolute maximum ratings

Item	Symbol	Rating	Unit
Maximum DC current forward bias	I_{Fmax}	85	mA
Maximum DC voltage forward bias	V_{Fmax}	5.0	V
Maximum DC voltage reverse bias	V_{Rmax}	2.0	V
Maximum optical input power	P_{max}	+13	dBm
RF Voltage (peak to peak)	V_{RF}	4	V
Maximum TEC current	TEC_{IM}	2.0	A
Maximum TEC voltage	TEC_{VM}	3.6	V
Operating temperature	T	15-40	°C
Storage temperature	T_s	10-70	°C
Fibre type	SMF-28 900µm tight buffer, >1m		
Maximum Chip on Carrier Solder Temperature	-	220	°C

Ordering Information— Part Number SOA-RL-OEC-1550

For Custom products please contact CIP Sales on +44 1473 663210 or e-mail sales@ciphotonics.com. For details of your local agent, visit www.ciphotonics.com

Wiring Diagram and Dimensions



Pin Number	Connection
1	Cooler (+)
2	Cooler (-)
3	NC
4	NC
5	Case Ground
6	Thermistor (10kΩ)
7	Thermistor (10kΩ)
SMA	Centre pin +ve (anode) Package case -ve (cathode)



CIP reserves the right to make changes in the design, specifications and other information at any time, and without prior notice. The information contained within the Data Sheet is believed to be accurate. However, no responsibility is assumed for possible inaccuracy or omission. Any information contained herein shall legally bind CIP only if it is specifically incorporated in the terms and conditions of a sales agreement.

Parts of this product are manufactured under one or more of the following patents licensed from British Telecommunications PLC :

European 143000;384764;416879;531377;890129;156566;227783;218344;279680;261943;390614;174729;228435;228435;242084;245085;746887;767923;830721;1181591;93527.3;1183561;170457;225015;247834;292328;320305;537237;624257;647327;94905188.2;691044;77924;782713;822425;822426;813761;97900375.3;97908417.5;97908417.5;865124 US 4826295;5426312;5481397;5202897;6008926;4734387;4728628;4935936;4754459;4964134;5242857;53329542;4736164;4817207;4981814;5015964;844929;5852696;6188511;6625371;6571037;959329/09;4744619;4793690;4879761;4969704;4973122;4995100;5216237;5371820;5656507;6075625;6229945;6097512;5719974;5832011;5917636;5841928;5978400;6104852;6052213;5974073;6178280. Canada 297211;1284683;2182591;2193095;2221693;2372581;2372401;2373546;1255485;1244519;1281802;1296887;1293996;2085596;2117682;2280472;2153798;2155528;2185132;2199513;2367133;2212736;2240519;2248042;1268848;2047196;2065247;2082939;2243279;1236554;1128936;1261483;265604;1295722;1332341;2049356. Japan 2837265;2968335;1000942;2134710;2547001;2935415;2140794;2708165;2984365;2018663;1868104;2670519;2128400;2764141;1957418;2664457;2081567;3117708;3404040;3556665;3346570;95-525482;97-525789;97-534136

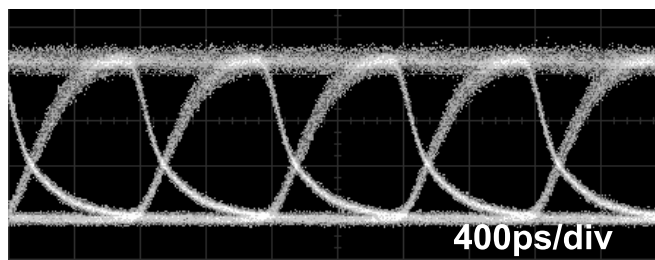
PRELIMINARY DATASHEET | SOA-RL-OEC-1550



Typical switching data for a packaged device

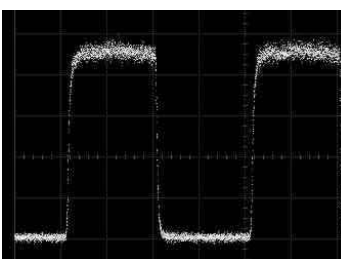
*Eye diagram of RLSOA modulated at 1.25Gb/s (at 20°C).
Pin=-10dBm, bias 80mA, RF=4.4V into 50ohm.*

Extinction ratio =16dB



Electrical switching at 20°C

Pin SOA, dBm	DC bias, mA	Rise Time (10-90%) ps	Fall time (90-10%) ps	XR, dB
-20	50	590	300	23
-20	60	520	370	22
-10	50	490	330	23
-10	60	440	430	19
-10	40	600	300	25
0	50	400	370	23
0	60	460	350	16
0	40	470	290	23



References

- [1] Z. A. El-Sahn, **J. M. Buset**, and D. V. Plant, “Overlapped-subcarrier multiplexing for WDM passive optical networks: Experimental verification and mathematical analysis,” *J. Lightw. Technol.*, vol. 30, no. 5, pp. 754–763, Mar. 2012.
- [2] **J. M. Buset**, Z. A. El-Sahn, and D. V. Plant, “Bandwidth efficient bidirectional 5 Gb/s overlapped-SCM WDM PON with electronic equalization and forward-error correction,” *Opt. Express*, vol. 20, no. 13, pp. 14 428–14 436, Jun. 2012.
- [3] **J. M. Buset**, Z. A. El-Sahn, and D. V. Plant, “Experimental demonstration of a 10 Gb/s subcarrier multiplexed WDM PON,” *IEEE Photon. Technol. Lett.*, vol. 25, no. 15, pp. 1435–1438, Aug. 2013.
- [4] **J. M. Buset**, Z. A. El-Sahn, and D. V. Plant, “Experimental demonstration of a 10 Gb/s RSOA-based 16-QAM subcarrier multiplexed WDM PON,” *Opt. Express*, vol. 22, no. 1, pp. 1–8, Jan. 2014.
- [5] Z. A. El-Sahn, **J. M. Buset**, and D. V. Plant, “Bidirectional WDM PON enabled by reflective ONUs and a novel overlapped-subcarrier multiplexing technique,” in *Proc. Optical Fiber Communication Conference*. Los Angeles, CA, USA: OSA, Mar. 2011, paper OMP7.
- [6] D. V. Plant, Z. A. El-Sahn, **J. M. Buset**, and B. J. Shastri, “Overlapped subcarrier multiplexed WDM PONs enabled by burst-mode receivers,” in *Proc. Access Networks and In-house Communications*. Toronto, Canada: OSA, Jun. 2011, paper ATuA3, note this is an **invited paper**.
- [7] **J. M. Buset**, Z. A. El-Sahn, and D. V. Plant, “Symmetric 2.5 Gb/s RSOA-based WDM-PON with electronic equalization and overlapped-subcarrier multiplexing,” in *Proc. IEEE Photonics Conference*. Arlington, VA, USA: IEEE, Oct. 2011, paper TuE1, pp. 216–217.
- [8] Z. A. El-Sahn, B. J. Shastri, **J. M. Buset**, and D. V. Plant, “A robust overlapped-SCM WDM PON with a standalone burst-mode OLT receiver,” in *Proc. IEEE Photonics Conference*. Arlington, VA, USA: IEEE, Oct. 2011, paper TuE6, pp. 226–227.
- [9] **J. M. Buset**, Z. A. El-Sahn, and D. V. Plant, “Demonstration of a symmetric 10 Gb/s QPSK subcarrier multiplexed WDM PON with IM/DD transceivers and a bandwidth-limited RSOA,” in *Proc. National Fiber Optic Engineers Conference*. Anaheim, CA, USA: IEEE/OSA, Mar. 2013, paper NTh4F.1, note that this work was selected as a semi-finalist for the **Corning Outstanding Student Paper Competition** [international].
- [10] **J. M. Buset**, Z. A. El-Sahn, and D. V. Plant, “Experimental demonstration of a 10 Gb/s 16-QAM SCM WDM PON with bandwidth-limited RSOA and IM/DD transceivers,” in *Proc. European Conference on Optical Communication*. London, UK: IET, Sep. 2013, paper Tu.3.F.5.
- [11] “Cisco Visual Networking Index: Forecast and methodology, 2012–2017,” Cisco Inc., Tech. Rep., May 2013.

- [12] “The zettabyte era—trends and analysis,” Cisco Inc., Whitepaper, May 2013.
- [13] G. Kramer, M. De Andrade, R. Roy, and P. Chowdhury, “Evolution of optical access networks: Architectures and capacity upgrades,” *Proc. IEEE*, vol. 100, no. 5, pp. 1188–1196, May 2012.
- [14] A. Gerber and R. Doverspike, “Traffic types and growth in backbone networks,” in *Proc. Optical Fiber Communication Conference*. Los Angeles, CA, USA: OSA, Mar. 2011, paper OTuR1.
- [15] C. F. Lam, Ed., *Passive Optical Networks: Principles and Practice*, 1st ed. Elsevier/Academic Press, Oct. 2007.
- [16] L. D. Lamb, “The business case for PON,” in *Proc. National Fiber Optic Engineers Conference*. Los Angeles, CA, USA: OSA, Mar. 2011, paper NWD1.
- [17] D. Piehler, “Next-generation components for optical access networks,” in *Proc. Optical Fiber Communication Conference*. Los Angeles, CA, USA: OSA, Mar. 2011, paper OThK5.
- [18] K. Grobe, M. Roppelt, A. Autenrieth, J.-P. Elbers, and M. Eiselt, “Cost and energy consumption analysis of advanced WDM-PONs,” *IEEE Commun. Mag.*, vol. 49, no. 2, pp. S25–S32, Feb. 2011.
- [19] S. Hanatani, “Overview of global FTTH market and state-of-the-art technologies,” in *Proc. OptoElectronics and Communications Conference*. Kyoto, Japan: IEEE, Jun. 2013, paper WP4-1.
- [20] Fiber To The Home Council Americas, “Known North American gigabit FTTH providers,” Jun. 2013. [Online]. Available: <http://www.ftthcouncil.org/d/do/1110>
- [21] R. Heron, “Next generation optical access networks,” in *Proc. Access Networks and In-house Communications*. Toronto, Canada: OSA, Jun. 2011, paper AMA2.
- [22] G. P. Agrawal, *Lightwave Technology: Telecommunication Systems*. John Wiley & Sons, Inc., 2005.
- [23] “G.984.3: Gigabit-capable passive optical networks (G-PON): Transmission convergence layer specification,” ITU-T, Recommendation, Mar. 2008.
- [24] “G.984.1: Gigabit-capable passive optical networks (G-PON): General characteristics,” ITU-T, Recommendation, Mar. 2008.
- [25] K. Tanaka, A. Agata, and Y. Horiuchi, “IEEE 802.3av 10G-EPON standardization and its research and development status,” *J. Lightw. Technol.*, vol. 28, no. 4, pp. 651–661, Feb. 2010.
- [26] “G.987.2: 10-Gigabit-capable passive optical networks (XG-PON): Physical media dependent (PMD) layer specification,” ITU-T, Recommendation, Oct. 2010.
- [27] D. Breuer, C. Lange, E. Weis, M. Eiselt, M. Roppelt, K. Grobe, J.-P. Elbers, S. Dahlfors, F. Cavaliere, and D. Hood, “Requirements and solutions for next-generation access,” in *Proc. ITG Symposium on Photonic Networks*. Leipzig, Germany: IEEE, May 2011, paper 12.
- [28] Y. Luo, X. Zhou, F. Effenberger, X. Yan, G. Peng, Y. Qian, and Y. Ma, “Time- and wavelength-division multiplexed passive optical network (TWDM-PON) for next-generation PON stage 2 (NG-PON2),” *J. Lightw. Technol.*, vol. 31, no. 4, pp. 587–593, Feb. 2013.

- [29] K. Grobe, "Access networks based on tunable transmitters," in *Proc. European Conference on Optical Communication*. London, UK: IET, Sep. 2013, paper We.1.F.1.
- [30] N. Cheng, J. Gao, C. Xu, B. Gao, X. Wu, D. Liu, L. Wang, X. Zhou, H. Lin, and F. Effenberger, "World's first demonstration of pluggable optical transceiver modules for flexible TWDM PONs," in *Proc. European Conference on Optical Communication*. London, UK: IET, Sep. 2013, paper PD4.F.4.
- [31] R. Murano, "Optical component technology options for NGPON2 systems," in *Proc. Optical Fiber Communication Conference*. San Francisco, CA, USA: OSA, Mar. 2014, paper M3I.1.
- [32] C.-H. Lee, W. V. Sorin, and B. Y. Kim, "Fiber to the home using a PON infrastructure," *J. Lightw. Technol.*, vol. 24, no. 12, pp. 4568–4583, Dec. 2006.
- [33] J.-i. Kani, "Enabling technologies for future scalable and flexible WDM-PON and WDM/TDM-PON systems," *IEEE J. Sel. Topics Quantum Electron.*, vol. 16, no. 5, pp. 1290–1297, Sep. 2010.
- [34] R. Urata, C. Lam, H. Liu, and C. Johnson, "High performance, low cost, colorless ONU for WDM-PON," in *Proc. National Fiber Optic Engineers Conference*. Los Angeles, CA, USA: OSA, Mar. 2012, paper NTh3E.4.
- [35] R. Huelsermann, K. Grobe, and D. Breuer, "Cost and performance evaluation of WDM-based access networks," in *Proc. National Fiber Optic Engineers Conference*. Anaheim, CA, USA: IEEE/OSA, Mar. 2013, paper NTh3F.4.
- [36] Y. C. Chung, "Recent advancement in WDM PON technology," in *Proc. European Conference on Optical Communication*. Geneva, Switzerland: IEEE, Sep. 2011, paper Th.11.C.4.
- [37] S. Kamei, "Recent progress on athermal AWG wavelength multiplexer," in *Proc. Optical Fiber Communication Conference*. San Diego, CA, USA: IEEE/OSA, Mar. 2009, paper OW01.
- [38] I. P. Kaminow, T. Li, and A. E. Willner, Eds., *Optical Fiber Telecommunications VI*, 6th ed. Academic Press, May 2013, vol. B.
- [39] S. Pachnicke, J. Zhu, M. Lawin, A. Wonfor, M. H. Eiselt, R. V. Penty, R. Cush, R. Turner, P. Firth, M. Wale, I. White, and J.-P. Elbers, "First demonstration of a full C-band tunable WDM-PON system with novel high-temperature DS-DBR lasers," in *Proc. Optical Fiber Communication Conference*. San Francisco, CA, USA: OSA, Mar. 2014, paper W3G.2.
- [40] J.-M. Kang and S.-K. Han, "A novel hybrid WDM/SCM-PON sharing wavelength for up- and down-link using reflective semiconductor optical amplifier," *IEEE Photon. Technol. Lett.*, vol. 18, no. 3, pp. 502–504, Feb. 2006.
- [41] K. Grobe and J.-P. Elbers, "PON in adolescence: from TDMA to WDM-PON," *IEEE Commun. Mag.*, vol. 46, no. 1, pp. 26–34, 2008.
- [42] K. Sato and H. Toba, "Reduction of mode partition noise by using semiconductor optical amplifiers," *IEEE J. Sel. Topics Quantum Electron.*, vol. 7, no. 2, pp. 328–333, Mar./Apr. 2001.
- [43] W. Lee, M. Y. Park, S. H. Cho, J. Lee, C. Kim, G. Jeong, and B. W. Kim, "Bidirectional WDM-PON based on gain-saturated reflective semiconductor optical amplifiers," *J. Lightw. Technol.*, vol. 17, no. 11, pp. 2460–2462, Nov. 2005.
- [44] J. Prat, C. Arellano, V. Polo, and C. Bock, "Optical network unit based on a bidirectional reflective semiconductor optical amplifier for fiber-to-the-home networks," *IEEE Photon. Technol. Lett.*, vol. 17, no. 1, pp. 250–252, Jan. 2005.

- [45] K. Y. Cho, Y. J. Lee, H. Choi, A. Murakami, A. Agata, Y. Takushima, and Y. Chung, "Effects of reflection in RSOA-based WDM PON utilizing remodulation technique," *J. Lightw. Technol.*, vol. 27, no. 10, pp. 1286–1295, May 2009.
- [46] C. Arellano, K. Langer, and J. Prat, "Reflections and multiple Rayleigh backscattering in WDM single-fiber loopback access networks," *J. Lightw. Technol.*, vol. 27, no. 1, pp. 12–18, Jan. 2009.
- [47] G. Talli, D. Cotter, and P. D. Townsend, "Rayleigh backscattering impairments in access networks with centralised light source," *Electron. Lett.*, vol. 42, no. 15, pp. 877–878, Jul. 2006.
- [48] R. K. Staubli and P. Gysel, "Crosstalk penalties due to coherent Rayleigh noise in bidirectional optical communication systems," *J. Lightw. Technol.*, vol. 9, no. 3, pp. 375–380, Mar. 1991.
- [49] K. Y. Cho, Y. Takushima, and Y. C. Chung, "10-Gb/s operation of RSOA for WDM PON," *IEEE Photon. Technol. Lett.*, vol. 20, no. 18, pp. 1533–1535, Sep. 2008.
- [50] J. G. Proakis and M. Salehi, *Digital Communications*, 5th ed. New York: McGraw-Hill, 2008.
- [51] K. Y. Cho, B. S. Choi, Y. Takushima, and Y. C. Chung, "25.78-Gb/s operation of RSOA for next-generation optical access networks," *IEEE Photon. Technol. Lett.*, vol. 23, no. 8, pp. 495–497, Apr. 2011.
- [52] K. Y. Cho, U. H. Hong, Y. Takushima, A. Agata, T. Sano, M. Suzuki, and Y. C. Chung, "103-Gb/s long-reach WDM PON implemented by using directly modulated RSOAs," *IEEE Photon. Technol. Lett.*, vol. 24, no. 3, pp. 209–211, Feb. 2012.
- [53] A. Agata, K. Y. Cho, Y. Takushima, Y. C. Chung, and Y. Horiuchi, "Study on ISI mitigation capability of MLSE equalizers in RSOA-based 10 Gbit/s WDM PON," in *Proc. European Conference on Optical Communication*. Vienna, Austria: IEEE, Sep. 2009, paper 9.5.5.
- [54] A. Agata and Y. Horiuchi, "RSOA-based 10G WDM PON using FEC and MLSE equalizers," in *Proc. Optical Fiber Communication Conference*. San Diego, CA, USA: IEEE/OSA, Mar. 2010, paper OWG3.
- [55] D. Fritzsche, L. Schürer, A. Ehrhardt, D. Breuer, H. Oeruen, and C. G. Schäffer, "Field trial investigation of 16-states MLSE equalizer for simultaneous compensation of CD, PMD and SPM," in *Proc. Optical Fiber Communication Conference*. San Diego, CA, USA: IEEE/OSA, Mar. 2009, paper OWE4.
- [56] Q. Guo and A. Tran, "20-Gb/s single-feeder WDM-PON using partial-response maximum likelihood equalizer," *IEEE Photon. Technol. Lett.*, vol. 23, no. 23, pp. 1802–1804, Dec. 2011.
- [57] I. Papagiannakis, M. Omella, D. Klonidis, A. Birbas, J. Kikidis, I. Tomkos, and J. Prat, "Investigation of 10-Gb/s RSOA-based upstream transmission in WDM-PONs utilizing optical filtering and electronic equalization," *IEEE Photon. Technol. Lett.*, vol. 20, no. 24, pp. 2168–2170, Dec. 2008.
- [58] H. Kim, "10-Gb/s operation of RSOA using a delay interferometer," *IEEE Photon. Technol. Lett.*, vol. 22, no. 18, pp. 1379–1381, Sep. 2010.
- [59] M. Omella, I. Papagiannakis, B. Schrenk, D. Klonidis, J. A. Lázaro, A. N. Birbas, J. Kikidis, J. Prat, and I. Tomkos, "10 Gb/s full-duplex bidirectional transmission with RSOA-based ONU using detuned optical filtering and decision feedback equalization," *Opt. Express*, vol. 17, no. 7, pp. 5008–5013, Mar. 2009.

- [60] M. Presi, A. Chiuchiarelli, R. Corsini, P. Choudury, F. Bottoni, L. Giorgi, and E. Ciaramella, "Enhanced 10 Gb/s operations of directly modulated reflective semiconductor optical amplifiers without electronic equalization," *Opt. Express*, vol. 20, no. 26, pp. B507–B512, Dec. 2012.
- [61] G. de Valicourt and R. Brenot, "10 Gbit/s modulation of reflective SOA without any electronic processing," in *Proc. Optical Fiber Communication Conference*. Los Angeles, CA, USA: OSA, Mar. 2011, paper OThT2.
- [62] G. de Valicourt, D. Maké, J. Landreau, M. Lamponi, G. H. Duan, P. Chanclou, and R. Brenot, "New RSOA devices for extended reach and high capacity hybrid TDM/WDM-PON networks," in *Proc. European Conference on Optical Communication*. Vienna, Austria: IEEE, Sep. 2009, paper 9.5.2.
- [63] B. Schrenk, G. de Valicourt, M. Omella, J. A. Lázaro, R. Brenot, and J. Prat, "Direct 10-Gb/s modulation of a single-section RSOA in PONs with high optical budget," *IEEE Photon. Technol. Lett.*, vol. 22, no. 6, pp. 392–394, Mar. 2010.
- [64] D. Smith, I. Lealman, X. Chen, D. Moodie, P. Cannard, J. Dosanjh, L. Rivers, C. Ford, R. Cronin, T. Kerr, L. Johnston, R. Waller, R. Firth, A. Borghesani, R. Wyatt, and A. Poustie, "Colourless 10 Gb/s reflective SOA-EAM with low polarization sensitivity for long-reach DWDM-PON networks," in *Proc. European Conference on Optical Communication*. Vienna, Austria: IEEE, Sep. 2009, paper 8.6.3.
- [65] J.-Y. Kim, S.-H. Yoo, S.-R. Moon, D. C. Kim, and C.-H. Lee, "400 Gb/s (40×10 Gb/s) ASE injection seeded WDM-PON based on SOA-REAM," in *Proc. Optical Fiber Communication Conference*. Anaheim, CA, USA: IEEE/OSA, Mar. 2013, paper OW4D.4.
- [66] G. Talli, A. Naughton, S. Porto, C. Antony, P. Ossieur, and P. D. Townsend, "Advantageous effects of gain saturation in semiconductor optical amplifier-based integrated reflective modulators," *J. Lightw. Technol.*, vol. 32, no. 3, pp. 392–401, Feb. 2014.
- [67] K. Roberts, D. Beckett, D. Boertjes, J. Berthold, and C. Laperle, "100G and beyond with digital coherent signal processing," *IEEE Commun. Mag.*, vol. 48, no. 7, pp. 62–69, Jul. 2010.
- [68] C. Laperle and M. O'Sullivan, "Advances in high-speed DACs, ADCs, and DSP for optical coherent transceivers," *J. Lightw. Technol.*, vol. 32, no. 4, pp. 629–643, Feb. 2014.
- [69] M. Omella, V. Polo, J. A. Lázaro, B. Schrenk, and J. Prat, "10 Gb/s RSOA transmission by direct duobinary modulation," in *Proc. European Conference on Optical Communication*. Brussels, Belgium: IEEE, Sep. 2008, paper Tu.3.E.4.
- [70] K. Y. Cho, Y. Takushima, and Y. C. Chung, "Demonstration of 11-Gb/s, 20-km reach WDM PON using directly-modulated RSOA with 4-ary PAM signal," in *Proc. Optical Fiber Communication Conference*. San Diego, CA, USA: IEEE/OSA, Mar. 2010, paper OWG1.
- [71] K. Y. Cho, U. H. Hong, S. P. Jung, Y. Takushima, A. Agata, T. Sano, Y. Horiuchi, M. Suzuki, and Y. C. Chung, "Long-reach 10-Gb/s RSOA-based WDM PON employing QPSK signal and coherent receiver," *Opt. Express*, vol. 20, no. 14, pp. 15 353–15 358, Jul 2012.
- [72] T. Duong, N. Genay, P. Chanclou, B. Charbonnier, A. Pizzinat, and R. Brenot, "Experimental demonstration of 10 Gbit/s upstream transmission by remote modulation of 1 GHz RSOA using adaptively modulated optical OFDM for WDM-PON single fiber architecture," in *Proc. European Conference on Optical Communication*. Brussels, Belgium: IEEE, Sep. 2008, paper Th.3.F.1.

- [73] N. Cvijetic, "OFDM for next-generation optical access networks," *J. Lightw. Technol.*, vol. 30, no. 4, pp. 384–398, Feb. 2012.
- [74] M.-K. Hong, N. C. Tran, Y. Shi, J. M. Joo, E. Tangdiongga, S. K. Han, and A. M. J. Koonen, "10-Gb/s transmission over 20-km single fiber link using 1-GHz RSOA by discrete multitone with multiple access," *Opt. Express*, vol. 19, no. 26, pp. B486–B495, Nov. 2011.
- [75] J. Zhang, J. Yu, F. Li, N. Chi, Z. Dong, and X. Li, "11 × 5 × 9.3 Gb/s WDM-CAP-PON based on optical single-side band multi-level multi-band carrier-less amplitude and phase modulation with direct detection," *Opt. Express*, vol. 21, no. 16, pp. 18 842–18 848, Aug. 2013.
- [76] D. Lavery, R. Maher, D. S. Millar, B. C. Thomsen, P. Bayvel, and S. J. Savory, "Digital coherent receivers for long-reach optical access networks," *J. Lightw. Technol.*, vol. 31, no. 4, pp. 609–620, Feb. 2013.
- [77] E. Wong, "Next-generation broadband access networks and technologies," *J. Lightw. Technol.*, vol. 30, no. 4, pp. 597–608, Feb. 2012.
- [78] M. Fujiwara, J.-i. Kani, H. Suzuki, and K. Iwatsuki, "Impact of backreflection on upstream transmission in WDM single-fiber loopback access networks," *J. Lightw. Technol.*, vol. 24, no. 2, pp. 740–746, Feb. 2006.
- [79] J. L. Wei, E. Hugues-Salas, R. P. Giddings, X. Q. Jin, X. Zheng, S. Mansoor, and J. M. Tang, "Wavelength reused bidirectional transmission of adaptively modulated optical OFDM signals in WDM-PONs incorporating SOA and RSOA intensity modulators," *Opt. Express*, vol. 18, no. 10, pp. 9791–9808, May 2010.
- [80] J. Ko, S. Kim, J. Lee, S. Won, Y. S. Kim, and J. Jeong, "Estimation of performance degradation of bidirectional WDM transmission systems due to Rayleigh backscattering and ASE noises using numerical and analytical models," *J. Lightw. Technol.*, vol. 21, no. 4, pp. 938–946, Apr. 2003.
- [81] C. W. Chow, C. H. Yeh, C. H. Wang, C. L. Wu, S. Chi, and C. Lin, "Studies of OFDM signal for broadband optical access networks," *IEEE J. Sel. Areas Commun.*, vol. 28, no. 6, pp. 800–807, Aug. 2010.
- [82] T. H. Wood, R. A. Linke, B. L. Kasper, and E. C. Carr, "Observation of coherent Rayleigh noise in single-source bidirectional optical fiber systems," *J. Lightw. Technol.*, vol. 6, no. 2, pp. 346–352, Feb. 1988.
- [83] P. Gysel and R. K. Staubli, "Statistical properties of Rayleigh backscattering in single-mode fibers," *J. Lightw. Technol.*, vol. 8, no. 4, pp. 561–567, Apr. 1990.
- [84] C. Arellano, C. Bock, J. Prat, and K.-D. Langer, "RSOA-based optical network units for WDM-PON," in *Proc. Optical Fiber Communication Conference*. Anaheim, CA, USA: OSA, Mar. 2006, paper OTuC1.
- [85] R. Hui, B. Zhu, R. Huang, C. T. Allen, K. R. Demarest, and D. Richards, "Subcarrier multiplexing for high-speed optical transmission," *J. Lightw. Technol.*, vol. 20, no. 3, pp. 417–427, Mar. 2002.
- [86] K. Y. Cho, A. Murakami, Y. J. Lee, A. Agata, Y. Takushima, and Y. C. Chung, "Demonstration of RSOA-based WDM PON operating at symmetric rate of 1.25 Gb/s with high reflection tolerance," in *Proc. Optical Fiber Communication Conference*. San Diego, CA, USA: OSA, Feb. 2008, paper OTuH4.

- [87] J. M. Fabrega, E. T. Lopez, J. A. Lázaro, M. Zuhdi, and J. Prat, "Demonstration of a full duplex PON featuring 2.5 Gbps sub carrier multiplexing downstream and 1.25 Gbps upstream with colourless ONU and simple optics," in *Proc. European Conference on Optical Communication*. Brussels, Belgium: IEEE, Sep. 2008, paper We.1.F.6.
- [88] J. M. Fabrega, A. E. Mardini, V. Polo, J. A. Lázaro, E. T. Lopez, R. Soila, and J. Prat, "Deployment analysis of TDM/WDM single fiber PON with colourless ONU operating at 2.5 Gbps subcarrier multiplexed downstream and 1.25 Gbps upstream," in *Proc. National Fiber Optic Engineers Conference*. San Diego, CA, USA: IEEE/OSA, Mar. 2010, paper NWB5.
- [89] H. Kim, "Long-reach WDM-PON using directly modulated RSOAs and subcarrier multiplexing," in *Proc. Optical Fiber Communication Conference*. Los Angeles, CA, USA: OSA, Mar. 2012, paper OW1B.3.
- [90] Z. Al-Qazwini and H. Kim, "10-Gbps single-feeder, full-duplex WDM-PON using directly modulated laser and RSOA," in *Proc. Optical Fiber Communication Conference*. Los Angeles, CA, USA: OSA, Mar. 2012, paper OTh1F.5.
- [91] S. Y. Kim, E. S. Son, S. B. Jun, and Y. C. Chung, "Effects of downstream modulation formats on the performance of bidirectional WDM-PON using RSOA," in *Proc. Optical Fiber Communication Conference*. Anaheim, CA, USA: OSA, Mar. 2007, paper OWD3.
- [92] J. Zhang, X. Yuan, Y. Gu, Y. Huang, M. Zhang, and Y. Zhang, "A novel bidirectional RSOA based WDM-PON with downstream DPSK and upstream re-modulated OOK data," in *Proc. International Conference on Transparent Optical Networks*. Azores: IEEE, Jun. 2009, paper We.P.1.
- [93] S. Y. Kim, S. B. Jun, Y. Takushima, E. S. Son, and Y. C. Chung, "Enhanced performance of RSOA-based WDM PON by using Manchester coding," *J. Opt. Netw.*, vol. 6, no. 6, pp. 624–630, Jun. 2007.
- [94] A. Chiuchiarelli, M. Presi, R. Proietti, G. Contestabile, P. Choudhury, L. Giorgi, and E. Ciarrella, "Enhancing resilience to Rayleigh crosstalk by means of line coding and electrical filtering," *IEEE Photon. Technol. Lett.*, vol. 22, no. 2, pp. 85–87, Jan. 2010.
- [95] Q. Guo and A. V. Tran, "Mitigation of Rayleigh noise and dispersion in REAM-based WDM-PON using spectrum-shaping codes," *Opt. Express*, vol. 20, no. 26, pp. B452–B461, Dec. 2012.
- [96] C. F. Marki, F. A. Marki, and S. C. Esener, "Reduction of interferometric optical crosstalk penalty via DC blocking," *Electron. Lett.*, vol. 43, no. 11, pp. 644–646, May 2007.
- [97] D. R. Jorgesen, C. F. Marki, and S. C. Esener, "Improved high pass filtering for passive optical networks," *IEEE Photon. Technol. Lett.*, vol. 22, no. 15, pp. 1144–1146, Aug. 2010.
- [98] J. Prat, "Rayleigh back-scattering reduction by means of quantized feedback equalization in WDM-PONs," in *Proc. European Conference on Optical Communication*. Torino, Italy: IEEE, Sep. 2010, paper Th.10.B.3.
- [99] Q. Guo and A. V. Tran, "Reduction of backscattering noise in 2.5 and 10 Gbit/s RSOA-based WDM-PON," *Electron. Lett.*, vol. 47, no. 24, pp. 1333–1335, Nov. 2011.
- [100] G. Haßlinger, "Quality-of-service analysis for statistical multiplexing with Gaussian distributed and autoregressive input," *Telecommunication Systems*, vol. 16, no. 3-4, pp. 315–334, 2001.

- [101] G. Haßlinger, “Validation of Gaussian traffic modeling using standard IP measurement,” in *Proc. Conference on Measuring, Modelling and Evaluation of Computer and Communication Systems*. Nürnberg, Germany: VDE, Mar. 2006.
- [102] G. Haßlinger, J. Mende, R. Geib, T. Beckhaus, and F. Hartleb, “Measurement and characteristics of aggregated traffic in broadband access networks,” in *Managing Traffic Performance in Converged Networks*, ser. Lecture Notes in Computer Science, L. Mason, T. Drwiega, and J. Yan, Eds. Springer Berlin / Heidelberg, 2007, vol. 4516, pp. 998–1010.
- [103] F. Hartleb and G. Haßlinger, “Comparison of link dimensioning methods for TCP/IP networks,” in *Proc. Global Telecommunications Conference*, vol. 4. San Antonio, TX, USA: IEEE, Nov. 2001, pp. 2240–2247.
- [104] C. Courcoubetis and R. Weber, *Pricing Communication Networks: Economics, Technology and Modelling*. Chichester, UK: John Wiley & Sons, Ltd., 2003, ch. 4, pp. 83–110.
- [105] A. Adas, “Traffic models in broadband networks,” *IEEE Commun. Mag.*, vol. 35, no. 7, pp. 82–89, Jul. 1997.
- [106] J. Kilpi and I. Norros, “Testing the Gaussian approximation of aggregate traffic,” in *Proc. Internet Measurement Workshop*. Marseille, France: ACM, Nov. 2002, pp. 49–61.
- [107] R. van de Meent, M. Mandjes, and A. Pras, “Gaussian traffic everywhere?” in *Proc. International Conference on Communications*, vol. 2. Istanbul, Turkey: IEEE, Jun. 2006, pp. 573–578.
- [108] H. G. Perros, *Connection-Oriented Networks: SONET/SDH, ATM, MPLS and Optical Networks*. Wiley, 2005, ch. 4, pp. 81–100.
- [109] J. D. H. Alexander, “Clock recovery from random binary signals,” *Electron. Lett.*, vol. 11, no. 22, pp. 541–542, Oct. 1975.
- [110] C. R. Hogge, Jr., “A self correcting clock recovery circuit,” *J. Lightw. Technol.*, vol. 3, no. 6, pp. 1312–1314, Dec. 1985.
- [111] M. Müller, R. Stephens, and R. McHugh, “Total jitter measurement at low probability levels, using optimized BERT scan method,” Agilent Technologies, Tech. Rep., 2005.
- [112] I. Papagiannakis, M. Omella, D. Klonidis, J. A. L. Villa, A. N. Birbas, J. Kikidis, I. Tomkos, and J. Prat, “Design characteristics for a full-duplex IM/IM bidirectional transmission at 10 Gb/s using low bandwidth RSOA,” *J. Lightw. Technol.*, vol. 28, no. 7, pp. 1094–1101, Apr. 2010.
- [113] H. Kim, “Transmission of 10-Gb/s directly modulated RSOA signals in single-fiber loopback WDM PONs,” *IEEE Photon. Technol. Lett.*, vol. 23, no. 14, pp. 965–967, Jul. 2011.
- [114] Y. Wang, E. Serpedin, and P. Ciblat, “An alternative blind feedforward symbol timing estimator using two samples per symbol,” *IEEE Trans. Commun.*, vol. 51, no. 9, pp. 1451–1455, Sep. 2003.
- [115] B. Châtelain and F. Gagnon, “Peak-to-average power ratio and intersymbol interference reduction by Nyquist pulse optimization,” in *Proc. Vehicular Technology Conference*, vol. 2. Los Angeles, CA, USA: IEEE, Sep. 2004, pp. 954–958.

- [116] S. C. Thompson, J. G. Proakis, and J. R. Zeidler, "The effectiveness of signal clipping for PAPR and total degradation reduction in OFDM systems," in *Proc. Global Telecommunications Conference*, vol. 5. St. Louis, MO, USA: IEEE, Dec. 2005, pp. 2807–2811.
- [117] J. Kim and Y. Shin, "An effective clipped companding scheme for PAPR reduction of OFDM signals," in *Proc. IEEE International Conference on Communications*. Beijing, China: IEEE, May 2008, pp. 668–672.
- [118] N. Yoshimoto, J.-i. Kani, S.-Y. Kim, N. Iiyama, and J. Terada, "DSP-based optical access approaches for enhancing NG-PON2 systems," *IEEE Commun. Mag.*, vol. 51, no. 3, pp. 58–64, Mar. 2013.
- [119] M. Abramowitz and I. A. Stegun, Eds., *Handbook of Mathematical Functions with Formulas, Graphs, and Mathematical Tables*, ser. National Bureau of Standards Applied Mathematics Series. Washington, D.C.: U.S. Government Printing Office, 1964, vol. 55.